Experimental study of metastable solid and superfluid helium-4

An Qu

THÈSE DE DOCTORAT
DE L'UNIVERSITÉ PIERRE ET MARIE CURIE

Spécialité : Physique

École doctorale : "Physique en Île-de-France"

réalisée

au Laboratoire Kaslter Brossel

présentée par

An QU

pour obtenir le grade de :

DOCTEUR DE L'UNIVERSITÉ PIERRE ET MARIE CURIE

Sujet de la thèse :

Experimental study of metastable solid and superfluid helium-4

soutenue le 20 janvier 2017

devant le jury composé de :

M^{me}.	Martine BEN AMAR	Examinateur
M.	Frédéric CAUPIN	Rapporteur
M^{me}.	Sylvie COHEN-ADDAD	Examinateur
M.	Philippe JACQUIER	Directeur de thèse
M.	Francisco PERALES	Examinateur
M.	Pierre-Etienne WOLF	Rapporteur

Contents

Acknowledgments

I would like to thank at first my parents for their comprehension and support. I would not have gone so far in my Physics career without them.

I am very grateful to my advisor Philippe Jacquier for sharing his knowledge with me. You are not only a good Physics professor but also an encyclopedia-type friend. I benefit a lot from being your student.

I also thank very much my best college Jules Grucker for the lunch we had everyday in ENS canteen, and thank you for the best white wine *Gewurztraminer*! Jacques Dupont-Roc and Azer Trimeche helped me a lot during my first two years, I appreciate your advices and fruitful discussions. Thanks to Pierre-Jean Nacher and Genevieve Tastevin, you lent me a nice room during the redaction of this thesis. I hope I could share *galette des rois* every year with you.

Of course, my research would not go so well without the help of the electronic service, the mechanic workshop, the cryogenic service and the administrative service. Many thanks to you!

At last, the most special thanks to my dear wife Siyi. Thank you so much for supporting me those years. The lovely home made lunch must be one of my best memories during my PhD career.

Jan 2017, Paris

Introduction

Helium is unique in Nature, being the only element that remains a liquid all the way down in temperature to absolute zero at saturated vapor pressure. In the low temperature regime, both the liquid and solid phases of helium exhibit remarkable properties. Some of them will be detailed in Chap.I.

Our group was initially interested in the metastable solid helium at low temperature, as it is considered as a possible candidate for the new quantum phase "supersolid". In our long term research project, our group has completed the first step: the former Ph.D student F. Souris has successfully brought solid helium to a metastable phase, and has observed an unexpected instability [1, 2]. Since the work of my thesis is a continuation of this experimental study, I began my thesis by determining the exact appearance time of the instability. This part is presented in Chap.III.

Then we were supposed to continue this study by measuring the local sound velocity of the metastable solid using stimulated Brillouin scattering. But due to the limitation of our instruments, I turned to the study of the metastable superfluid helium. In particular, I have studied the cavitation limit of superfluid helium under negative pressure. Because superfluid is a model liquid at low temperature, it is regarded as an ideal object for testing the nucleation theories. Using an interferometric method, we are able to directly measure the cavitation density of metastable superfluid helium, expecting new insights in this topic. To our surprise, we found an inconsistency amongst our result and the others, as it will be discussed in Chap.IV.

Before performing the measurement of the local sound velocity, we could not confirm either results of the cavitation limit of metastable helium. Nevertheless, we found another interesting phenomenon triggered by the cavitation. Every cavitation in metastable helium will end by creating a vapor bubble, and the duration of the bubbles has a dramatic transition as helium passes the $\lambda-$transition between normal and superfluid liquid. In order to understand it, we have studied the dynamics of the bubble and successfully explained most behaviors of bubble. This part will be presented in Chap.V.

Chapter I

Helium at low temperature and its metastable phases

At the beginning of my thesis, a presentation of the helium properties is necessary. For more detail about helium, one may refer to the book of Wilks [3]. It provides a very informative summary of the basic properties of liquid and solid helium. In this chapter, I will first present the properties of solid ^{4}He, as it is related to the previous research of our group. Then I will describe the famous superfluid state of ^{4}He. To have a better understanding of the metastable phases, an introduction of the nucleation theory is presented in the last section.

I.1 Basic properties of solid ^{4}He and supersolid

In this section, I start with a very brief introduction of some of the properties of solid ^{4}He. With regard to solid helium, a recent overview was given by M.H.W. Chan *et al.* [4].

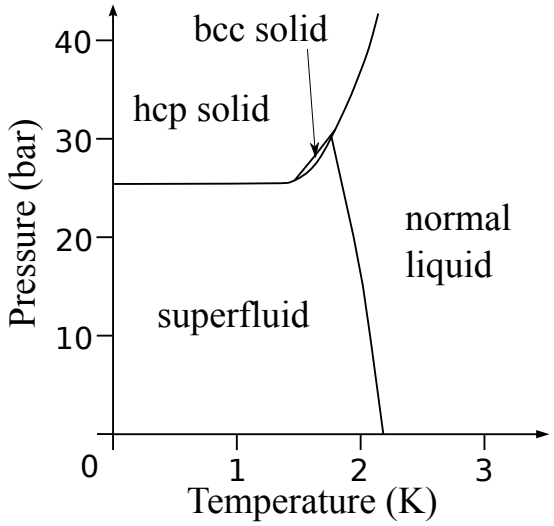

Fig.I.1 – Phase diagram

Helium exist as one of two stable isotopes, ^{3}He and ^{4}He. ^{4}He is the most common isotope on Earth, and it is also our experimental object. The phase diagram for ^{4}He Fig.I.1 shows that there are two primary phases of solid ^{4}He at relatively low pressure: a hcp phase and a narrow region of bcc phase. Under pressure, ^{4}He remains a liquid until a pressure just above 25 bars is applied, and the transition pressure between the solid and superfluid helium barely depends on the temperature below 1.5 K. It is because the zero point motion of helium atoms is large compared to their thermal motion at low temperature. It implies that solid helium has a significant quantum behavior. In solid physics, we can characterize the quantum nature of solid by the de Boer parameter Λ [5].

$$\Lambda = \frac{h}{\sigma\sqrt{m\epsilon}}$$

where h is Planck's constant and m the mass of the molecule. The constants σ and ϵ are obtained by assuming that the force field of most molecules may be represented by a *Lennard-Jones* potential:

$$v(r) = 4\epsilon[(\sigma/r)^{12} - (\sigma/r)^6]$$

This de Boer parameter Λ could be regarded as a measure of the ratio of the de Broglie wavelength to the typical distance between two atoms. If $\Lambda < 0.5$, quantum effects are not very important, most elements are in this regime. On the contrary, helium has the largest de Boer parameter, in the case of solid ^{4}He, $\Lambda = 2.7$. Therefore, helium is the element with the most significant quantum character.

Another unusual behavior of solid helium is that the *Lindemann* criterion of melting does not hold. The criterion states that melting is expected when the

root mean square of atomic vibration amplitude exceeds a threshold value of the order of the interatomic separation. For most solids, this ratio is less than 10%. X-ray diffraction study of the *Debye-Waller* factor of hcp solid ^{4}He shows that this ratio is as large as 26% [6]. This property clearly illustrates that the helium atoms are not well localized.

These remarkable properties of solid helium, as well as its coexistence with a superfluid phase, make it a possible candidate for a new state of matter: a solid with superfluid properties.

I.1.1 Supersolid

In 1969, Andreev and Lifshitz proposed a new quantum phase that combines the solid and the superfluid properties, then Chester developed the same idea independently in the same year [7, 8]. They described the possibility that the solid ^{4}He might contain vacancies as an intrinsic property of the system. As solid helium has a large quantum nature, a vacancy can easily exchange its position with an adjacent helium atom through tunnel effect. If the gain in kinetic energy due to delocalization of the atom is larger than the cost of creating a vacancy, then the total energy of the system will be lowered by the presence of such vacancies. Therefore, the system contains a non-zero density of vacancies, which might be considered as weakly interacting. As the atoms of solid are bosons, the vacancies could form a Bose-Einstein condensate and present a superfluid behavior. This is the so-called *Andreev-Lifshitz-Chester* (ALC) scenario of supersolidity.

I.1.2 Experimental search for supersolidity

Different groups have attempted to detect a supersolid state in helium-4 solid. The early experiments by Andreev, Suzuki and Tsymbalenko measured the motion of objects immersed in the crystal [9, 10, 11]. Other measurements had attempted to detect the supersolid phase through mass flows [12], or with the help of torsional oscillators [13]. A detailed review of these experiments was provided by Meisel *et al.* in 1992 [14]. However, nothing unusual was found at this early stage.

The experiment in 2004 by Kim and Chan showed a rotational anomaly in solid helium, and they interpreted it as the possible appearance of a supersolid state [15, 16]. The measured effect is a decrease in the period of their torsional oscillator containing solid helium at temperature lower than 200 mK. This experiment led to a new surge of searching supersolidity, and the explained that as a sign that a fraction of the solid inside this oscillator had become supersolid and had decoupled from the oscillator. Following this experiment, other properties of the crystal were measured and these results have been summarized by S. Balibar *et al.* in [17]. In order to search for other traces of the supersolid, Day and Beamish showed that a variation in shear modulus exists in solid helium at

a temperature similar to that of the rotational anomaly [18]. They explained it by the dislocations of the crystal and the impurities of ^{3}He. Dislocation lines can be regarded as moving lines. At low temperature the ^{3}He atoms are trapped on these lines with a binding energy of the order of 0.73 K [19] and prevent their displacement, which causes stiffening of the crystal. At higher temperatures, the thermally-activated ^{3}He atoms detach and the shear modulus decreases. The origin of the elastic anomaly is therefore related to the presence of crystalline defects (dislocations) in the crystal. Later, more and more evidence led to the same conclusion [20, 21, 22, 23]. At last, in 2013, in the review paper of Chan *et al.* [4], he mentioned "...the torsional oscillator results reported have been dominated by effects associated with the stiffness of the solid helium."

So far, the experimental results led to a simple conclusion: the ALC supersolid state does not exist in solid helium. A possible reason for this could be that the activation energy of vacancies is too large in solid helium.

I.1.3 Activation energy of vacancies

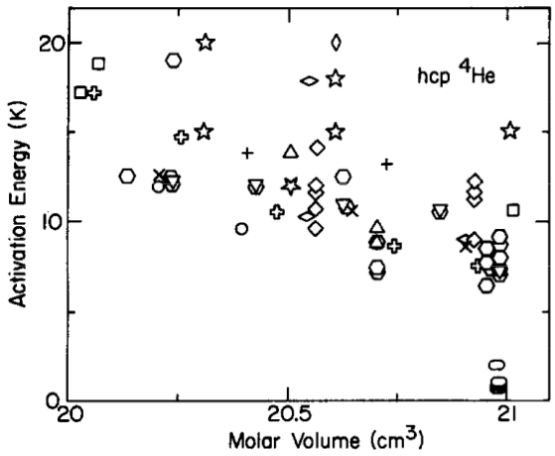

Fig.I.2 – The figure is extracted from [24]. It summarized the existing experimental results for E_v as a function of the molar volume. There is a big difference between different data points, because they crucially depend on the vacancy model used to analyze the measurements.

The ALC scenario is based on the non-zero density of vacancies in the crystal at zero temperature. At finite temperature, the solid always contains a number of thermally activated vacancies. Their density varies with the temperature T as $S(T)\exp(-E_v/k_BT)$, where $S(T)$ is an entropy contribution depending on the vacancy state density, and E_v is the activation energy of one vacancy which directly determines the vacancy density in the crystal [24]. Experimentally, there are two main methods to measure the density of vacancies in crystal. One is to directly measure the mesh parameter by neutron or X-ray diffraction. Another

is to measure the variation of the heat capacity as a function of temperature, which contains the contribution of vacancies. A review of these measures can be found in a review by Simmons [24].

Fig.I.2 is directly extracted from [24], it is a summary of the activation energy of vacancy as a function of the molar volume of solid ^{4}He. The figure clearly shows a decrease in E_v when the molar volume V_m increases. Since the vacancy density exponentially depends on $-E_v$, the maximum density should appear at the largest molar volume. For a stable solid ^{4}He, its melting limit is $V_{mf} = 20.97\text{cm}^3$ (for temperature 1 K), which corresponds to a E_v about 7 K to 15 K. This value is too high at temperature below 1.5 K, and the vacancy density is therefore very small. Thus the stable solid ^{4}He does not seem to fulfill the conditions of the ALC scenario for supersolidity. But if it were possible to increase V_m beyond the melting limit V_{mf} by retaining the solid phase, we might expect to attain the situation where E_v is small enough to allow the ALC scenario. But first it has to be proven that it is possible to have solid ^{4}He at $V_m > V_{mf}$, which is metastable solid ^{4}He.

I.2 Our search for supersolidity

In 2010, our group launched a long term project of searching supersolidity in metastable solid helium. A metastable phase of solid helium is the state where helium remains solid out of its equilibrium conditions. Most metastable solid are realised by superheating, because in classical crystals the pressure barely influences the melting temperature. There are more details in the review of melting and superheating by Mei *et al.* [25]. However, as indicated above, the melting temperature of solid helium is nearly independent of the pressure at temperatures below 1.5 K. Instead of superheating the crystal, we can control the pressure so as to produce a metastable solid helium.

Metastable phase is highly related to the nucleation theory, which will be described briefly in the next section. And metastable phase is very susceptible to perturbation including thermal fluctuation and impurity in the medium. In order to exclude the influence of heterogeneous nucleation/cavitation in helium, we used a hemisphere-like piezoelectric transducer (PZT) to generate and focus an acoustic wave. As shown in Fig.I.3, we prepare solid ^{4}He at a pressure slightly above the melting pressure. The sound waves sent by the internal surface of the piezoelectric transducer (PZT) cause a pressure modulation δP_{surf}. During the sound propagation, the amplitude of the pressure modulation increases. At the acoustic focus, the pressure modulation δP_{focus} may pass transiently into the metastable regime, which is below the melting pressure. Experimentally creating and measuring such a metastable state was the goal of our group's former Ph.D student F. Souris [1]. He succeeded in doing so and developed a "time-resolved quantitative multiphase interferometric method" to reconstruct the variation of

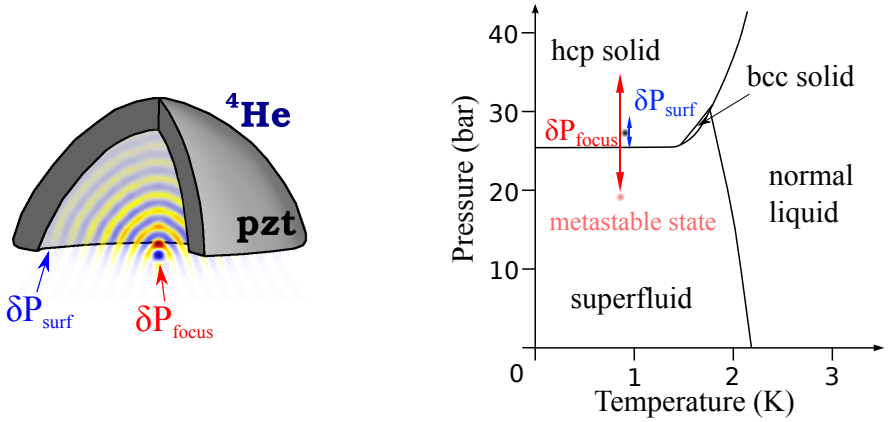

Fig.I.3 – The transducer creates a small variation of pressure on its surface δP_{surf}. As acoustic wave propagates and focuses, δP_{focus} will become much larger. If we start from an initial state near the phase transition line, helium at focus will become metastable. This technique is available for both solid and superfluid helium.

the local density due to the sound waves. This method will be described in detail in Chap.II. As a result, our group has observed and measured that during

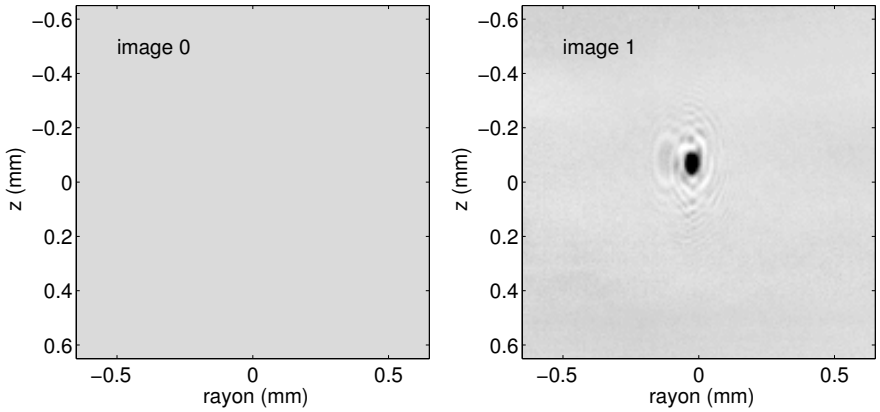

Fig.I.4 – Images of the instability's appearance, extracted from the thesis of F. Souris [2]. Nothing appears in image 0, but in image 1 it shows up. The instability appears in image 1 as an oval defect at the center of the image. The size of this defect is of the order of 0.1 mm.

negative oscillations of the pressure modulation, solid ^{4}He was carried to the molar volume of 21.32 cm^3, which corresponds to a local pressure 4.4 bar below the melting pressure (the absolute local pressure is about 20.9 bar). And we have also observed an unexpected instability of this metastable solid helium. The crystal will break once the local pressure goes below 20.9 bar, and a small region ($\sim$ 0.1 mm) is irreversibly damaged. Whereas H. Maris predicted that perfect helium crystals should remain metastable down to 35 bar below the melting

pressure [26].

Fig.I.4 shows an image of this defect. As concluded by F. Souris: the instability diffuses the incident light rather strongly, which implies that the structure of the defect is quite different from its neighbouring crystal. The defect first appears at a certain PZT tension threshold, and it will expand in the crystal as the sound waves goes on. If the sound is gone, the defect will gradually fade at a speed dependent on the static pressure. It is noteworthy that after a defect has faded and became undetected in the camera, it will appear again for a lower PZT tension. This fact means that the defect is irreversible.

Since the dynamics of this instability is unknown, we may wonder whether it could be related to the supersolid? This interesting instability was the start of my thesis' work.

I.3 Superfluid ^{4}He

Liquid helium has even more remarkable properties compared to its solid phases. For example, because of the relatively high zero point motions, it remains in liquid phase even at extreme low temperature. This makes liquid helium be the purest liquid in the universe, because the only impurity it contains is its isotope. Furthermore, below the temperature T_λ ^{4}He turns to the superfluid phase, which has zero viscosity! So many researchers considered superfluid helium is a model liquid in many domains. In this section, I describe only a few properties of superfluid helium. For a more complete description, one can look at the book written by J. Wilks [3].

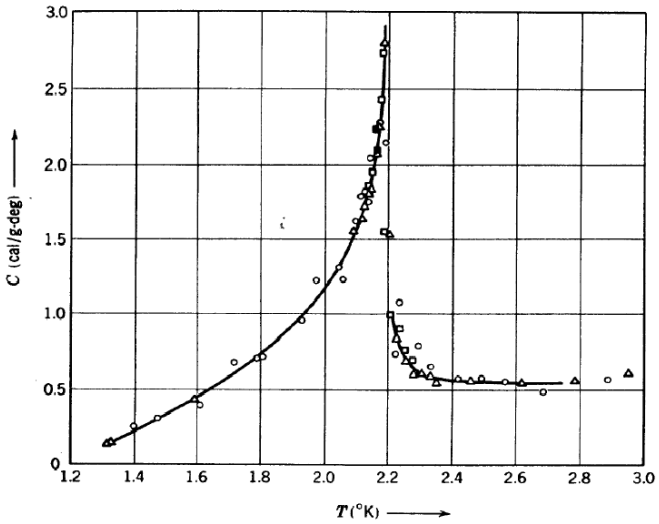

Fig.I.5 – The specific heat of liquid ^{4}He under the saturated vapor pressure [27].

^{4}He becomes the so-called superfluid and displays very remarkable properties below the lambda temperature $T_\lambda = 2.17$ K at saturated vapor pressure. The name of "lambda" comes from a characteristic anomaly of the specific heat. The specific heat of ^{4}He rises to a very high value at T_λ, if we draw it as a function of temperature, we will see a λ-shape as shown in Fig.I.5. For the same reason, the normal liquid/superfluid transition is also called the "lambda transition".

Another anomaly of superfluid helium is the thermal conductivity. If we look at liquid helium in a dewar, while pumping on it so as to cool it below T_λ, the liquid stops boiling when crossing T_λ. This is because the thermal conductivity of liquid helium has suddenly increased so much that the temperature becomes very homogeneous. The walls of the dewar are no longer warmer than the surface of the liquid. They do not provide efficient nucleation sites for bubbles any more. As a result, superfluid helium evaporates from its free surface, instead of showing bubble nucleation on hot defects.

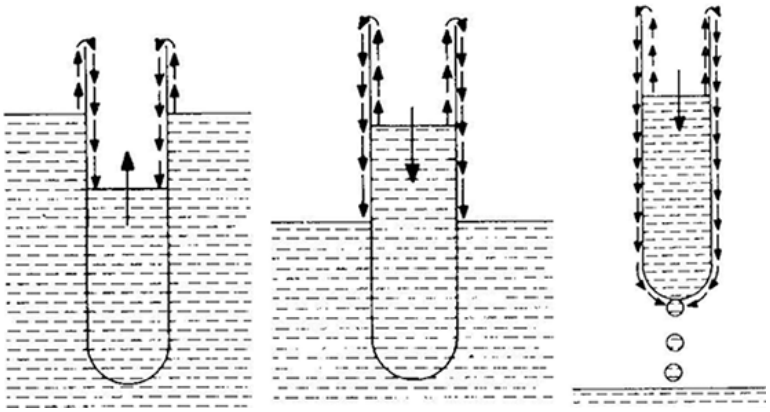

Fig.I.6 – If an empty beaker is lowered into a bath of superfluid helium, the liquid flows over the surface of the beaker until the levels are equalized. If the beaker is then lifted above the bath, the helium flows out over the rim, drops off the bottom of the beaker, and returns to the bath.

The viscosity of superfluid helium, as determined by its rate of flow through narrow slits, is vanishingly small: at least 10^6 times less than the viscosity of normal liquid helium. This is the so-called superfluidity of helium. A striking example is provided by "film flow". Any solid surface in contact with the liquid is covered by a film of liquid, about 30 nm in thickness as a result of van der Waals attraction between the helium atoms and the substrate. This is true in principle for any liquid, but in helium, a flow of the superfluid through the very thin film becomes possible. An illustration of the film flow on beakers is shown in Fig.I.6.

I.3.1 Two fluid model

At first glance these properties present a confusing picture, but many of the unusual properties of the liquid may be correlated with each other and with the thermodynamic functions by a mathematical picture known as the "two fluid model". This model was first proposed by Landau [28], and it serves as a pure phenomenological description. Landau postulated that superfluid liquid helium behaves as if it were a mixture of two fluids freely intermingling with each other without any viscous interaction. These two fluids are the normal fluid and the superfluid, and have densities ρ_n and ρ_s such that:

$$\rho_n + \rho_s = \rho$$

where ρ is the ordinary density of liquid helium. The normal density fraction increases from zero at $T = 0$ to ρ at the lambda point, whereas the superfluid fraction behaves inversely. In addition, the superfluid carries zero entropy and has zero viscosity. Therefore, we can write the equations of motion for the fluid model. And we have the continuity equation for entropy. By using basic continuity equations for both momentum density and entropy density we have:

$$\nabla \cdot \mathbf{j} = -\partial_t \rho$$
$$\nabla \cdot (\rho S\ \mathbf{v}_n) = -\partial_t (\rho S)$$

where $\mathbf{j} = \rho_n \mathbf{v}_n + \rho_s \mathbf{v}_s$ is the total momentum density. The entropy is conserved, because in the approximation of zero viscosity, the motions of the two fluids are reversible.

Then we write the Euler's equation of liquid and ignore the viscosity terms:

$$\partial_t \mathbf{v} + \mathbf{v} \cdot \nabla \mathbf{v} = -\nabla P/\rho$$

The last equation involves the increase of the internal energy:

$$\mathrm{d}U = T\mathrm{d}S - P\mathrm{d}V + G\mathrm{d}M$$

where G is the Gibbs energy density of liquid and $\mathrm{d}M$ is the change in the mass. Since $\mathrm{d}S = 0$, and we let $\mathrm{d}V = 0$, and we have $\mathrm{d}U = G\mathrm{d}M$. The increase of U is due to the change of the superfluid fraction so that:

$$\mathrm{d}\mathbf{v}_s/\mathrm{d}t = -\nabla G = S\nabla T - \nabla P/\rho$$

Landau also proposed to treat these equations in the small velocity approximation by ignoring the quadratic terms in $\mathbf{v}$. And he obtained two equations of wave propagation:

$$\partial_t^2 \rho = (\partial P/\partial \rho)_S \nabla^2 \rho + (\partial P/\partial S)_\rho \nabla^2 S$$
$$\partial_t^2 S = (\rho_s S^2/\rho_n)[(\partial T/\partial \rho)_S \nabla^2 \rho + (\partial T/\partial S)_\rho \nabla^2 S]$$

The solutions of these two equations allows two modes of longitudinal wave propagation. The two fluids can oscillate in phase, giving rise to usual sound, here called "first sound"; or they can oscillate in anti-phase, giving rise to "second sound". First sound is a pressure or density wave, similar to ordinary sound in a fluid. It propagates at a speed of typically 230 m/s. Second sound involves a change in the proportions of the two fluids. It is a temperature wave that obeys the wave equation rather than the diffusion equation. According to the measured properties of helium [29], the speed of second sound around 1 K is about 20 m/s.

The two fluid model is effective to explain the phenomenon that involves heat transport, even it can be applied in superconductors. But this model fails when the flow velocities exceed certain critical values.

I.4 Metastable phases and nucleation theory

Besides the metastable solid phase, helium exhibits many other metastable phases, such as the over-pressurized superfluid or the superfluid at negative pressure. Meanwhile superfluid helium is a model material at low temperature, its metastable phases have been studied experimentally and theoretically (see the review articles of S.Balibar *et al.* [30, 31]). Since our experimental set-up allows to perform similar measurements in studying the metastable superfluid helium, after measuring the exact appearance time of the instability in metastable solid helium, I turned to study the metastable superfluid helium.

I.4.1 Standard nucleation theory

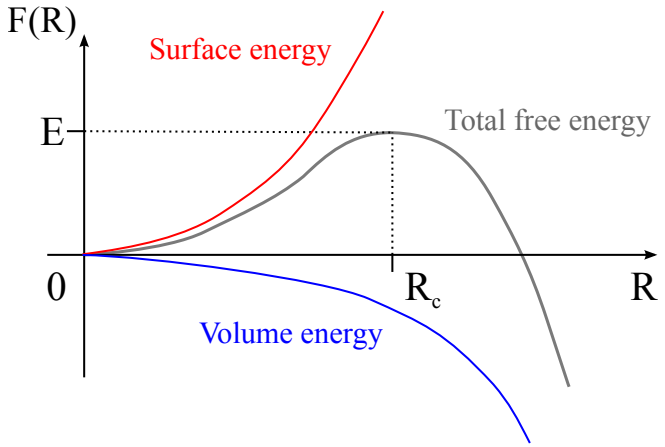

Fig.I.7 – An illustration of the nucleus free energy $F(R)$. The total free energy is the sum of the surface term and the volume term. It reaches the maximum energy barrier at R_c.

The metastable phase, or more precisely, the thermodynamic metastable state is a state outside of the stability region in the phase diagram. An ordinary example is water. Pure water can be supercooled down to −40°C at atmospheric pressure, or be overheated up to 200°C [32]. The metastability is possible because the liquid/solid transition and the liquid/gas transition are discontinuous phase transitions, or the first order transitions.

To understand this phase transition and metastable state, we can consider the simple case of cavitation in a liquid. In the standard nucleation theory, as explained by Landau and Lifshitz [33], we can model cavitation by calculating the free energy of a spherical vapor bubble inside the metastable liquid. This bubble is always considered as a "nucleus". We respectively denote V_v the volume of the bubble and s_v its surface, and it is filled with a gas at a pressure P_v inside a liquid of volume V_l and pressure P_l. Before the nucleus appears, the volume of the metastable phase will be equal to $V_l + V_v$ and its potential $\Omega = -P_l(V_l + V_v)$. After the nucleus has appeared the potential Ω for the whole system becomes $-P_l V_l - P_v V_v + \sigma s_v$ where σ is the surface tension. Then the free energy F of creating a bubble is the difference in the potential Ω:

$$F = \Delta\Omega = -(P_v - P_l)V_v + \sigma s_v$$

The nucleus may be considered to be spherical in isotropic phases, so the free energy can be written as a function of the bubble radius R:

$$F(R) = 4\pi R^2\sigma - \frac{4}{3}\pi R^3(P_v - P_l) \tag{I.1}$$

On the right side of Eq.(I.1), the positive term is the cost in surface free energy, and the second one is a gain in volume energy. Fig.I.7 presents the curve of $F(R)$. We can see that $F(R)$ has a maximum value E for a "critical radius": $R_c = 2\sigma/(P_v - P_l)$. And E equals to

$$E = \frac{16\pi\sigma^3}{3(P_v - P_l)^2}$$

We can consider the following scenario: because of some fluctuations in the liquid, small nuclei will randomly appear and disappear. If the nucleus' radius is smaller than R_c, the local minimum free energy is at $R = 0$, then nucleus will eventually shrink and vanish. On the contrary, if its radius is larger than R_c, the bubble will grow, and the phase transition occurs. So we can regard the maximum value E as the energy barrier for the cavitation.

Using the expression of E, we can write a nucleation rate per unit volume and per unit time as:

$$\Gamma = \Gamma_0 \exp(-E/k_B T)$$

Γ_0 is called the "prefactor". As stated by S. Balibar [30], it is the product of an "attempt frequency" by a "density of independent sites". By integrating this

nucleation rate, we can obtain the probability of the nucleation in a volume V during a time τ:

$$\Sigma = 1 - \exp[-\Gamma_0 V \tau \exp(-E/k_B T)]$$

In most cases, the gas density is negligible, then this probability varies exponentially as a function of $-P_l$. So we can define the nucleation threshold by setting the probability Σ to be one half. This threshold could be a critical pressure P_c such as:

$$P_c = -\left[\frac{16\pi\sigma^3}{3k_B T \ln(\Gamma_0 V \tau)}\right]^{1/2}$$

Estimating Γ_0 is difficult. D. Oxtoby explained in his review that a rigorous calculation only exists in the condensation of a supersaturated gas [34]. Turnbull and Fisher have also given a phenomenological estimation [35].

Although we only modeled the particular case of the cavitation in liquid, the physical scenario is general for all the metastable phases. By substituting the explicit forms of the free energy terms, we could calculate the nucleation rate in other cases.

I.4.2 Nucleation theory in helium

To check the standard theory further, Sinha *et al.* proposed to extend the study inside liquid ^{4}He in the negative pressure [36]. Sinha *et al.* used a bismuth crystal immersed in normal liquid ^{4}He. By sending a pulse through the crystal, they could heat the liquid so as to create bubbles in the bulk of liquid helium. They measured the nucleation rate around 4 K and found a good agreement with the standard nucleation theory.

However, at lower temperature, the nucleation theory fails. We remind the expression of the critical pressure that P_c is proportional to $T^{-0.5}$ and it diverges as T tends to zero. How could a liquid stand an infinite stress? Meanwhile, the critical radius of nucleus $R_c = 2\sigma/|P|$ also tends to zero, and it is not realistic either. The direct modeling of the nucleation threshold in superfluid helium seems difficult. But we can still find a critical pressure. In 1989, H. Maris estimated the spinodal limit of superfluid helium [37, 38]. Here, the "spinodal limit" means once the matter passes this limit, it will be totally unstable and eventually turns to other phases. He considered the graph of the energy $E(V)$ of a system with molar volume V. E diverges to plus infinity as V tends to zero. It has a minimum for a value of V, and tends to zero when V tends to infinity. We can assume E is a continuous function of V, then there must be an inflexion point at a value V_{sp}. The pressure P is the derivative $\mathrm{d}E/\mathrm{d}V$, and it has a minimum value at V_{sp}. The compressibility around V_{sp} should tends to infinity. Since the sound velocity c is , it should vanish near P_{sp}. This is the spinodal pressure. Maris also proposed an equation of state which was corrected by F. Caupin *et al.* for superfluid helium at negative pressure, and found -9.6

bar in ^{4}He. This value could be experimentally checked. Nucleation theories will be further mentioned at the end of Chap.IV.

Chapter II

Experimental devices and preparations

Introduction

Our experimental objects are solid and superfluid helium. These two states of helium have barely the same equilibrium temperature, which is between 0 to 2.2 K. So the experimental conditions of both solid and superfluid helium are very similar. In the first two sections, I will introduce our main experimental

devices which are the optical cryostat and the acoustic transducer. Then I will discuss how we prepare our helium sample in these two different states. At last, I will show the core technique of measuring the local density of metastable helium.

II.1 Optical Cryostat

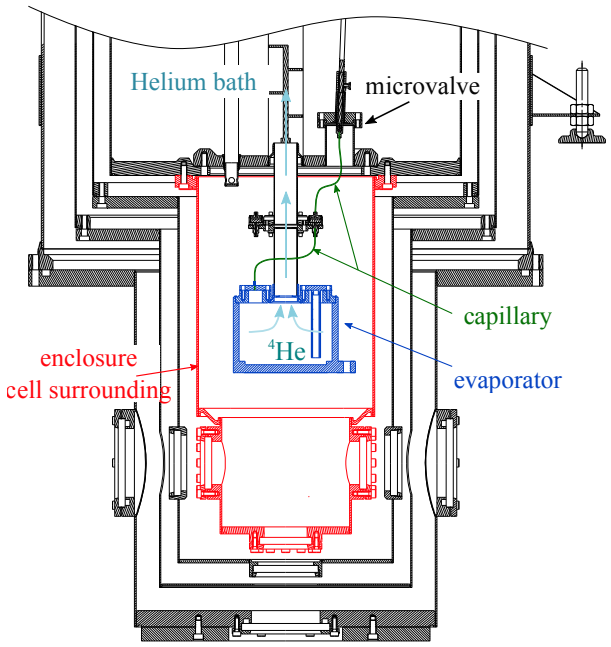

Fig.II.1 – This design plan of the cryostat shows its main parts, such as helium bath, evaporator, optical ports and protection enclosures. The experimental cell (not shown in this figure) will be mounted below the evaporator. The optical port on the bottom was initially planned but is not used in this work.

To avoid the boiling noise and pollution of nitrogen, our group designed and manufactured a nitrogen-free optical cryostat in 2004 [39]. As shown in Fig.II.1, to reduce heat transfer from outside, the cryostat is equipped with four protection layers including two radiation insulation layers and two vacuum enclosures. The inner enclosure, which is called cell surrounding, is filled with a small amount of Neon gas instead of keeping a vacuum inside, so as to significantly increase cooling efficiency at temperatures between 100 K and 25 K. There are four circular optical ports on each layer. Their size and position permit us to observe the experimental cell in two orthogonal directions with a large open angle of 25 degree. A helium bath of 29 liters stands above the cell surrounding. This big bath and good protection layers ensure a long self-sufficient time up to 60 hours. The cooling

system consists of a three-pump system[1] and an evaporator of liquid helium, which is isolated in the center of the cell surrounding. This evaporator is also connected to the helium bath through a capillary with a micro valve, in order to control the liquid flow and keep the evaporator's temperature stable. If regularly maintained, the cryostat can work at a stable temperature from 0.9 K to 5 K for long time.

II.1.1 Experimental Cell

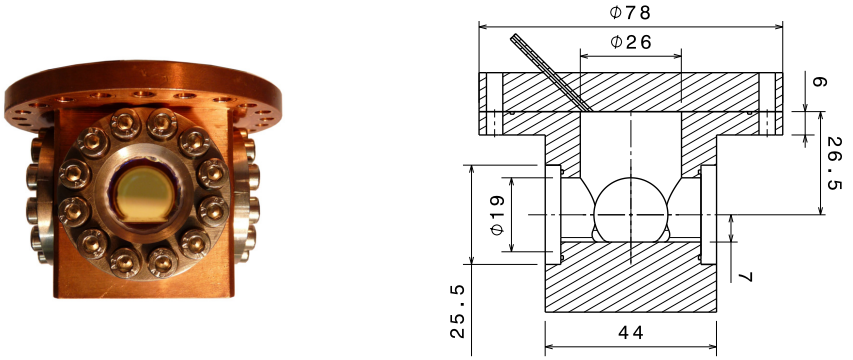

Fig.II.2 – Photo and blueprint of experimental cell. Its inner cavity is like a hollow cylinder with four circular ports. The floor of the cavity is flat and polished to allow free growth of helium crystals. There is a copper cover on top of the cell. The total inner volume is 30 cm^3.

The experimental cell is a small cubic copper chamber suspended below the evaporator. In Fig.II.2, we can see an optical window on each side, which provides a good view of the cell. Those small windows have a diameter of 25.4 mm with a thickness of 5 mm, and are anti-reflection coated for 400 $\sim$ 1100 nm wavelength. Each window is fixed on the copper wall by a stainless steel flange, a *Teflon* joint and an indium joint. The cell can sustain a high pressure up to 40 bar.

As shown in Fig.II.3, the upper part of this cell is a thick copper disk with some small tunnels. On one hand, this disk serves as a thermally conductive cover to seal the cell cavity. On the other hand, the tunnels on the disk allow the passage of wires for electronic devices. Of course, to keep the cell well isolated from vacuum, we are obliged to put wires in a *Teflon*[2] tube which is fixed in the tunnel, and then seal the tunnels by vacuum adhesive *Stycast*.

There is an injection capillary of helium welded on the cell cover. It links directly the cell to the helium reservoir outside of the cryostat through a long tube at room temperature. This reservoir consists of five main parts, they are respectively a high pressure helium bottle, a pressure regulator, a micro flow controller, a Keller X35 pressure transmitter. In order to condense other impurities,

[1] The three-pump system consists of two parallel primary pumps and one root pump.
[2] *Teflon* and *Stycast* are the names of commercial products

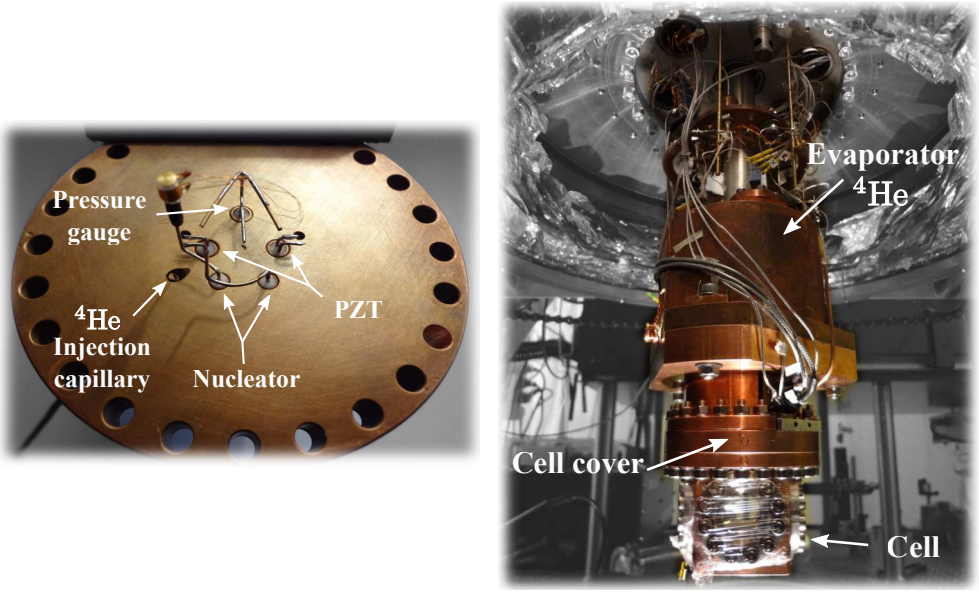

Fig.II.3 – Left: Photo of the cell cover, there are six tunnels on this cover. The one on the left is an injection capillary for helium. The other five are tunnels for wires. This cover is used in solid helium experiments, so we have three additional tunnels for nucleator (see Sect.II.3.2) and pressure gauge (see Sect.II.1.2); Right: Photo of the entire experimental cell part. On the top are the evaporator and wires. Cell cover serves as an important junction between them and the cell. On the photo, the cell (at bottom) is temporarily wrapped with cling film for protection purpose.

before helium gas goes into the experimental cell, the gas will pass through an active carbon trap which is cooled by liquid nitrogen.

II.1.2 Temperature and pressure sensors

The electronic devices related to experimental cell are mainly pressure and temperature gauges, heating resistors, electronic nucleator, and piezoelectric transducers. Most of them are well described in the thesis of Mathieu Mélich [39]. The piezoelectric transducer is a core part of our actual experiments, I will describe it in Sect.II.2.

Depending on the intended temperature range, we have three different types of thermometers. At the higher temperature interval 300 K to 20 K, we use platinum resistors[3] to monitor the cooling process of the cryostat. At lower temperature interval 20 K to 1 K, platinum resistor becomes less sensitive, so some carbon resistors[4] are placed near the evaporator. The third type of thermome-

[3] Correge PT-1000 PTFD102B Sensor Type
[4] *Allan-Bradley* Carbon resistor, 22 and 100 Ω

ters is a germanium resistor[5]. There are two such resistors placed respectively on the bottom of the evaporator and against the cell. A *Lakeshore* Temperature Controller (Model 332) keeps evaporator's temperature steady by a heating resistor with a PID loop feedback. The return value is used as a measure of the cell temperature.

While we do the superfluid experiments, measuring pressure in experimental cell can be done with a pressure gauge at room temperature. As the cell is in a stable state, the whole system is always in hydrostatic equilibrium, the pressure difference between cell and gauge is equivalent to the hydrostatic pressure of several centimeters of vapor helium, which is negligible compared to our experimental pressure. This pressure gauge, as a part of the helium reservoir, is a commercial Keller Series 35X pressure transmitter. It measures pressure in the range from 0 to 30 bar with an accuracy of 15 mbar (given by the manufacturer).

In solid helium experiments, the cell is filled with crystal that is away from the liquid/solid coexistence condition. The injection capillary would probably be blocked by crystal. Consequently, the cell pressure may be different from that measured by the pressure gauge at room temperature. Therefore we decided to put a capacitive pressure gauge of Straty Adams type [40]. This gauge has two bronze electrodes sandwiching a thin insulated void (Mylar paper thickness 25 μm). Its capacity is sensitive to external pressure, and this relation has been measured by the former PhD student F. Souris [2].

II.2 Acoustic Transducer

The principle of creating metastable helium has been discussed in the last chapter (see Sect.I.2). In this section, I will discuss how to manufacture and process a good transducer in superfluid and solid helium.

II.2.1 Hemispherical PZT for superfluid helium

For the purpose of maximizing focalization effect, an ideal PZT should be able to make the wave front arrive at focus synchronously. Since superfluid helium is an isotropic medium, a spherically symmetric acoustic wave front will not be deformed during its propagation. So a hemispherical PZT meets our requirement. Fortunately, poled ceramic PZT is a common device, there are many available commercial suppliers. We thus bought some 401-type PZT from *Morgan Technical Ceramics*. Their inner diameter is $d_{inner} = 12$ mm, and thickness is 2 mm (that gives $d_{outer} = 16$ mm) . The resonant frequency of the first thickness vibration mode is about 1.15 MHz. They are also poled and silver-coated on inner and outer surfaces.

[5] *Lakeshore* GR-200A-250-0.5D

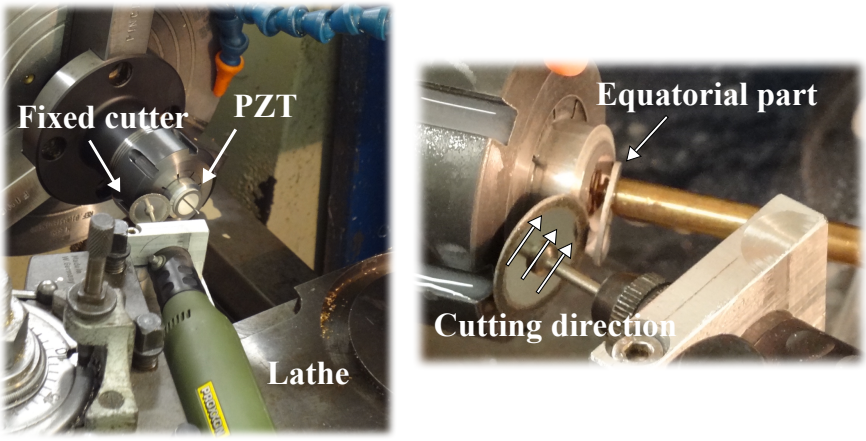

Fig.II.4 – Our first attempt of manufacturing PZT. Left: PZT is fixed on faceplate of lathe, and cutter is placed on carriage. We cut PZT with an attacking angle of 10 degree; Right: A small equatorial part of height 1.4 mm is removed from PZT.

Although this transducer is well made, there are still two steps before applying the PZT in our experiments. Our local density measurement (see Sect.II.4) uses a parallel laser beam to illuminate the acoustic focus zone, and this focus zone should always remain unobstructed. Accordingly, a circular part along the equator of the transducer was removed. Considering our cryostat has a maximum open angle of 25°, we decided to manufacture a transducer of $\theta = 10°$ half observation angle. It gives the thickness to be removed $\delta_{inner} = \sin\theta \cdot d_{inner}/2 = 1.04$ mm and $\delta_{outer} = \sin\theta \cdot d_{outer}/2 = 1.39$ mm. Fig.II.4 shows our first attempt of PZT manufacturing. In order to keep the spherical symmetry of the transducer, the cutting direction is towards the sphere center which is also the acoustic focus. We had successfully manufactured two such transducers, and used them to observe the crystal nucleation in metastable superfluid helium (see Sect.IV.1).

However, during the study, we found that the focalization effect of sound wave was not as good as expected. It is also considered that the ceramic transducer is too fragile to be machined, and the manufacturing precision is not good enough. We decided to make a new transducer and to grind it with sandpaper. Grinding move is very moderate, so this method does not break the transducer, and it also leaves a smooth sectional plane after grinding. Since the grinding direction is not towards the center, a too much grinded transducer would lower the spherical symmetry and probably affect the transducer's thickness vibration. We decided to reduce the observation angle and we only grinded 0.9 mm height of the equatorial part. There is also a hole on the top of PZT to suspend it. This type of transducer was used in the observation of cavitation in superfluid helium (see Sect.IV.2).

The second step is to make a suitable support to fix the transducer in our

experimental cell. Our local density measurement (see Sect.II.4) uses a Jamin interferometer. It sends two parallel laser beams into the cell through the small windows to measure the variation of refractive index. The beam's height determines the position of the acoustic focus, which is about 20 mm below the copper ceiling. It is easy to conclude the requirements for transducer support: first, it should be isolating. Second it should not deform at low temperature. Third, it must be easy to manufacture. Fig.II.5 presents our final plan for transducer support, which is made of PVC. Support is like a hollow cone inside a cylinder. This design eases manufacturing and control of symmetry, and it also provides a solid support to hemispherical transducer. On support's both sides, there are two little insulated holder to keep transducer from dropping or shaking. This PVC support is mounted on two brass sticks which are fixed directly on the copper disk.

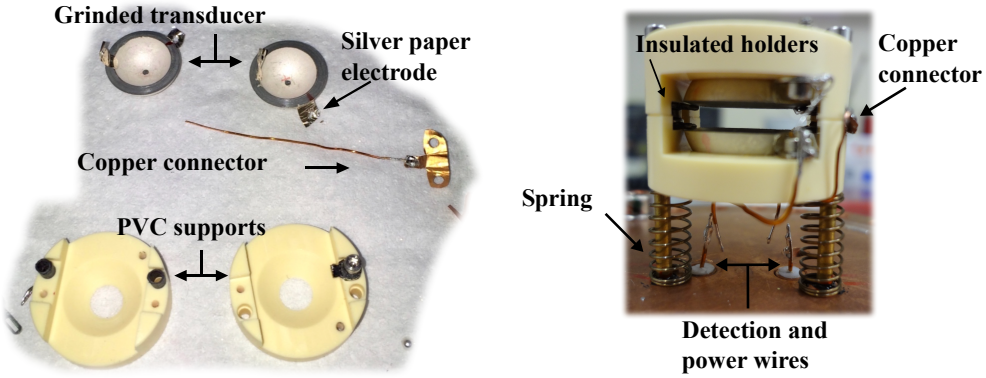

Fig.II.5 – Left: Unmounted PZT and PVC supports. Two silver paper electrodes are already stuck on each transducer. The connector is made of copper paper. All these electric parts have small holes for screws. On PVC support, there are two black plastic tube for insulating bronze sticks. Right: Mounted transducers and support. All connections and fixations are made by springs and screws.

For electrical measurements and power supply of the transducer, we used a 4-wire system with two wires for detection and the other two for power supply. The wires connect directly to measuring devices and signal generators outside the cryostat at room temperature. On the other side, in the cell, they are welded to two electrodes. Those electrodes are made of aluminum paper so that they are small and light enough to keep transducer vibration mode unchanged. To ensure a good contact at low temperature, electrodes are glued on transducer by a conductive low temperature adhesive "Stycast".

Our support is initially designed for two face-to-face PZT so that they could generate a more intense acoustic wave. In this case, two PZT should be mounted in parallel. Then in the consideration of making a removable support system, we made a cooper connector as presented in Fig.II.5. However this connector is

made of copper paper (thickness $\sim$ 80μm), it is too elastic to keep transducer in its position. As a result, we observed two separated focuses in experiments. So later we changed our plan. This support can also be used with a single PZT by simply removing one of them. Actually, at least half the experiments of this thesis were carried with a single PZT.

II.2.2 PZT for solid helium

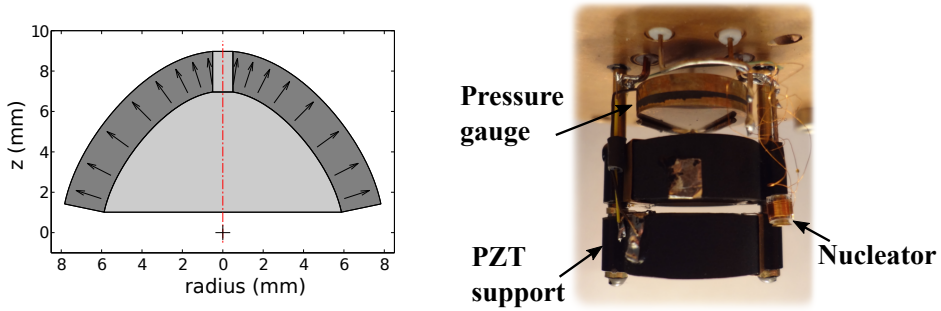

Fig.II.6 – Left: Plan of PZT in solid helium. This sectional profile can compensate the anisotropy of ultrasound velocity. Acoustic focus is marked with black cross. Black arrows represent poling direction. Right: Photo of mounted support and PZT in solid helium. Compared to the one in superfluid, we added a capacitive pressure gauge and a nucleator.

This part of work was mainly done by F. Souris [2]. In solid helium, the case becomes more complex. The hexagonal closest packing solid helium (hcp solid helium) has a uniaxial symmetry. We take this uniaxis parallel to the vertical Oz direction in our coordinate system. Then this uniaxial symmetry has the property that ultrasound velocity is isotropic in the plane (Ox, Oy) and only depends on the angle between the wave vector and the z axis (see Fig.II.6). As a result, a hemispherical transducer does not allow to effectively focus a sound wave in such an anisotropic medium. To compensate the anisotropy of ultrasound velocity, we need a specific PZT of new geometry. This geometry takes the anisotropy of sound speed into account, and it can be obtained by reconstructing the ultrasound wave front inversely from the acoustic focus.

In Fig.II.6, we can clearly see that this geometry of transducer is no longer a hemisphere but similar to a semi-ellipse. No commercial supplier was willing to provide such a transducer, so it was necessary to make one in our laboratory. In 2011, based on raw material PZT 401 of *Morgan Ceramics*, our group had successfully manufactured such a transducer [2]. As for the hemispherical PZT, a small part has been grinded away around the equator. A hole on the top allows for the growth of the crystal inside the transducer. Accordingly, the support is different from the one for superfluid case. It was made by moulding non-

conductive *Stycast* on transducer. Two transducers are also placed face-to-face, and their wire junction is very small, so it has a unique focal centre.

II.2.3 Thermal Dissipation in helium

PZT converts income power into two different energies, one is acoustic energy that propagates in helium, and the other is thermal energy that dissipates in the transducer. This electric-thermal transfer of energy would probably change the temperature of helium medium. We have to estimate this heating effect and its influence to the metastable helium. Our former group member F.Souris already gave an estimation in the case of the solid [2]. His conclusion is that temperature variations at the transducer's surface is on the order of 6.5 mK; for solid helium at 1 mm distance from the surface, thermal dissipation makes temperature raise about 0.4 mK. This heating effect is thus very weak, and negligible. In superfluid case, the fluid has an enormous thermal conductivity, then temperature can be considered identical everywhere in the cell. And the heating effect also gives a negligible change to temperature.

Thus we can safely ignore thermal dissipation in helium introduced by the transducer, and the temperature at focus is always the one measured by the cell thermometer.

II.3 Preparation of experimental helium

Similar to the case of PZT, the preparation of superfluid and solid helium are not exactly the same. For superfluid, there is only one step: filling the cell with liquid helium. If we want to make solid helium, then we need to do another additional step: grow a single-crystal of helium.

II.3.1 Filling the cell with superfluid helium

In order to fill the cell with superfluid helium two ways are possible. One could first lower the temperature to our working temperature, that is 1 K, and then fill the cell with gas that directly condenses to superfluid. Or we can first fill the cell with normal fluid and then cool it to 1 K, ending again with superfluid as described above. The later way is probably less prone to produce vortices. The filling process is performed at constant pressure and temperature.

II.3.2 Creating a single-crystal and making it grow

Compared to the filling process, the growth of a helium single-crystal is not simple. Our objective is to bring superfluid helium to solid phase at a temperature

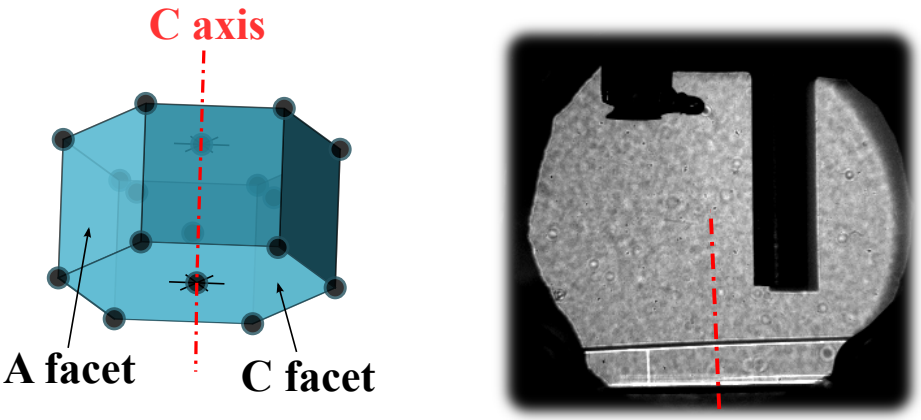

Fig.II.7 – This figure shows hcp solid helium structure. The C-axis in red is perpendicular to C facet, and parallel to A facet. This structure is visible below temperature $T = 1.30$ K. On the right side is a photo of crystal during its growth at 1 K, the contact line between two A facets is then visible.

1 K and at the pressure $P_{solid} \simeq 25.9$ bar which is 560 mbar higher than the solidification/fusion pressure $P_{s/f} = 25.34$ bar. First, we bring superfluid helium to a pressure slightly below $P_{s/f}$ such as $P_{superfluid} \simeq 25.3$ bar. Then we use a small device called "nucleator" to create a small crystal seed. This technique has been used many times in the work of Mélich and Souris [39, 2]. The mechanism is as follow: because of electrostriction, an electric field will locally cause an increase of pressure. When our "nucleator" is turned on, it will locally apply an electric field, and increase the local pressure by $\delta P \simeq 100$ mbar. The local pressure near the "nucleator" will be $P_{local} = P_{superfluid} + \delta P \simeq 25.4$ bar which is more than the fusion pressure $P_{s/f}$. Once a crystal seed is created near the nucleator, we slightly and slowly increase the pressure in the cell, the seed will grow and eventually fall down like a snow flake. Then we switch off the nucleator. Usually, the crystal orientation will be perturbed during its falling. After each creation of a crystal seed, we measure its orientation in two directions, in order to ensure the C-axis of this hcp-type crystal is parallel to the cell vertical axis. Otherwise, the anisotropic crystal structure would greatly affect the focalization of acoustic wave. If the orientation is not good, we melt the crystal by lowering the pressure and start again the whole process.

Once we, by chance, have got a good crystal seed, we will inject helium slowly into the experimental cell from the reservoir. Since helium is at the solid-fluid coexistence, the pressure will remain constant at $P_{s/f}$. However, a direct isothermal process from initial state ($T_i = 1.0$ K, $P_i = 25.34$ bar) to final state ($T_f = 1.0$ K, $P_f \simeq 26$ bar) needs to push solid into the hollow of the PZT and this breaks the

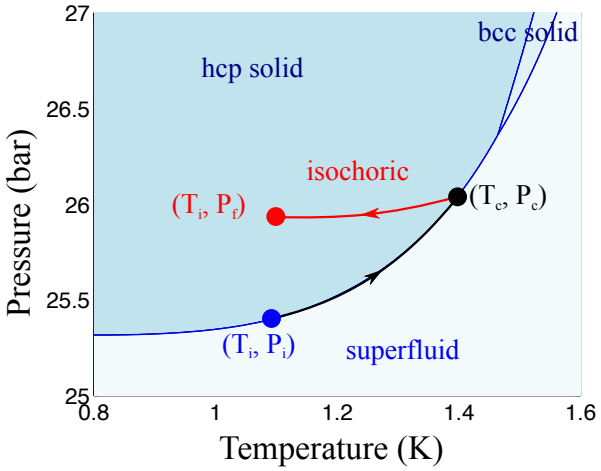

Fig.II.8 – A presentation of the crystal's growth process on the phase diagram. We bring the crystal seed from its initial state (T_i, P_i) to a higher pressure state (T_c, P_c), and grow the crystal at this state until the cell is filled with crystal. Then we slowly reduce the temperature so that the crystal follow the red isochoric line and finally reach the final state (T_i, P_f).

crystal so that the helium crystal loses its single-crystal character. So we decided to grow crystals at a higher temperature, $T_c = 1.4$ K. By pushing more helium into the cell, solid is produced in the injection capillary and acts as a mechanical plug. Then we can cool the cell through an isochoric process. Such a process is illustrated in Fig.II.8. Finally, after manipulating carefully during 3 hours, a good single-crystal can be produced. More details can be found in [2].

II.4 Local density measurement and Optical system

In 2011, our group had developed a "time-resolved quantitative multiphase interferometric imaging method" [1] to measure the local density of helium. Although our original objective was to investigate the metastable solid phase of helium, this method is also usable for metastable superfluid. There are many existent results in this domain, for example, Nissen *et al.* [41] used the diffracted light intensity and a modified *Raman-Nath* theory to calculate the local pressure. And Chavanne *et al.* [42, 43] have measured the instantaneous density at the acoustic focus on a glass plate. Compared to their cases, our method is purely homogeneous. It provides a new perspective for studying metastable phases of helium. In 2010, F. Souris *et al.* [44] have compared between the local density measured by our method and the one measured by a hydrophone in water, their results agreed within 5%.

Because local density measurement is the first step of our investigation for metastable helium, this method has determined the protocol of our optical system. For the comfort of reading, the presentation of our optical system is combined with the local density measurement. In this section, we will first present the local density measurement in both theoretical and technical aspects. Then I will show the original optical system and a typical experimental process.

II.4.1 From phase shift to density

The idea of measuring helium density initially comes from the relation between optical refractive index and local density variation. In electromagnetic theory, the *Clausius–Mossotti* relation relates the refractive index of a substance to its polarizability. Let n, ρ, m, and α be respectively the refractive index, the density, the single molecule mass, and the mean polarizability, then:

$$\frac{n^2-1}{n^2+2} = \frac{4\pi\alpha}{3m}\,\rho$$

We write it in perturbative form:

$$\frac{6n\ \delta n}{(n^2+2)^2} = \frac{4\pi\alpha}{3m}\,\delta\rho$$

We divide both sides by ρ then this equation reduces to:

$$\frac{6n\ \delta n}{(n^2+2)(n^2-1)} = \frac{\delta\rho}{\rho}$$

When the polarizability is small, that is $|n-1| \ll 1$ which is the case of helium, we finally have:

$$\frac{\delta n}{n-1} = \frac{\delta\rho}{\rho} \tag{II.1}$$

This formula shows that measuring helium local density is equivalent to measuring its local refractive index. Then our measurement of the local density of the metastable helium becomes an optical problem.

Our local density measurement is based on an interferometric technique. Let us consider a simplified case: Fig.II.9 is a sketch of a double path interferometer and the PZT. We take the acoustic focus as original point O, the propagation direction of the laser beam as the y-axis, and the x-axis to be perpendicular to the paper surface. Then the hemispherical-like PZT is axially symmetric with respect to z-axis. The observed interference fringes are directly related to the variation of phase shift $\delta\phi$ between the two separated beams. And it is an integral of the refractive index $\delta n(\mathbf{r})$ along y-axis, then $\delta\phi$ is a function of coordinates (x, z) such as:

$$\delta\phi(x,z) = \frac{2\pi}{\lambda}\int_L \delta n(\mathbf{r})\mathrm{d}\mathbf{r} \tag{II.2}$$

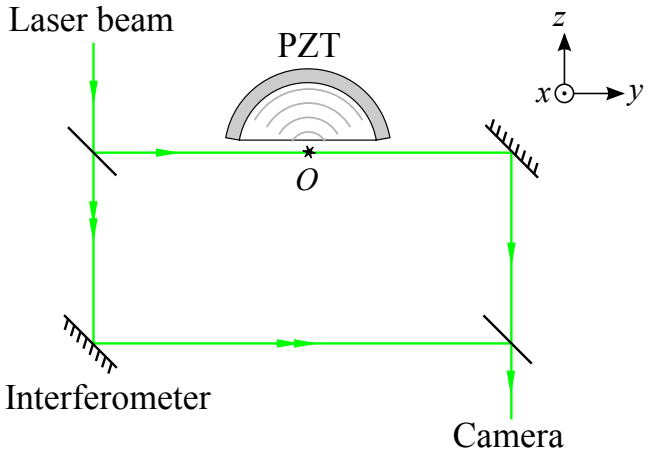

Fig.II.9 – A simplified plan of the interferometer. The incident laser beam is separated into two beams. One passes through the sound field induced by the PZT, and the other passes through an unperturbed zone. We can detect the interference at the end. A detailed description of the optical setup is given in Sect.II.4.3.2.

where δn is a function of position vector $\mathbf{r}$, and the integral is along the optical path L. In fact, we have to consider the diffraction of the light due to the sound field. In Sect.II.4.3.3, I will discuss the validity of the inverse Abel transform. Fig.II.10 is a figure of sectional plan x-O-y including the sound field, the z-axis is normal to the paper surface. We know that $\delta n(\mathbf{r})$ is due to the sound wave excited by the hemispherical-like PZT. Because of the rotational invariance of the sound field around the z-axis, $\delta n(\mathbf{r})$ depends only on the coordinate z and on the distance r to the z-axis. The extended laser light line is an optical path at coordinate (x, z). The observed phase shift at this point is the integral of δn from $-A(x)$ to $A(x)$. Then using Eq.(II.2), we have:

$$\delta\phi(x,z) = \frac{2\pi}{\lambda}\int_{-A(x)}^{A(x)} \delta n(\sqrt{x^2+y^2}, z)\mathrm{d}y, \text{ with } x^2 + A(x)^2 = R^2$$

which is also:

$$\delta\phi(x,z) = \frac{4\pi}{\lambda}\int_{x}^{R} \frac{\delta n(r,z)}{\sqrt{r^2-z^2}}\, r\mathrm{d}r \tag{II.3}$$

Apart from a factor $2\pi/\lambda$, the right side of this equation is the Abel transform of δn. And we can calculate δn by inverting Eq.(II.3) as explained in ref. [2]:

$$\delta n(r) = -\frac{\lambda}{2\pi^2}\int_{r}^{R} \frac{\partial\delta\phi(x)}{\partial x}\frac{\mathrm{d}x}{\sqrt{x^2-r^2}} \tag{II.4}$$

Finally, from Eq.(II.1) to Eq.(II.4), we establish the relation between local density and local phase shift.

$$\delta\rho = -\frac{\lambda}{2\pi^2}\frac{\rho_0}{(n_0-1)}\int_{r}^{R} \frac{\partial\delta\phi(x)}{\partial x}\frac{\mathrm{d}x}{\sqrt{x^2-r^2}} \tag{II.5}$$

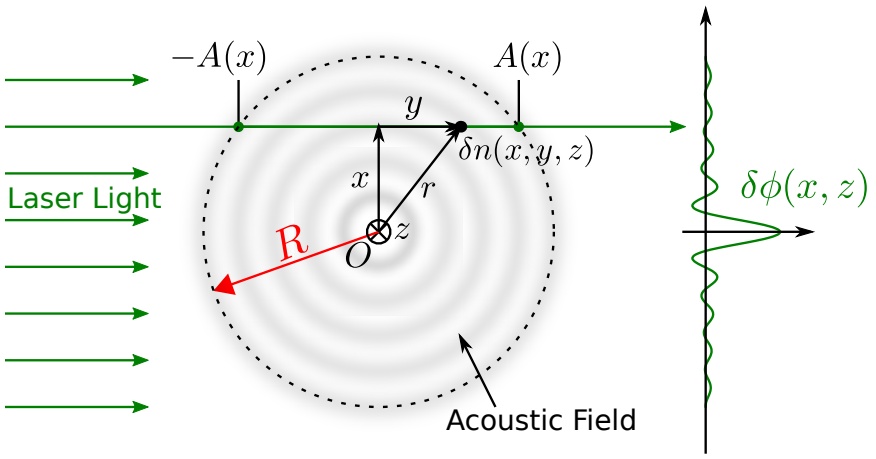

Fig.II.10 – The sectional plan of Fig.II.9, they share the same coordinate system. Laser beam propagates along y-axis. The sound field induced by the PZT is shown as blurred gray circles. The dotted circle R is the limit of the PZT, it defines the range of the sound field. On the right side of the figure, is the profile of $\delta\phi$ as a function of coordinate x.

where n_0 and ρ_0 are the initial values of refractive index and local density. The process of actually calculating this integral from experimental data is not at all simple, and is described in details in Fabien Souris' thesis [2].

II.4.2 Interferometer and multiphase technique

Eq.(II.5) converts phase shift into local density variation, so the former step has to be measuring the local phase shift induced by the sound wave. However a simple interferometer has the important disadvantage that it is very sensitive to the environmental noise and parasitic phase shifts due to, for example, dust on the windows. In order to circumvent this, the multiphase technique was developed. In this section, as the first part of our "time-resolved quantitative multiphase interferometric method", I will present our interferometer and phase plates in detail, which are used to precisely measure the local phase shift at a given time.

II.4.2.1 Jamin Interferometer

Amongst various types of interferometer, the Jamin interferometer was chosen. Compared to a Mach-Zehnder interferometer which has a minimum of 4 optics, a Jamin interferometer has only 2 thick mirrors. So it is less sensitive to external vibrations and eases the adjustment and installation.

Our Jamin interferometer is made up of two identical mirrors. These mirrors, with a thickness of $t_l = 15.75$ mm and a diameter of 50 mm, are made of BK7 whose refractive index is $n = 1.519$ at wavelength 532 nm. The back surface has

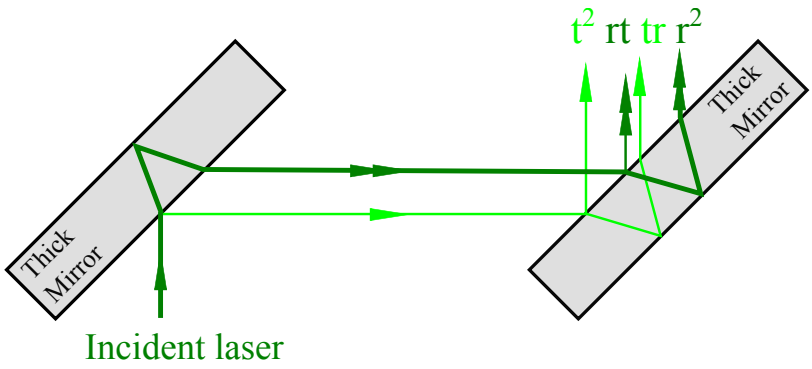

Fig.II.11 – Schematic plan of a typical Jamin interferometer. The two mirrors are parallel. While the first mirror separates the incident light into two beams, the second mirror combines them. In the figure, the second reflection of the two beams are marked with different colors and respectively noted by t^2, rt, tr and r^2. In reality, the rt and tr beams coincide and interfere.

high-reflection coating with reflection ratio more than 99.5%. The front surface is not coated and has a reflection ratio of 9.6% for light of incident angle around 45°. These two mirrors are placed at the same height with the same inclination angle 45° relative to the horizontal plane. Once an incident laser beam comes along the vertical direction, light undergoes multiple reflections inside the thick mirrors. If we only consider the first order reflection and transmission of the first mirror, incident light will be separated into a reference beam and another sample beam. These two separated beams will generate four output beams after passing through the second mirror. We respectively note r and t the reflective and transmissive amplitude rate ($r^2 + t^2 = 1$) which correspond to reference and sample beams. Let the incident beam be of unit electromagnetic amplitude. Then the four output beams can be marked as r^2, rt, tr, and t^2. If the two mirrors are adjusted to be parallel to each other, two of these four output beams, rt and tr would overlap and interfere. In this case, interference fringes are directly observable and phase shift between sample beam and reference beam could be measured.

II.4.2.2 Phase plate

Phase plates are also a device made by our group, which is used to quantitatively change the relative phase shift between the two beams of the Jamin interferometer. If we put a flat transparent glass (phase plate) on the path of one beam of the interferometer, it will increase its optical path length and change the phase shift between the two beams. As the refractive index of glass and thickness of the phase plates are known, this phase shift is a known function of the incident angle of light with respect to the phase plate. By controlling the inclination angle of

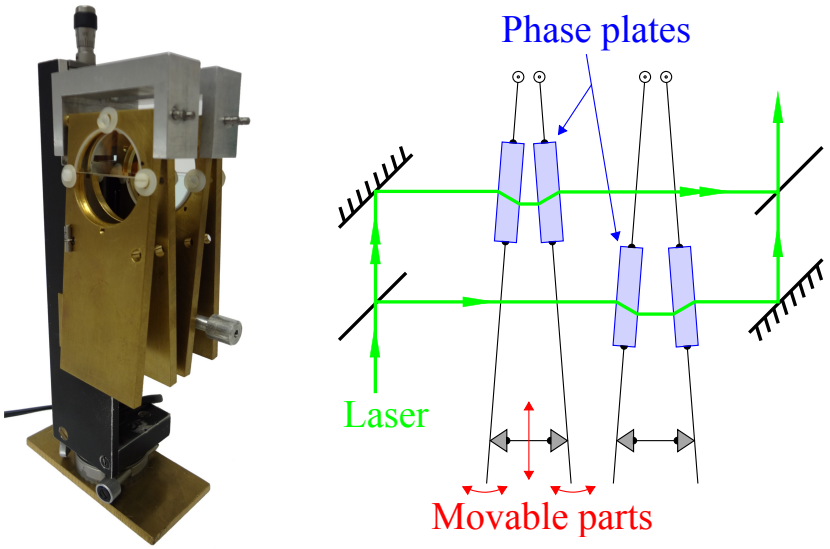

Fig.II.12 – Photo and schematic plan of phase plates and their support. Each phase plate is a half circle of 4 mm thickness and 40 mm diameter. Each pair of phase plates are made by cutting a flat circular glass window so that they have the same thickness and flatness.

the phase plate, we can quantitatively control the phase shift of the two parallel beams.

As shown in Fig.II.12, four transparent phase plates made of BK7 are mounted on two mechanical supports. Each support has a pair of symmetric phase plates. It is to compensate the vertical shift due to a single phase plate. In addition, the coherence length of our light source[6] is about 7 mm, which is on the same order as the optical thickness of two phase plates. So we also put another pair of phase plates on the other beam in order to have a better contrast of the interference fringes. This is why we have four phase plates in total.

On top of the support, there is a rotary shaft that connects two phase plates, so that they can rotate relative to each other around the shaft. The rotation of the phase plates is made by a vertically movable spacer which is at the bottom of the support. The spacer is a solid metal cube that is always in close contact with support. When we lift the spacer towards the shaft, it will push the two plates away and increase the open angle between two phase plates. The spacer is mounted on a numerical translation table which has a total translation length of 25 mm with a step of 0.1 μm. One pair of phase plates is fixed as reference, and its open angle is 5.5°. The other pair is equipped with the spacer. We can adjust its open angle from 5° to 6.5°, and give an additional phase shift to the Jamin interferometer up to $10 \times 2\pi$ rad with a precision of 1 μrad.

To obtain the expression of the phase shift added by the phase plates as

[6] A pulsed Nd:YAG laser

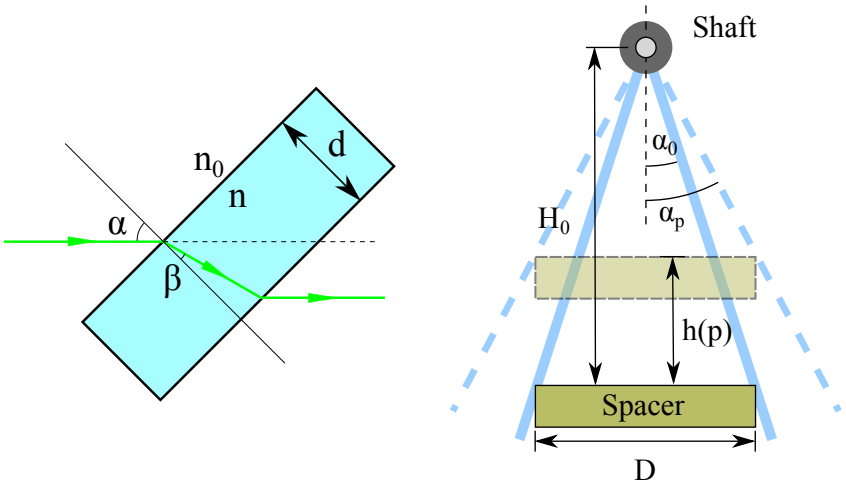

Fig.II.13 – Left: A horizontal laser beam passes through the inclined phase plate of thickness d. The incident angle α is the same as the open angle of phase plate. Right: The schematic plan of the spacer and phase plates' support. Blue lines show two different positions of phase plates, which correspond to two different open angles α_0 and α_p. H_0 is the initial distance between the spacer and the shaft axis, and h is the change of the spacer's height.

a function of spacer height, we first consider a simple optical model: a light beam passes through a thick glass. In the left side of Fig.II.13, the horizontal laser beam passes through the glass plate of thickness d. The incident angle is α. Let the refracted angle inside glass be β. Air and glass refractive index are respectively n_0 and n. Then the optical path δ added by *one* pair of phase plate is given by:

$$\delta(\alpha) = \frac{2n_0 d}{\cos\beta}\Big[\frac{n}{n_0} - \cos(\alpha-\beta)\Big] \approx 2n_0 d\Big[(\frac{n}{n_0}-1) + (1-\frac{n_0}{n})\frac{\alpha^2}{2}\Big] \qquad \text{(II.6)}$$

The right side expression is valid within the small angle approximation. In our case this condition is valid as the open angle is about 5°. Obviously, δ only depends on the phase plates' open angle α. By adjusting the position of spacer $h(p)$[7], we can control the open angle of the phase plates $\alpha(h)$. Let D be spacer's width and H_0 is the initial distance between spacer and rotary shaft. We have:

$$\alpha_0 = \frac{D}{2H_0}\ , \text{ and } \ \alpha_p = \frac{D}{2(H_0-h)}$$

As described above, two pairs of phase plates are respectively mounted on each path of the interferometer, the total optical path added to the interferometer is

[7] p is the step number of spacer, it can be regarded as a parameter that directly controls the spacer height h.

the difference of $\delta(\alpha_0)$ and $\delta(\alpha_p)$, which is:

$$\Delta = \delta(\alpha_p) - \delta(\alpha_0)$$

Using Eq.(II.6), and the relation $h \ll H_0$, we immediately have:

$$\Delta = \frac{n_0 d D^2}{4H_0^2}(1 - \frac{n_0}{n})\frac{h(p)}{H_0}(1 + \frac{h(p)}{2H_0})$$

By substituting all the constant variables, we can deduce the phase shift ψ induced by the phase plates as a function of phase plate spacer height $h(p)$:

$$\psi(p) = \frac{2\pi}{\lambda}\Delta = 2\pi\frac{h(p)}{a}(1 + s\frac{h(p)}{a}) \tag{II.7}$$

where ψ_0 is the initial phase, $a \approx 3.7$ mm and $s \approx 0.04$, which are determined by the geometry. However, the parameters a and s both depend on the incident angle of the beam which is not easy to measure. So we regard them as free parameters in the regression analysis which will be explained in the next paragraph.

II.4.2.3 Quantitative multiphase technique

Experimentally, the phase shift due to the sound wave is obtained by measuring the laser intensity $I(p)$ as a function of the spacer height $h(p)$. Let us consider the signal received by the camera at a given time t. Although the entire image received by the camera has thousands of pixels, we only consider one pixel. Because the following reasoning is valid for all pixel if the conditions for the inverse Abel transform are valid. As already mentioned once, I will discuss these conditions in the end of this section.

In ideal case, which means there is no background noise light and the light is monochromatic, the intensity of the combined beam can be written as:

$$I = (I_1 + I_2)\Big[1 + \frac{2\sqrt{I_1 I_2}}{I_1 + I_2}\cos(\Delta\phi)\Big]$$

where I is the observed intensity, and I_1, I_2 are the sample and reference beam intensities, $\Delta\phi$ is the phase shift between the two beams. In fact, because of parasitic terms, this formula is not exact. But it can always be written in a general form:

$$I = I_{eff}\Big[1 + C_{eff}\cos(\Delta\phi)\Big] \tag{II.8}$$

where I_{eff} is the effective intensity and C_{eff} is the effective contrast.

In our experiment, the total phase shift $\Delta\phi$ is the difference of two terms[8]:

$$\Delta\phi(p) = \phi - \psi(p) \tag{II.9}$$

[8]The minus sign is because ϕ and ψ are respectively added to the sample beam and the reference beam.

$\psi(p)$ is the phase shift brought by the phase plates, which is a function of the spacer position, and we denote it by the position number p. And ϕ is the phase shift between the two beams , which can be decomposed to two terms:

$$\phi = \phi_{static} + \phi_{sound}$$

where ϕ_{static} is the static phase shift between two beams, and ϕ_{sound} is the one added by the sound field. Then using (II.9), we can rewrite (II.8) by developing its cosine term:

$$I(p) = I_{eff}\Big[1 + C_{eff}\cos\phi\ \cos\psi(p) + C_{eff}\sin\phi\ \sin\psi(p)\Big] \tag{II.10}$$

As mentioned in Sect.II.4.2.2, the value of $\psi(p)$ is determined by Eq.(II.7). And we extract the variables a and s from a regression analysis. We first measure the interference intensity by changing the position of the spacer without sending any sound in helium. Experimentally, we measure 25 images corresponding to 25

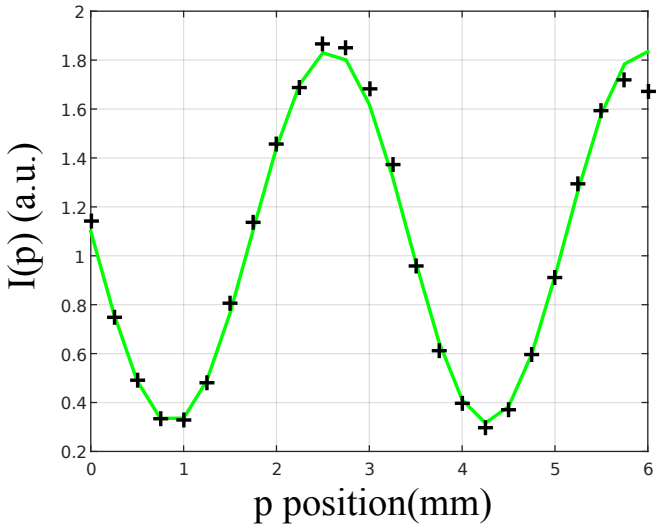

Fig.II.14 – The cross data points are the measured intensity $I(p)$ as a function of p. The green curve is the corresponding sinusoidal regression of the free parameters in Eq.(II.7). These two parameters depend on the inclination angle between the phase plates and the laser beam, which is very difficult to measure.

gradually increasing values of $h(p) = \{h_1, h_2, h_3 \ldots h_{25}\}$. Eq.(II.7) shows that the corresponding $\psi(p)$ will also increase. Consequently, the observed intensity $I(p)$ will change periodically as the cosine term $\cos\psi(p)$ does. Fig.II.14 is a typical result of this regression analysis. Once we have obtained $\psi(p)$, we also use the same regression analysis to extract the phase shift ϕ from the interference images taken with sound. For the convenience of computation, we replace I_{eff}, C_{eff},

and ϕ terms by D, E, and F, and rewrite Eq.(II.10) in the following form:

$$I(p) = D + E\cos\psi(p) + F\sin\psi(p)$$

The simplest way is to measure $I(p)$ at three different p, as Eq.(II.10) has three unknown variables. However, one advantage of our multiphase technique is the efficiency, as we can implement dozens of measurements in a very short time by repeating the experiment for different p. More measurements bring a more precise result. So in fact, in a series of measurement, we measure $I(p)$ for 25 different p, then a simply linear regression will gives D, E and F so that we can compute:

$$\phi_{static} + \phi_{sound} = \arctan\frac{F}{E}\ ,\quad C_{eff} = \frac{\sqrt{E^2+F^2}}{D}\ ,\quad I_{eff} = D$$

The phase shift ϕ_{static} can be measured by taking images without any sound wave, and we can obtain ϕ_{sound}. Finally, by substituting the result into Eq.(II.5), the local density of helium comes to light immediately.

II.4.3 Time-resolved technique and imaging system

Sect.II.4.1 showed how we calculate the local density from the local phase shift by the inverse Abel transform for a given pixel of the camera at a given time t. In numerical computation, the precision of the inverse Abel transform is determined by the spatial and temporal resolution of the data. In this section, I will discuss these two kinds of resolution in our experiments.

II.4.3.1 Time-resolved technique

The acoustically driven metastable phase of helium is a state far from equilibrium conditions. Its observation is determined by the duration of the sound wave. In our set up, sound frequency is 1.15 MHz, so the observation of a typical metastable phase is on the order of a microsecond.

The acquisition frequency of our CCD camera is 10 Hz, which is much longer that the duration of the metastable phase of helium. The camera is not able to continuously record the local density at the microsecond scale. However, as acoustically bringing helium in metastable states is a reproducible phenomenon, we can still obtain a movie of the metastable event at microsecond scale using a so-called time-resolved technique. We use a pulsed laser to measure the sample at a given time t. Note that this laser pulse duration 9 ns is much shorter than the lifetime of metastable helium event, so during this detection time, we consider the detected signal as a snapshot of sample at time t. Then we repeat a series measurements at successive delays $t+\delta t$, $t+2\delta t$,... etc.. At last we can rebuild the complete time evolution of this event. Here δt is the time interval between

two successive detections, which is also the temporal resolution of our system. We choose it to be equivalent to 1% of the duration of the metastable phase, that is about 0.05 μs.

II.4.3.2 Imaging system

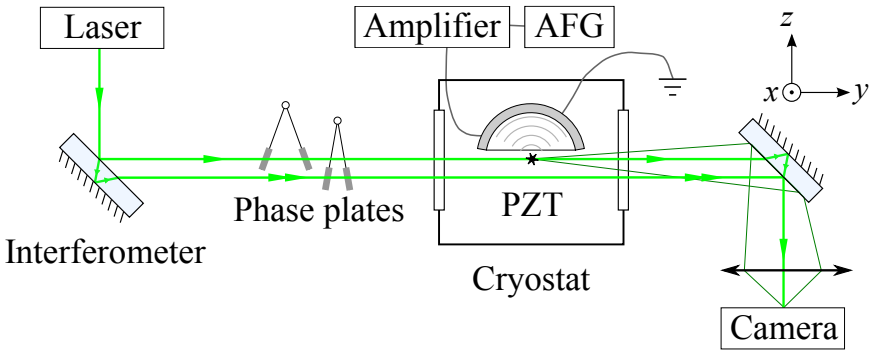

Fig.II.15 – Scheme of the entire optical system. At the center of the transducer, the small star is the acoustic focus. A CCD camera monitors the focus plane through a lens.

Fig.II.15 shows a scheme of the entire optical system. We use a pulsed Nd:YAG laser ($\lambda = 532$ nm) as a light source to directly illuminate the sample. Its pulse duration is 9 ns, the repetition frequency is 20 Hz. After passing through the first interferometric mirror and the phase plates, two parallel beams go into the experimental cell. The square in the center of figure represents the optical cryostat and the experimental cell. Inside the cell, the PZT excites and focuses acoustic waves in helium at frequency of 1.15 MHz. One side of the transducer is grounded and the other side is connected to the output of a RF amplifier driven by an arbitrary function generator (AFG). This generator is a core device for time-resolved technique and the synchronization of the system. In fact, it is enabling for adjusting the time delay between input and output signal from 1 ns to 1000 ms with a precision up to 1 ns.

As described above, incident light is separated into two beams. The sample beam passes through the acoustic focal region while the reference beam crosses the cell in an unperturbed zone. These two beams merge and interfere after being reflected by the second interferometric mirror. The center plane x-O-z of the sound field, which we also call the "focal region", is imaged onto the CCD camera by an appropriate lens system. This lens system has been designed so that its spatial resolution does not exceed 25 microns. Our group also experimentally checked that this spatial resolution is $\delta x \simeq 20$ μm [2]. Compared to the sound wavelength in liquid helium, $\lambda_s \simeq 0.20$ mm, this resolution is high enough.

II.4.3.3 The conditions of the inverse Abel transform

We have already mentioned that the model used in Section.II.4.1 is valid only if the diffraction of light due to the sound wave is negligible. In the acousto-optics, the diffraction due to sound wave can be divided into two different regimes, one is called the *Bragg* regime, the other is the *Raman-Nath* regime. Each of them has different criteria. So our first step to investigate the diffraction of light is to check if the sample can be considered as a thin optical grating. This is called the *Raman-Nath* condition [45, 46], which states that the light diffracted at the beginning of the grating does not shift more than half the spatial period of the grating.

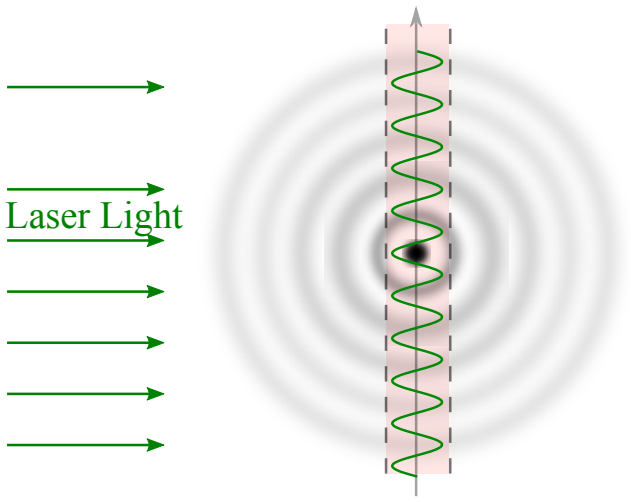

Fig.II.16 – Diagram of the simplified sound field. The amplitude of phase modulation radially increases as $1/r$. Roughly speaking, only the central red zone contributes to the light diffraction. Then we can further simplify that in the dashed line zone, the phase modulation is uniform.

To check if it is indeed the case, we consider the following scenario. First, we compute the different diffractive orders as if the sample were effectively thin. Let the real thickness of the sample be L. In our case, as the radial sound field is concentrated towards the center and the amplitude varies reciprocally as $1/r$. So the sound amplitude away from the focus center is very small, we can then neglect this part. And also, if the sound wave front is perpendicular to the incident direction, it will make a low contribution to the diffraction, and we can also neglect this part. As shown in Fig.II.16, after neglecting these two parts, we simplify the radial sound field to sinusoidal grating with Λ being the sound wavelength, which is perpendicular to the laser beam and can be written as:

$$\phi(x) = \phi_0 \sin(\frac{2\pi x}{\Lambda})$$

We get three ordersrepresented by a diffraction angle α such as $\alpha = \lambda/\Lambda$ where λ is the laser wavelength. The *Raman-Nath* condition is then:

$$L\alpha = \frac{L\lambda}{\Lambda} < \frac{\Lambda}{2}$$

Since the sound field is highly concentrated at the focus, whose typical length is serveral Λ, only a zone of thickness of the order of Λ will effectively contribute to the diffraction, so the *Raman-Nath* condition reduces to:

$$\lambda < \frac{\Lambda}{2}$$

and with $\lambda = 532$ nm, $\Lambda \approx 200$ μm, this is, by far, true.

As the phase modulation amplitude grows, we have to take into account higher diffraction orders. Indeed, we can consider that side orders diffracted at the beginning of the thick grating will be diffracted again by the neighboring slices of the thick grating. Higher orders of diffraction are thus gradually "populated" as light travels through the grating. Eventually, if the phase modulation amplitude is high enough, high orders that do not pass through the collecting optics because their scattering angle is too high will have to be considered. Fabien Souris has proposed a very simple way to address this problem. Consider the same sinusoidal phase modulation as above:

$$\phi(x) = \phi_0 \sin(\frac{2\pi x}{\Lambda})$$

This corresponds to a modulation of the wavefront function:

$$z(x) = \frac{\lambda}{2\pi}\phi(x)$$

And the maximum slope of this modulation corresponds to the highest implicated diffraction orders. This slope is:

$$\alpha = \frac{\mathrm{d}z}{\mathrm{d}x} = \frac{\lambda}{2\pi}\phi_0\frac{2\pi}{\Lambda}\cos(\frac{2\pi x}{\Lambda})$$

Its maximum value is:

$$\alpha_m = \phi_0\frac{\lambda}{\Lambda}$$

This should remain lower than the angular aperture of the optics, which is related to its spatial resolution δx by $\theta = \lambda/\delta x$. The condition on ϕ_0 is then:

$$\phi_0\frac{\lambda}{\Lambda} < \frac{\lambda}{\delta x}$$

that is:

$$\phi_0 < \frac{\Lambda}{\delta x} \simeq 10 \text{ rad}$$

As we will see, this is always the case.

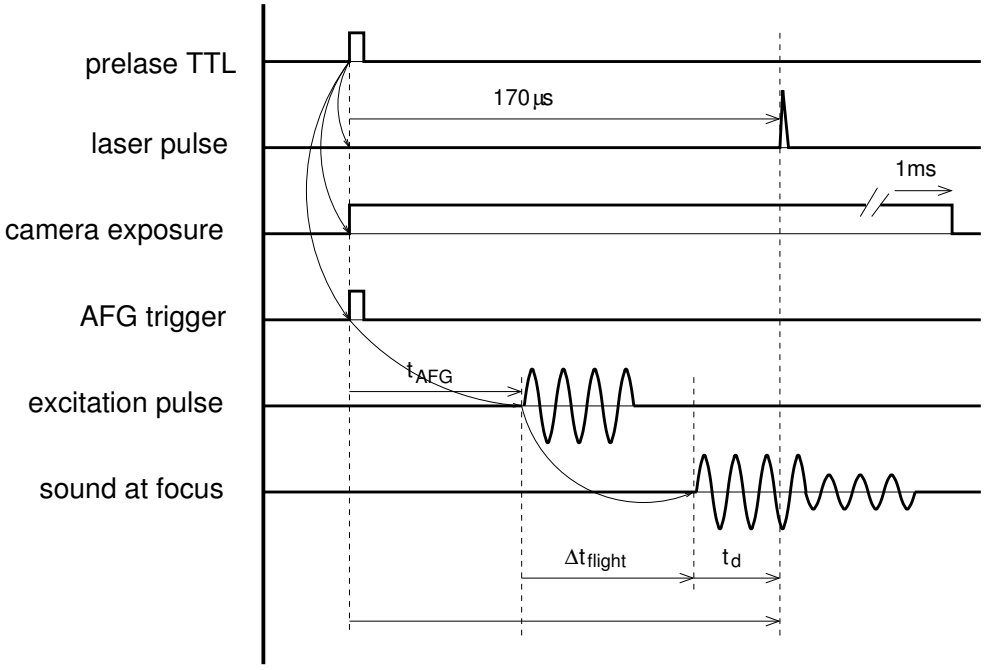

Fig.II.17 – The time line in a single measurement. The time arrow is towards right. 1) Initial trigger at t_0, it precipitates the camera the AFG and the amplifier. 2) After the delay t_{AFG}, the sound wave sent by the PZT. 3) After the time of flight t_{flight}, the sound wave arrives at the focus. 4) The laser pulses at the pre-lasing time t_{pulse}, and an image is captured at this time.

II.4.4 Experimental process

Our experimental protocol consists of the two main parts that was described in the last two sections. It is the "time-resolved quantitative multiphase interferometric method". Before performing any measurement, we need to synchronize our complex optical system.

A single measurement is to take an image of the focal region at a given time t and spacer position p of phase plates. Fig.II.17 gives the timing of a single measurement. Our pulsed laser has a pre-lasing signal that will be sent $t_{pulse} = 170$ μs before the laser pulse. This signal is set as the initial trigger of the entire system. And it will precipitate three actions. The first one is the exposure of the CCD camera, which has a much longer duration than 170 μs. The second is a TTL gate signal sent by AFG, which is used for activating the RF amplifier. The last one is a RF burst signal also sent by AFG, which is amplified by the RF amplifier and then excites the PZT, it determines the time of sending the sound wave.

The opening of the camera and the TTL gate signal are both executed at the initial trigger time. So only the time of sending the sound wave concerns

us the most. Let the initial trigger time be time zero. Then the laser pulse is at time $t_{pulse} = 170$ μs. If we want to capture the instantaneous image of the first arrival of sound wave at focus, we have to consider the time of flight of sound wave. In superfluid helium, for pressure 1 bar, this time is about: $\Delta t_{flight} = R/c_{sound} \approx 26$ μs, where R is the PZT radius, and c_{sound} the sound velocity. So we should send the RF burst at time $t_{pulse} - \Delta t_{flight}$. We call this time t_{AFG}, as it is controlled by the AFG.

Let t_d be the time interval between the arrival of the sound wave at focus and the laser pulse. Keep in mind that the discussion above is made to capture the instantaneous image of the arrival of the sound wave at focus, which is $t_d = 0$. If we want to capture an earlier or a later time, we can simply change the delay t_{AFG}. And from the above discussion, we can write:

$$t_d = t_{pulse} - \Delta t_{flight} - t_{AFG} \tag{II.11}$$

This equation shows that t_d could be considered as the time reference of how long it has been since the first sound wave front arrived at the focus. This notation is very practical when we study the bubble lifetime in helium in Chap.V.

Next step is to measure a series of images at different times and a constant spacer position p. By adjusting t_{AFG}, we can easily change t_d at every single measurement. As mentioned earlier, our temporal resolution of measurement is about 0.05 μs, so a typical series of measurement consists of hundreds of single measurements at successive time delays $t_d = \{t_{d1}, t_{d2}, t_{d3}, \ldots\}$. After that, we will perform 24 other series of measurement at 24 different values of $p = \{p_1, p_2, p_3 \ldots p_{24}\}$.

To summarize our experimental process, we have 25 series of measurement at different spacer position p, and each series is composed of hundreds of images at successive delays. Because our default sound burst repetition frequency is 10 Hz, if there are 200 images to record in a series of measurement, and we take the initializing of the spacer position into account, then it takes about 30 s for one run. Then the total experimental time for 25 runs is about 15 minutes. If we want to have a higher temporal resolution measurement, we should use a smaller time step, and it will significantly increase the amount of images in each run. Consequently, the total experiment time will increase up to several hours.

Chapter III

Study of the metastable solid helium

Introduction

The former PhD student of our group, F. Souris had succeeded in bringing solid helium into a metastable state [1]. This is a very interesting experiment, because metastable solid helium in a low density state seems to be a good candidate for a possible supersolid state (see Chap.I). As already mentioned, the metastable solid helium was achieved by using our manufactured PZT to focus sound wave in solid helium. We found that the crystal breaks only 4.4 bar below the melting pressure, and a small region ($\sim$ 0.1 mm) is irreversibly damaged. However, this experimental result does not match the theoretical expectation of H. Maris who predicted that perfect helium crystals should remain metastable down to 35 bar below the melting pressure [26]. This instability was studied in numerous crystals at various temperatures between 0.9 K and 1.4 K. The existing imaging protocol allowed us to precisely locate the damaged region at the very focus of the sound wave, where shear is zero and pressure swing maximum [2]. However, it was based on a standard CCD camera and was neither suitable for determining the appearance time of damage, nor its growth dynamics. In particular, it remained

unproven that the instability occurs during a negative swing of the pressure oscillation. For that purpose, a different detection method had to be developed.

III.1 Experimental method

The new imaging system allows us to precisely determine when the instability occurs and, to some extent, its growth dynamics. Interesting conclusions can be drawn from their dependence on the amplitude of the sound wave. To detect events at a microsecond time scale, we have implemented a standard Schlieren imaging technique.

III.1.1 Schlieren method

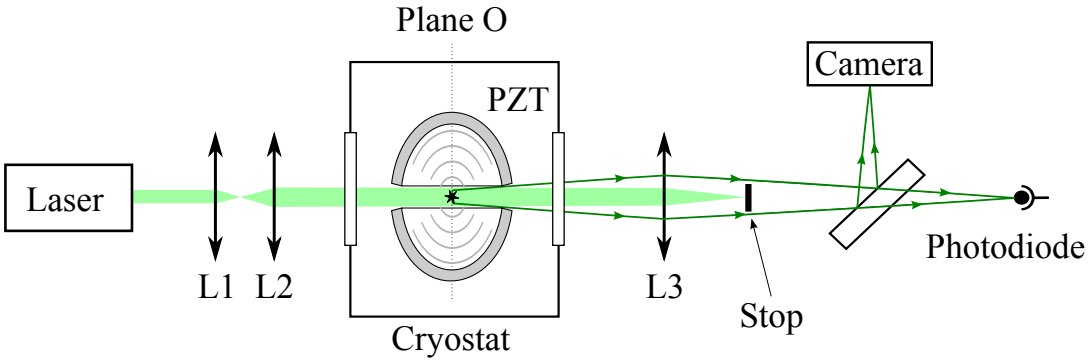

Fig.III.1 – Experimental arrangement to monitor the light scattered by the damaged region (plane O) at a microsecond time scale. The beam of a CW laser, expanded by two lenses (L_1 and L_2), illuminates the region where the instability occurs. The unscattered light is focused by L_3 and absorbed by a beam stop, while the light scattered by the damage is collected by a fast photodiode. Using a semi-transparent plate, images of plane O can be simultaneously recorded on a standard CCD camera.

Unlike the 10 Hz pulse laser (8 ns width) used in the previous protocol, we use a continuous wave (CW) laser beam ($\lambda = 532$ nm) to illuminate the focal region. The detector of the present experiment is a fast photodiode (~ 5 MHz bandwidth) instead of the CCD camera. This photodiode is placed at the image plane of the sound focus through a corrected lens assembly. This lens focuses the parallel laser beam onto an opaque beam stop (diameter 1.8 mm). Consequently, only the light scattered by the damage would be detected. The entire set-up is shown in Fig.III.1. In addition, a semi-transparent mirror allows us to get simultaneously an image of the region of interest on a CCD camera. It is used to check whether the instability really occurs.

In order to increase the signal to noise ratio, care is taken to avoid parasitic light by illuminating only the region of interest. To that end, a two lens beam expander combined with an adjustable diaphragm is used. The waist after L_2 is located $\sim$ 100 cm downstream which is near the PZT focal region, and its divergence is $\sim$ 0.6 mrad. The Rayleigh range is about 150 cm. Note that the stop diameter is larger than what is required by the beam divergence. It is designed to stop also the light scattered by the sound wave in the focal region at an angle $2\lambda/\lambda_s \simeq 2.5$ mrad.

III.1.2 Experimental process

All the experiments were performed at $T = 1.06$ K and $P_{static} = 25.50$ bar. The static pressure is 0.12 bar above the fusion pressure at this temperature. The experimental process is also slightly different from the protocol described in Chap.II. First, we prepare a single crystal in the experimental cell so that the PZTs are completely immersed in it. The crystal is then brought to the chosen state by the technique described in Sect.II.3.2. The crystal quality is controlled by checking the focalization of sound waves using the interferometric method described previously. This is done at a low enough driving voltage ($V_{PZT} \sim 40$ V) that the crystal remains undamaged. Typical lowest local pressures achieved are about 2 bar below the melting line. The position of the sound focus is then determined on the interferometric images.

The CW laser beam used in the Schlieren imaging measurement is centered on the sound focus. The beam diameter measured at plane O is $d = 0.7 \pm 0.1$ mm, while the typical maximal size of the damaged region is 250 μm.

The synchronization of the system is also slightly different to the protocol described in Sect.II.4.4. Because the pulsed laser was not used in this study, we used a generator as initial trigger instead of the pre-lasing signal. As mentioned before, it triggers the camera, the AFG, and the RF burst. In addition, it triggers a mechanical chopper that opens the CW laser beam during 50 ms. This time is small enough to avoid cell heating, and long enough to detect any forthcoming scattering event and assess the long term evolution of the damage. A few milliseconds later, the two PZT receive a four oscillation electrical excitation at their resonance frequency 1.25 MHz. In the solid the sound velocity is between 300 and 500 m/s depending on its propagation direction so that $\Delta t_{flight} = 12\mu$s.

The photodiode output is recorded on a digital oscilloscope, triggered at $t = 0$ by the beginning of the radio frequency excitation. Fig.III.2(a) displays several signal examples corresponding to different driving voltages of the PZT. Due to non linear effects, this voltage is not directly proportional to the wave amplitude but is used only for benchmarking. For every signal, the contribution of the background stray light is measured at lower driving voltage and then subtracted from the actual signal. A sharp increase of the scattered light signals the damage occurrence at t_0.

III.1.3 Determining t_0

To determine precisely t_0, we have fitted the beginning of curves like those of Fig.III.2(a) with a quadratic function :

$$V_{photo}(t) = \mathcal{H}(t - t_0)\, a\, (t - t_0)^2 + b$$

where a, b and t_0 are free parameters and $\mathcal{H}$ is the Heaviside function. The fit is performed for each instability on a time interval from 0.8 μs before the signal rise to the point where it reaches half the first relative maximum. In the limit of Huygens-Fresnel diffraction, the intensity of the light scattered by a damaged region of diameter d is expected to be proportional to d^2. If d grows linearly in time, we thus expect that the signal first starts growing as $(t-t_0)^2$. The inset of Fig.III.2(a) gives an example of such a fit. Typical uncertainty on t_0 is 0.02 μs, i.e. less than 2.5% of the sound period. The value t_0 given by the fit is taken to be the time of occurrence of the instability.

To provide a temporal reference for the sound pressure at the focal point, Fig.III.2(b) represents the pressure variations of the crystal previously recorded using the interferometric method at lower driving voltage. This signal is used for time calibration.

III.2 Experimental results

On the recordings shown in Fig.III.2, the instability starts on a depression, i.e. in a domain of the helium phase diagram where the stable phase is the liquid phase. Once the damaged region is created, its size oscillates with the wave pressure. But it does not come back to zero afterwards, having undergone an irreversible growth. Its size remains finite at the end of the pressure wave. The crystal is irreversibly damaged.

We have reproduced this kind of measurement to determine the time of birth for 20 instabilities at different driving voltages of the PZT. The results are shown in Fig.III.3. They confirm that the instabilities always start on a depression swing of the sound wave. This result gives strong support to the hypothesis that this instability corresponds to the nucleation of some 'drop' of another phase, presumably the liquid one, inside the bulk of solid helium. We also remark that for a given driving voltage, the times of birth of the instabilities are all within the same negative swing of the sound pulse. But, as the driving voltage is increased, t_0 jumps from one negative swing to an earlier one.

III.3 Discussion

We attribute this behavior to the existence of a pressure threshold triggering the instability: this threshold would be reached earlier in the sound wave as the

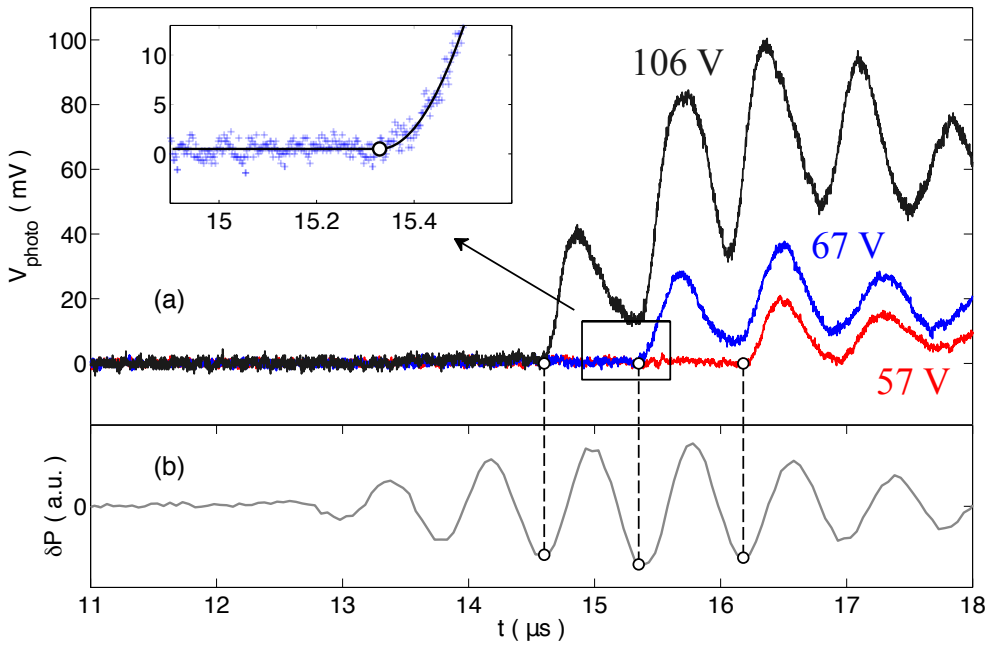

Fig.III.2 – a) Photodiode voltage as function of time for 3 experiments creating solid helium instabilities at different PZT driving voltages. The sharp increase of the signal corresponds to the appearance of damage. The open circles give the time of birth t_0. Inset: Typical fit of the photodiode voltage as function of time using Eq.(III.1.3). b) Pressure variations at sound focus in arbitrary units for temporal reference.

wave amplitude is increased. Moreover, at low excitation driving voltage (50 V or less), thousands of sound pulses can be sent into the crystal without damaging it [1]. It seems to support the existence of a pressure threshold.

However, the results shown in Fig.III.3 are not consistent with such a simple scenario. For the seven experiments performed at the lowest driving voltage (V_{PZT} = 57 V), the instability systematically starts during the oscillation *after* the one of minimum pressure. If a threshold did exist, the 57 V instabilities would have nucleated at least one oscillation before the one observed. Even if we assume that there is only some probability of breaking during a certain swing, as soon as the amplitude is large enough, this result doesn't seem compatible with a simple threshold. Indeed, the two preceding oscillations have amplitudes equal or larger than the one where events are observed. Attributing equal probabilities for a nucleation event in each of these oscillations (which is a conservative hypothesis), the probability for 7 events lying in the last oscillation would be only $(1/3)^7 \simeq 5 \times 10^{-4}$. This is rather unlikely and we thus conclude that the instantaneous pressure is not the only physical quantity which triggers the instability.

Looking for a physical quantity which remains constant for the different observed events, one may remark that the time spent under stress compensates in

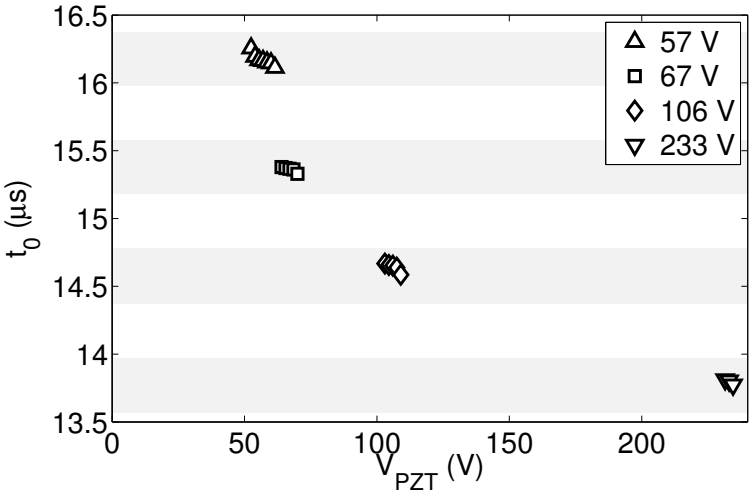

Fig.III.3 – Times of birth t_0 of 20 instabilities at different driving voltages of the PZT. For clarity, the symbols for a given excitation voltage are slightly horizontally dispersed around their nominal values. Error bars are within the data point sizes. Gray areas: Time intervals of negative swings of the pressure wave at sound focus.

some way a lower depression amplitude. This is reminiscent of fatigue effects, more precisely of Wöhler fatigue curves [47]. In a fatigue test, a piece of material is submitted to an alternating stress of amplitude S_r until it breaks after N cycles. The Wöhler curve presents S_r as a function of N in log-log coordinates. It decreases from the static rupture stress towards the plasticity threshold of the material for very large N.

In conclusion, we have shown experimentally that the observed instability in metastable hcp solid helium indeed appears during the depression swing of the sound wave for which the stable phase is the liquid phase. Moreover, we have found that this instability cannot be associated with a simple depression threshold. This part of work was published on [48].

Chapter IV

Study of metastable superfluid helium

Introduction

Although our “time-resolved quantitative multiphase interferometric method" was initially developed for studying metastable solid helium, it can be used to study the metastable superfluid phase. As already mentioned in Sect.I.3, superfluid helium is a model liquid for investigating condensed matter theory. Especially, the metastable superfluid helium has been studied in detail in order to check the nucleation theory (see the review article [30]).

There are two kinds of metastable phases for superfluid helium. One is the over-pressurized liquid phase, in which we squeeze the superfluid intending to observe the nucleation of a helium crystal. The other is to bring the liquid to a negative pressure so as to create helium vapor bubbles. The later one is related to the spinodal limit of the liquid, in which the condensed liquid phase become totally unstable. This limit is usually deduced from the equation of state of the superfluid helium at negative pressure. Many theorists used different approaches, and obtained similar equations of state at zero temperature. Since our method could measure the local density of the metastable helium, we decided to study the stability limits of the superfluid helium hoping to find a cavitation density being consistent with others.

This chapter is organized as follow: I will first present the preliminary study about two different metastable phases of the superfluid helium. It is followed by the detailed study of cavitation limit in superfluid helium. To our surprise, during the study of the cavitation limit, we found an interesting problem which will be discussed in the end of this chapter.

IV.1 Over-pressurized superfluid helium

IV.1.1 Existing experimental results

In the past few years, to our knowledge, there have been only a few studies of homogeneous nucleation of the solid helium in over-pressurized superfluid helium. Most of them were performed by the group of S. Balibar in Paris[1]. In 2004, F. Werner *et al.* focused bursts of 1 MHz acoustic waves by a hemispherical PZT [49], and they studied the possible nucleation of bubbles or crystals by shining laser light through the acoustic focal region, and by using a photomultiplier as a detector to capture the scattered light due to the nucleation. Since they could not measure directly the local pressure of the helium, they estimated the pressure at the focus by assuming the pressure to be proportional to the driving voltage of the PZT. Then by analyzing the dependence between the critical driving voltage and the static pressure, they could find out whether the signals is due to a bubble or a crystal. But to their surprise, they found no evidence of the nucleation of a helium crystal up to about 160 bar. This value is much larger than the one predicted by the standard nucleation theory (65 bar) [50].

Later, in 2006, R.Ishiguro *et al.* (the group of S. Balibar) implemented a similar experiment and criticized the result of F. Werner *et al.*, at last they came to an opposite conclusion. They mentioned "...we now think that this (the conclusion of F. Werner *et al.*) needs to be further checked and their conclusion possibly corrected...", and attributed this to the possible non-linear effect of the

[1]Laboratoire de Physique Statistique de l'ENS, Paris, France

acoustic waves which weakens their estimation of the local pressure. Therefore, for the same reason, they did not give the threshold of the nucleation pressure.

For now, this problem is still open, and it also becomes one of the starting points of our study.

IV.1.2 Experimental set up

Our preliminary experiment is based on the local density measurement described in Chap.II. In principle, we would observe the acoustic focus without the interferometer so as to see whether a crystal/bubble appears. Once we found something unusual, we would launch a local density measurement.

As mentioned in Sect.II.2.1, two face-to-face grinded hemispherical PZT focuses acoustic waves in liquid helium. They are held by the PVC support in the experiment cell. The pulsed laser is synchronized with the AFG and the camera, so as to take a snapshot at a given delay.

As a preliminary observation, our goal was to find any possible evidence for a crystal in the images. To do so, we repeated the experiment in different conditions. Since there are many controllable variables, such as the temperature and static pressure, driving voltage applied on the PZT, and observation delay, our group developed a program to display the camera images in real time. It allows to rapidly repeat the experiment at different driving voltages and time delays.

In addition, differing from the experiments of the S. Balibar's group, we did not need to estimate the local pressure of the liquid through the driving voltage applied on the PZT. The direct measurement of this driving voltage is then unnecessary. Moreover, in order to precisely control the driving voltage of the PZT[2], we fixed the signal amplifier gain factor at 390, and adjust only the AFG voltage amplitude with a relative accuracy of 10^{-4}. Hence we use the AFG voltage V as the scale to indicate the threshold voltage instead of the PZT driving voltage.

IV.1.3 The equation of state

However, a simple result of the local density does not allow to compare it with the result given by the theories or other experiments (they all give the threshold pressure instead of density). So we have to convert the density to pressure by the equation of state which was initially given by H.Maris *et al.* [37, 38]. The one we used in the context is the later one fitted by F. Caupin *et al.* [51].

$$P - P_c = \frac{b^2}{27}(\rho - \rho_c)^3 \tag{IV.1}$$

[2]A small reminder: the RF burst is amplified before it is sent to the PZT.

where P and ρ are helium pressure and density. For liquid ^{4}He , $b = 1.4030 \times 10^6 \mathrm{g}^{-1}\mathrm{cm}^4\mathrm{s}^{-1}$, $P_c = -9.6435$ bar and $\rho_c = 0.094175$ g.cm^{-3}. Because this equation is mainly intended to describes the behavior of ^{4}He at negative pressure, perhaps its not accurate enough for the over-pressurized helium. Actually, there are not many results dedicated in the equation of state for over-pressurized helium. So far we only found one given by L. Vranjes *et al.* [52]. It is obtained by a Monte Carlo simulation and gives a pressure value larger than the extrapolation of the experimental equation of state from the low pressure region. So the converted pressure should only be regarded as an estimation.

IV.1.4 Results

However, the search of crystal nucleation in superfluid did not go well. In fact, we use a CCD camera to capture helium images. Differing from the experiments done by the photodiode [53, 49], what we observed is the entire image of the focus zone. We have tried hundreds of combination of static temperature, pressure, driving voltage and time delay. We did not find any obvious trace of crystal nuclei. But we still found some suspicious signals. We call them suspicious because we did not have full evidence to prove the appearance of a crystal.

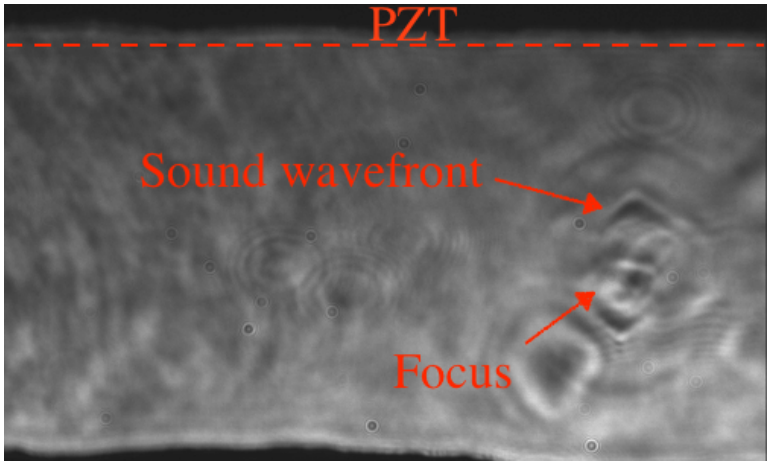

Fig.IV.1 – A raw image taken at $T = 1.05$ K and $P_{static} = 25.14$ bar (the solidification pressure is 25.37 bar), time delay $t_d = 20.13$ μs. The AFG voltage $V = 745$ mV. The upper stripe is the border of the PZT. The acoustical focus is on the right side of the image. The sound wavefront is also shown in the image.

Fig.IV.1 is a typical raw image in this experiment. We noticed that there are some triangular structures which are indicated in the image. They are suspected to be the shadow of sound wavefronts, because these structures would move forward or backward as we increase or decrease the observation delay, and they always propagate on radial direction. But, since the phase modulation due to the

sound amplitude is usually too small to scatter the light, why would we observe shadows of the wavefront? I think there could be two reasons. One is our highly focused sound wave has non-linear effects, possibly shock waves, that scatters the incident light. In fact, C. Appert *et al.* has reported strong non-linear effects found in the simulation of focused large amplitude sound waves [43]. Due to the non-linear effects, the gradient of the sound amplitude could be large enough to scatter the light, so we observed the shadow. The other reason is our grinded PZT. Perhaps it is too much grinded and loses the spherical symmetry. As the geometry of the wavefront changed, it would possibly change the way it scatters the light.

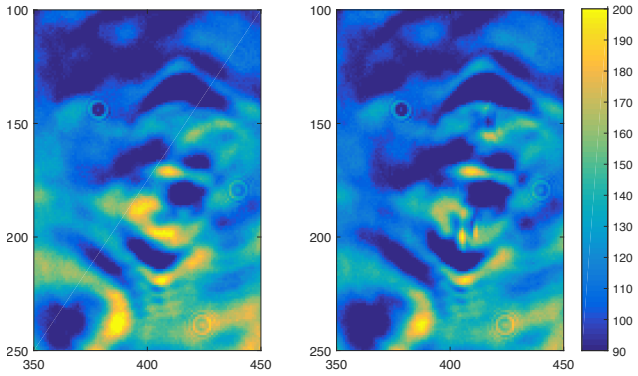

Fig.IV.2 – Partial zoom of the acoustic focus of two raw images. Both images are taken at $T = 1.05$ K and $P_{static} = 25.14$ bar, time delay $t_d = 3.73.$ μs. But their AFG voltage are different: left $V_1 = 745$ mV; right: $V_2 = 820$ mV. The left one is the same one shown in Fig.IV.1. The color bar is an arbitrary unit indication of the light intensity.

Fig.IV.2 shows the partial zoom of the acoustic focus region for two different AFG voltages. They were taken at the same $t_d = 3.73$ μs, which corresponds to the maximum over-pressurized swing. As already mentioned in Sect.II.4.4, it is the delay between the observed time and the arrival time of the sound wavefront. We found that, at lower AFG voltage $V_1 = 745$ mV (the image at left of Fig.IV.2), there was no evident structures at the focus. At higher voltage $V_2 = 820$ mV, there was some small fringes at the focus (the one at right of Fig.IV.2). In order to clearly show this signal, I present the profiles of the intensity on Fig.IV.3. In the profile of 820 mV, there is a peak around the pixel (405,191) which corresponds to the sound focus of the upper PZT. As indicated on the right side of the figure, there is another similar anomaly around the pixel (420,150). These anomalies only appear at higher AFG voltage in the two focal regions, so we suspected them to be a possible nucleation of the crystal.

In addition, the two separated focuses are due to the two PZTs being not perfectly con-focal which has already been mentioned in Sect.II.2.1.

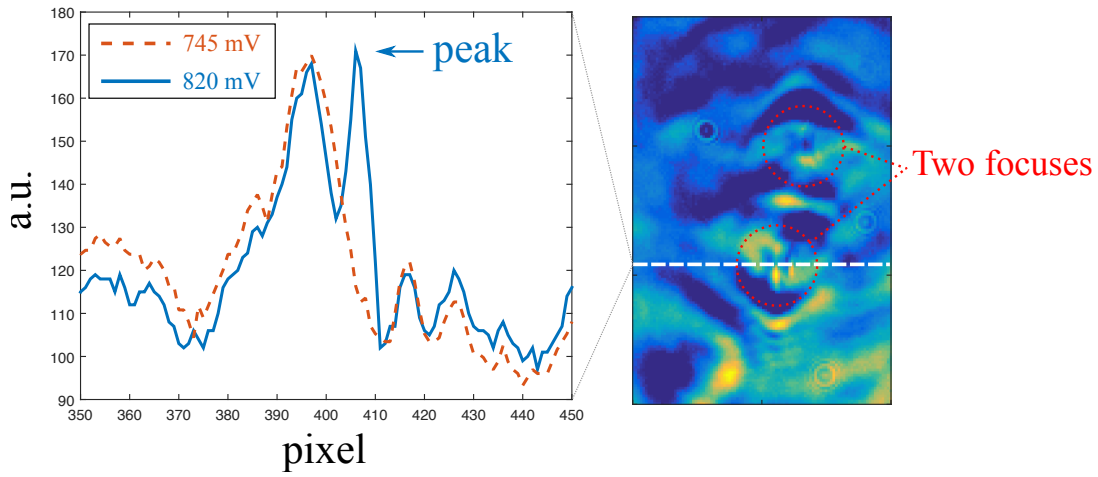

Fig.IV.3 – The profiles of light intensity for the same row of the two images shown in Fig.IV.2. Because the sound wave amplitudes are different in the images, we normalized the light intensity by multiplying one image by a factor so that most pixels of the curves are overlapped. The red dotted line is the profile of $V_1 = 745$ mV, and the blue line is the profile of $V_2 = 820$ mV. There is an abnormal peak around the pixel (405,191). On the right side, the horizontal line shows the position of the row. And the two circles are the two separated focuses.

IV.1.5 Discussion

Unfortunately, we did not find any decisive evidence of the crystal nucleation in over-pressurized superfluid helium. We attribute the inconclusive result to two main reasons. The first one is that the highly deformed sound wavefront greatly influenced the image contrast, which makes the event signal difficult to be detected. The second one is that the upper and lower sound wave fronts are not perfectly aligned. The two focuses are separated apart from each other a distance of 400 μm, and it is about one and a half sound wavelength. This defect makes the two counter propagating sound wave no longer in-phase, and weakens focusing.

Nevertheless, we could still measure the local density when the suspicious structure appears and then convert it to local pressure by using Eq.(IV.1). We found that, at $T = 1.05$ K, the pressure range at which we obseve the suspicious structure varies from 44 bar to 62 bar depending on the static pressure. We also noticed that the threshold pressure of the nucleation crystal predicted by the standard nucleation theory is about 65 bar at zero temperature.

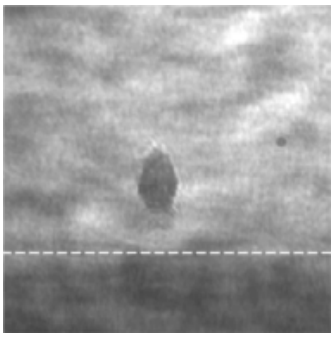

Fig.IV.4 – Image of a cavitation bubble, taken at $P_{static} = 0.05$ bar, $T = 0.93$ K, $t_d = 20.0$ μs, the AFG voltage $V = 660$ mV. The lower dark strip is the PZT border.

IV.2 Cavitation bubble in superfluid helium

After the inconclusive search for crystal nucleation, we turned to study the cavitation in superfluid helium. In theoretical aspects, many researchers studied the so-called spinodal limit of superfluid helium, which could be experimentally examined. At zero temperature, various theoretical approaches [54, 55, 56, 57] have produced quite similar equations of state. So a direct measurement of the cavitation limit could possibly help us to give more insights to this study. All the existing results in this domain were given as cavitation pressures. So in order to compare with other experimental results, we also have to convert our measured density to pressure using an equation of state. To our surprise, our converted pressure does not quite agree with previous estimations. Thus we also reproduced the pressure extrapolation of F.Caupin and S.Balibar [51], and found a reasonable agreement with their data. After discussion of various sources of uncertainties in our measurements, we compare our results with various theoretical estimates of the cavitation pressure.

IV.2.1 Preliminary observation

In this series of experiments, we slightly modified the experimental set up. Instead of using two over grinded PZT, we put only one single PZT on the support. The new PZT was only grinded a small part of 0.9 mm height along the equator (see Sect.II.2.1), so it could keep the sound wavefront quite spherical.

It is known that cavitation in superfluid helium will give birth to a helium bubble. In our experiments, without exception, when we increase the driving voltage on PZT above some value, we observed a helium vapour bubble at the acoustic focus. Our time-resolved technique allows to observe the image of bubble at any give delay. Fig.IV.4 shows a typical photo of bubble. Similar to the case described in last section, these photos are taken without interferometer.

In our preliminary experiments, we learned that cavitation is a temperature dependent stochastic process. This result has already been predicted in the standard nucleation theory, and other groups have already observed the same behavior [58, 51]. What we do is to verify this result by our own devices. As expected, we found that, around a critical driving voltage, the probability to see a bubble is not always 1. Our result on the cavitation probability will be presented in next section.

IV.2.2 Determining the cavitation voltage

Our measurement of local density by interferometry requires a completely reproducible phenomenon. If bubbles appear randomly, it is impossible to measure the optical phase shift $\delta\phi(t)$ for the pixels involved. In other words, this method only allows us to measure the local density just below the cavitation density where no cavitation process occurs (or the cavitation probability is very low). Then the measured local density should be very close to the real cavitation density and a linear extrapolation to the cavitation voltage would introduce only a small correction.

Thus, before performing any density measurement, we have to precisely determine the cavitation voltage. Other groups have observed that bubble life time in superfluid helium depends on the static pressure P_{static} and is of the order of some tens of microseconds [41, 59].

According to our recent research about bubble lifetime of helium liquid, this lifetime in superfluid helium mainly depends on the hydrostatic pressure. In our case bubble can be clearly seen by camera $\sim 10\,\mu$s after the minimum pressure wave front passed the acoustic focus, because bubbles will expand to about 100 μm and are easily observed on the CCD camera. In 1998, H. Lambaré *et al.* [58] proposed to fit the cavitation probability by an "asymmetric S-curve formula":

$$\Sigma(V) = 1 - \exp[-\ln 2 \exp(\xi(V/V_c - 1))] \tag{IV.2}$$

where V is the excitation voltage, V_c the cavitation voltage and ξ is the inverse width of the curve.

In order to determine V_c, we proceed as follows. For a given static pressure, the bubble probability is determined for 5 different excitation voltages. Each voltage point corresponds to 1000 trials (1000 sound pulses) and the probability is then simply given by the number of positive events (creation of bubble) divided by the number of trials. To simplify the counting of bubbles, we made a computer program, which calculates a mean light intensity of a small region around the acoustic focus. Because the bubble is always created and then collapses at the acoustic focus[3], once a bubble appears in this small region, the total light intensity will significantly decline. By choosing a proper threshold of the mean

[3]The behavior of the bubble will be described in Chap.V.

intensity, the program could easily count the bubble probability. We also noticed

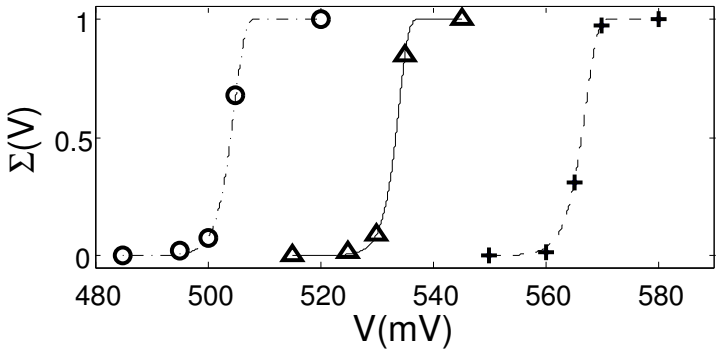

Fig.IV.5 – Cavitation probability at 0.96 K for three different pressures P_{static}: circles 0.15 bar, triangles 0.65 bar, crosses 1.26 bar. The corresponding lines are fits according to Eq.(IV.2).

that, as the cavitation is a thermally activated process, the probability is very sensitive to the temperature changes. To avoid heating, 10 bursts of 100 sound pulses at 10 Hz repetition rate were shot, waiting 100 s between each burst.

The cavitation voltage is the value corresponding to a bubble probability of 1/2 according to Eq.(IV.2). As can be seen in Fig.IV.5, the relative width of the curves is about 1% of V_c. These curves are indeed very sharp. So if we want to make a local density measurement without bubbles, the available maximum AFG voltage V_{max} should be about 2% below V_c, such as

$$V_{max} \approx 0.98 V_c$$

In this situation, the probability $\Sigma(V_{max})$ is about 10^{-3}.

IV.2.3 Cavitation density

Fig.IV.6 is a radial density profile at $P_{static} = 0.15$ bar at a given time t_d, it is obtained by the local density measurement. The local density at zero radius is the minimum density at P_{static} and t_d. Then the minimum density in time and space ρ_{min} was measured for several voltages below the cavitation threshold. An example is shown in Fig.IV.7. Assuming a local linear dependence of ρ_{min} to V near V_{max}, and taking into account the error bars, we can safely consider ρ_{cav} is $\rho_{min}(V_{max})$.

Finally, the cavitation density was reached from three different static pressures: 0.15 bar, 0.65 bar and 1.26 bar, and at the same temperature 0.96 K as shown in Fig.IV.8.

Fig.IV.9 is the same 13 data, and they are averaged for each static pressure.

Within the error bars we find that ρ_{cav} is independent of P_{static}. We computed the mean of these measurements and their mean squared error to determine, respectively, the cavitation density of helium and its uncertainty. Our

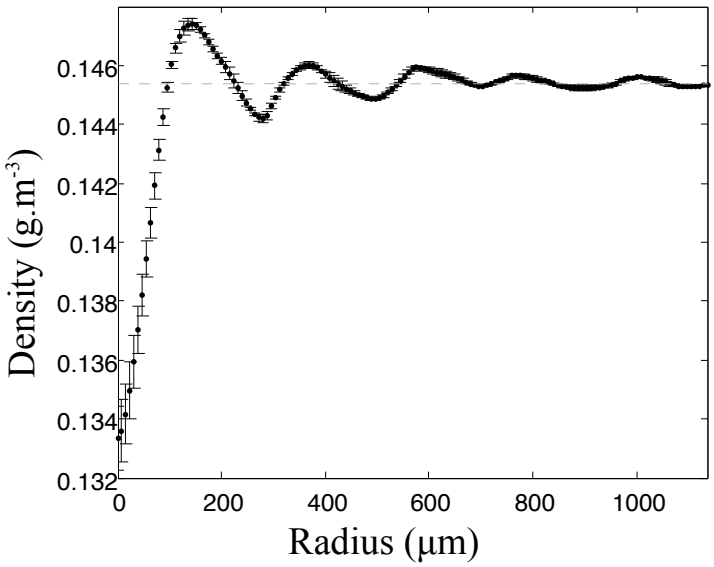

Fig.IV.6 – Typical radial density profile for $P_{static} = 0.15$ bar at the time when the density is minimum at acoustic focus. The static density corresponding to P_{static} is shown by the horizontal dashed line.

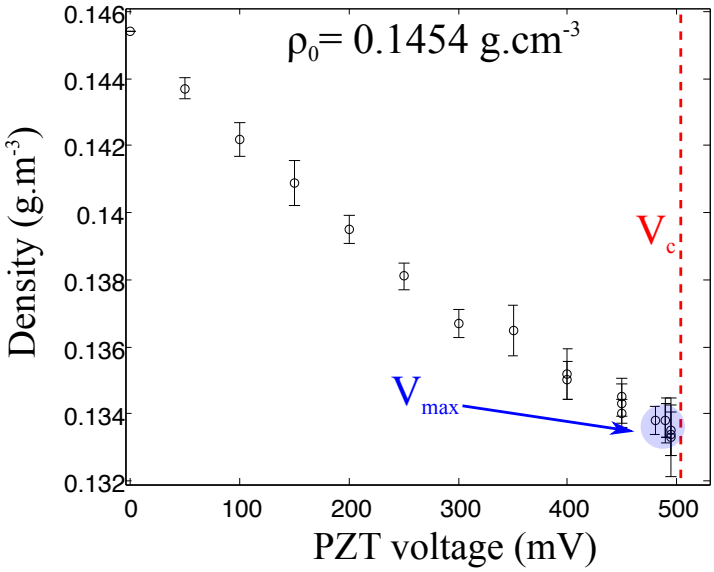

Fig.IV.7 – Experimental measurements of minimum densities ρ_{min} for different driving voltages V at $T = 0.96\,\mathrm{K}$ and $P_{static} = 0.15\,\mathrm{bar}$. The data points in the blue circle are the measurements at V_{max}. The dashed red line represents the cavitation voltage V_c.

final result is that the cavitation density of superfluid ^{4}He at 0.96 K $\rho_{cav} = 0.1338 \pm 0.0002$ g.cm^{-3}. In these three different pressures, the static density does not change much and has the value of about $\rho_{static} \approx 0.146$ g.cm^{-3}. The relative

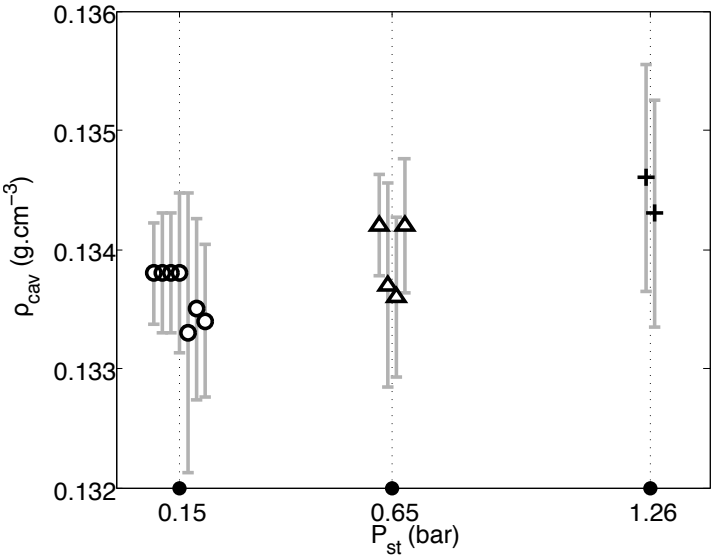

Fig.IV.8 – 13 measurements of the cavitation density at three different P_{static}. For more clarity, the different measurements are shifted from their actual P_{static} values.

difference of ρ_{cav} and ρ_{static} is:

$$\frac{\Delta\rho}{\rho_{static}} = \frac{\rho_{static} - \rho_{cav}}{\rho_{static}} = 8.4\%$$

And we can state that superfluid helium around 1 K will break when its local density is lowered by about 8.4%.

In addition, we many ask whether the cavitation density is really independent of the pressure. As shown in Fig.IV.9 the data points can also be fitted by a slightly inclined straight line. If we accept such assumption that ρ_{cav} depends on P_{static}, we will find the difference between the fit line and the data points is too small compared to the error bars. Normally, a such a fit should be considered as a coincidence. In fact, with these data points, we can not deny either assumption, and in the near future, we will perform more experiments to check this.

IV.2.4 Uncertainty analysis

Before analyzing the measurement uncertainties, we should first discuss the condition of the inverse Abel transform. As already mentioned in Sect.II.4.3.3, the amplitude of the phase modulation due to the sound wave should satisfy $\phi_0 < 10$ rad. Whereas the measured minimum density corresponds to a maximum phase modulation $\phi_0 \approx 5$ rad. So the inverse Abel transform is valid in our case.

The measurement uncertainties can be divided in two parts: the statistical ones which come mainly from the extraction process of the optical phase shift

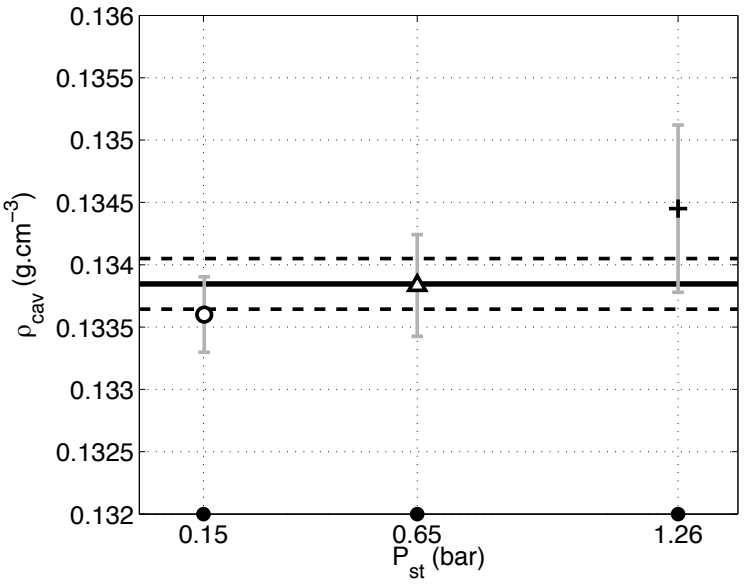

Fig.IV.9 – Same data as Fig.IV.8, but data points are averaged for each pressures.

induced by the acoustic wave, and the systematic errors arising from an imperfect cylindrical symmetry of the pressure wave.

As we mentioned in Sect.II.4.3, for each time and for each pixel, the phase shift value $\delta\phi\,(t)$ is obtained by applying a fit on intensities using Eq.(II.10). We use a computer program to extract these phases with 95% confidence bounds. This gives the phase shift uncertainties mainly due to shot noise, camera reading noise and laser power fluctuations. Once the phase shift map is determined, an inverse Abel transform is applied to recover the refractive index local variation induced by the acoustic wave(see Sect.II.4.1). Then, the density variations are deduced from the optical index variations using Eq.(II.1). The inverse Abel transform is a linear transformation, from its expression Eq.(II.4) we can see that the calculation of the optical index at a given pixel i depends linearly on the phase shift values for all pixels on the same line. The local density variation at this pixel is thus in the form:

$$\delta\rho_i = \sum_{j=i}^{j_{max}} \alpha_{ij}\delta\phi_j$$

where j is the pixel index and α_{ij} is a weight. The errors $\Delta\delta\rho_i$ on $\delta\rho_i$ can be computed from the error $\Delta\delta\phi_j$ on $\delta\phi_j$ and the weights α_{ij} which could be in principle extracted from the Abel inversion program. Instead we used a simpler empiric method, assuming that the phase uncertainty is about the same for each pixel, and is not correlated from one pixel to an other. In that case, the

uncertainty of the density variation at the pixel i is:

$$(\Delta\delta\rho_i)^2 = \sum_{j=i}^{j_{max}} \alpha_{ij}^2 \, (\Delta\delta\phi_j)^2 = (\Delta\delta\phi)^2 \sum_{j=i}^{j_{max}} \alpha_{ij}^2$$

Then, we performed $N = 1000$ density calculations, for the same treated line while adding a Gaussian noise to the phase shifts for every calculation. The standard deviation of the added noise is chosen to be the same as the phase shift uncertainty $\Delta\delta\phi$. Once we have these N treatments, the statistical uncertainty $(\Delta\delta\rho_i)_N$ of the radial density variation is calculated for each pixel of the line. By construction, this uncertainty is equal to $\sqrt{2}$ times the original unknown statistical uncertainty $\Delta\delta\rho_i$ of the density variation, because:

$$(\Delta\delta\rho_i)_N^2 = \sum_{j=i}^{j_{max}} \alpha_{ij}^2 \left[(\Delta\delta\phi)^2 + (\Delta\delta\phi)^2\right] = 2\,(\Delta\delta\rho_i)^2$$

Applying this method, we found that the statistical uncertainty δ_{stat} around the cavitation density is on the order of $2 \times 10^{-4}\,\mathrm{g.cm^{-3}}$, while the maximum value of $\delta\rho$ is of order 125×10^{-4} g.cm^{-3}.

The inverse Abel transform assumes that the symmetry axis is exactly known. Actually, it is unknown and has to be determined experimentally by searching a symmetry axis in the phase maps. But the phase noises as well as any possible asymmetry of the acoustic wave locally perturb the left-right symmetry of the phase shift maps. This perturbation will add an uncertainty in the calculation of density variations. The difference between the Abel inversion applied to the left and to the right of this axis gives an order of magnitude of this uncertainty.

The symmetry axis for a given phase map is found by fitting a straight line through all symmetry centers when the amplitude of the sound pulse at focus is maximum. Then the mean and the standard deviation for the position of these axis are computed.The uncertainty on the symmetry axis is about 3 μm, giving a contribution to the density variation uncertainty on the order of $3 \times 10^{-4}\,\mathrm{g.cm^{-3}}$. To this systematic uncertainty we add another incertitude due to the difference between the left and right parts of the Abel inversion. This gap varies from one image to another and it is on the order of $5 \times 10^{-4}\,\mathrm{g.cm^{-3}}$. So the uncertainty of the symmetry axis is about $\delta_{sym} = 8 \times 10^{-4}$ g.cm^{-3}

At last, we have the total uncertainty for one single measurement: $\Delta\delta\rho = \sqrt{\delta_{sym}^2 + \delta_{stat}^2} \approx 10^{-3}$ g.cm^{-3}.

This analysis is an example of how we deal with the uncertainty. The value given here might change in different measurements. In fact, we have respectively calculated the uncertainty for every single measurement. The error bars of the three data points shown in Fig.IV.9 are calculated independently. The final uncertainty is calculated by assuming that the cavitation density is independent of the static pressure. Therefore, we have $\Delta\delta\rho_{total} = 2 \times 10^{-4}\,\mathrm{g.cm^{-3}}$

Note that, this value compared to the density variation $\delta\rho$ gives a relative uncertainty about 2%. Concerning the reliability of this measurement, it may

be interesting to recall that a comparison with a hydrophone [44] was made in water in 2010. It was found that the deviation between the two methods is less than 5%.

IV.2.5 Discussion

Previous results [51, 60] about cavitation in liquid helium were given as cavitation pressures instead of cavitation densities. The equation of state (EOS) of liquid helium in its metastable state (density and pressure below the boiling curve values) is needed to convert the ρ_{cav} to a corresponding P_{cav}. Although such an equation of state has never been measured experimentally, as I mentioned earlier in Sect.IV.1.3, some have been proposed. H. Maris has pointed out that, in the stable phase at $T = 0.1\ K$, the sound velocity pressure dependence could be fit very well by the law $c^3 = b(P - P_c)$ with c the sound velocity, P the pressure, P_c the spinodal pressure and b a constant [61]. He proposed that this relationship holds in the metastable state (negative pressure).

$$P - P_c = \frac{b^2}{27}(\rho - \rho_c)^3$$

where P and ρ are helium pressure and density. For liquid ^{4}He , $b = 1.4030 \times 10^6 \mathrm{g}^{-1}\mathrm{cm}^4\mathrm{s}^{-1}$, $P_c = -9.6435$ bar and $\rho_c = 0.094175$ g.cm^{-3}. Bauer *et al.* have performed Path-integral Monte Carlo simulations of liquid helium in the metastable state at finite temperature and found the same dependence of sound velocity on pressure [56]. Dalfovo *et al.* have calculated the EOS of metastable liquid helium at $T = 0\ K$ using density-functional approach [55], and Boronat *et al.* using a quadratic diffusion Monte Carlo method to achieve a similar EOS [54]. The EOSs at 0 K agree within a few percent. Moreover, using the density-functional theory of Dalfovo *et al.*, Maris and Edwards have shown that in the temperature range $0 < T < 1\ K$, the EOS is nearly independent of temperature [57].

So in order to compare our cavitation density result to cavitation pressure results of other experiments, we use the well established EOS of metastable liquid helium at $T = 0\ K$ and assume it holds for $T = 0.96\ K$. By doing so, our cavitation pressure is $P_{cav}(0.96K) = -5.1 \pm 0.1$ bar.

At temperatures ∼1 K, in addition to the present experiment, there are to our knowledge only two experiments which studied the cavitation of liquid helium. Both also used focused acoustic wave. Xiong *et al.* [60] found the cavitation pressure at 1 K is ~ -3 bar. The incertitude mentioned in this paper is about ±10% and comes mostly from the difficulty of estimating the pressure at acoustic focus knowing the displacement of the emitter. Non-linear effects were not taken into account in their calculation. So this incertitude is likely to be underestimated. Caupin *et al.* [51] studied the dependence of cavitation voltage to the static pressure. They claim that this method enables them to set an upper limit

for the actual cavitation pressure. Modelling a linear response of their emitter to voltage, they also give a lower limit for the cavitation pressure. Their result is $-9.8 < P_{cav}(0.9K) < -7.7\,\text{bar}$. According to the data points published in [50], the result at $T \sim 1$ K is almost the same. One can see that there are large discrepancies among these experiments.

We have tried to reproduce the experiment of F.Caupin *et al.* using their extrapolation method on P_{static} [51] (see Sect.IV.2.6). The upper limit of P_{cav} we found is about $-8\,\text{bar}$ which agrees pretty well to the one of F.Caupin *et al.* (see next section). But the disagreement with our density measurement converted to pressure remains.

Jezek *et al.* [62] have calculated the cavitation pressure of liquid helium as a function of temperature, by using a density functional method and assuming the absence of defects (especially vortices). In order to compute the cavitation pressure, the volume υ and the time τ in which nucleation is likely to occur are needed. We take $\upsilon = (\lambda_s/2)^3$ and $\tau = 0.1\ \mu$s is the 1/10 of the sound period. This gives $\upsilon\tau \sim 10^{-13}\ \text{cm}^3\text{s}$. Using this $\upsilon\tau$ value, Jezek *et al.* calculated $P_{cav}^{Jezek}(0.96K) \sim -6.9\,\text{bar}$. This value is just between our result (-5.1 bar) and the central value (-8.8 bar) of F.Caupin *et al.*.

Finally, we would like to point out that Maris has developed a model of cavitation in the presence of quantized vortices in liquid helium [63]. For a vortex density ranging from 10^4 to $10^{12}\,\text{cm}^{-2}$, he founds that $-5.8 < P_{cav}^{vortices}(0.96K) < -5.1\,\text{bar}$. Although Maris can not estimate the error bar on this simulation, we note that our result does lie in this range. Besides, Pettersen *et al.* [64] have proposed that the vortex density in the high amplitude sound wave should be of the order of $10^8 \sim 10^{10}\,\text{cm}^{-2}$. The presence of vortices might be a possible way to conciliate our experimental result with simulations. However, this would imply that, in the presence of vortices, the P_{static} extrapolation method of reference [51] does not give an upper limit of P_{cav}.

IV.2.6 Cavitation pressure by extrapolating the static pressure

In 2001, F.Caupin *et al.* implemented an extrapolation method [51] to investigate the behavior of helium in negative pressure. They imagined an environment with a "stable" negative static pressure. In this situation, the required driving voltage for achieving cavitation would be less than the one in null static pressure. Then the very negative static pressure corresponding to zero cavitation voltage would be the cavitation pressure. That can be expressed as:

$$P_{cav} = P_{focus} = P_{static} + \Delta P\,(\rho_{static} V_c)$$

where P_{cav}, P_{static} and P_{focus} are respectively the cavitation pressure, the static pressure of helium and the pressure at acoustic focus. $\Delta P\,(\rho_{static} V)$ is the variation of pressure induced by the sound wave and ρ_{static} is the static density.

This equation holds when the driving voltage V reaches the cavitation voltage V_c. Assuming that the cavitation pressure is independent of P_{static}, we measure the different cavitation voltages at different static pressures, and then extrapolate linearly at zero cavitation voltage [4]. Numerical simulations [65] have shown that in absence of vortices the true curve is concave toward negative pressures. The linear extrapolation gives an upper limit of the true cavitation pressure. The Fig.IV.10 shows our extrapolation corresponding to our measurements of

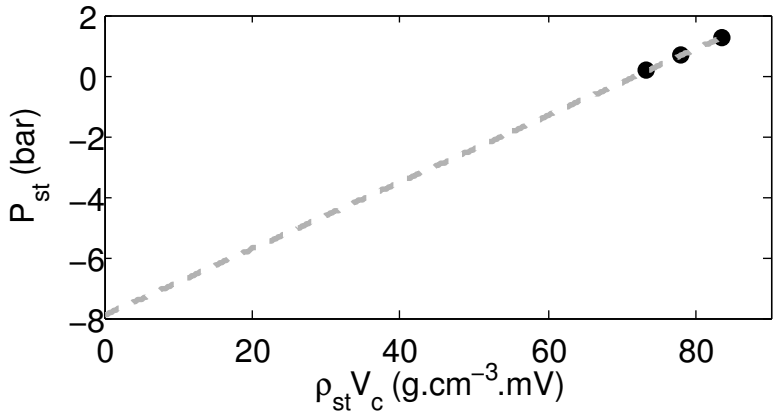

Fig.IV.10 – Reproduction of reference [51] experiment. P_{static} as function of $\rho_{static}V_c$. The 3 data points(black circles) correspond to static pressures of 0.15 bar, 0.65 bar, 1.26 bar. Cavitation voltage are the ones shown in Fig.IV.5. The dotted line is the linear extrapolation of the data points.

(P_{static},V_c) values at $T = 0.96$ K (see Fig.IV.5). The upper limit of cavitation pressure obtained in this way is -7.9 ± 0.3 bar. This is in agreement with F.Caupin *et al.*'s value which is $P_{cav} < -7.7$ bar at 1 K.

IV.3 Conclusion

We have preliminarily investigated two different metastable phases of superfluid helium expecting to observe the nucleation/cavitation phenomenon.

Regarding the over-pressurized superfluid helium, due to the mentioned experimental difficulties, we are not able to draw clear conclusions about the nucleation limit of superfluid helium.

Then in the metastable superfluid helium of negative pressure, we observed the cavitation bubble as expected, so we further studied its cavitation density. Using an interferometric set up, we have measured the cavitation density of liquid ^{4}He at $T = 0.96$ K and the result is $\rho_{cav} = 0.1338 \pm 0.0002$ g/cm^3. This means

[4] Although we use the AFG generator voltage, it is strictly proportional to the real driving voltage so that the extrapolation result will not be affected.

that superfluid helium around 1 K will break when its local density is lowered by 8.4%.

In order to compare it to other theoretical results, we converted this density to pressure by using an equation of state which was initially given by H. Maris then corrected by F. Caupin *et al.*. Meanwhile, different theoretical or simulation approaches gave a similar cavitation pressure at 0 K. And below 1 K, this cavitation pressure is nearly independent of temperature. So we used this well established EOS and obtained P_{cav} to be -5.1 ± 0.1 bar. However, F. Caupin *et al.* has proposed another experimental result. They used a far-fetched extrapolation method and found P_{cav} between -9.8 bar and -7.7 bar. Their method seems very logic, but is not compatible with our converted P_{cav}. Therefore, the method of F. Caupin *et al.*, our local density measurements and the EOS are not compatible together. For now, there maybe several possibilities for this paradox. First, in our experiments the quantum vortex density is much larger than the one in F. Caupin's experiment. Second, the equation of state is not correct. Third, the cavitation density maybe dependent of the static pressure, which makes the result of F. Caupin *et al.* would have to be reinterpreted. However, any of these statements requires much more study. Besides performing more cavitation density measurements, we have another way to study this problem which will be discussed in the general conclusion of this thesis. This study of metastable superfluid helium was partially published in [66].

Chapter V

Study of bubble lifetime in liquid helium

Introduction

We have already studied the acoustic cavitation limit of ^{4}He in last chapter. Acoustical cavitation will give birth to a vapor bubble, then this bubble will grow and collapse. Our grinded PZT and imaging system provide an excellent chance to study bubble properties by imaging the bubbles, such as measuring their

lifetime. And we found it very interesting that bubble lifetime has a dramatic transition as helium passes the $\lambda-$transition. By lifetime of the bubble, one means the time interval during which the bubble is created, grows, collapses and eventually disappears.

In superfluid helium, bubbles vanish quickly, their lifetime is on the order of one millisecond. On the contrary, in normal liquid helium, the lifetime is much longer and varies from ten to hundreds of milliseconds depending on temperature. Apparently, the large difference of bubble lifetime in the two different liquids is due to the $\lambda-$transition, but the dynamics is not that obvious.

As already discussed many times in this thesis, because of its extreme purity, liquid ^{4}He is a model liquid for the fluid dynamics. There are many studies about homogeneous cavitation bubble in superfluid helium [58, 41, 67]. All of them used a similar PZT to achieve acoustic cavitation, and they measured the scattering of an incident laser beam by the bubble using a fast photodiode. Surprisingly, none of them is dedicated to the bubble dynamics. The only one we are aware of is that of Roche *et al.* [67] who studied the bubble lifetime dependence on applied external pressure at very low temperature ($\sim$ 70 mK). Compared to their work, our set up allows a direct measurement of the diameter of bubbles.

This chapter is organized as follow: The first section is dedicated to experimental preparations. It is followed by the observation of bubbles in two different temperature ranges. At last we try to interpret and conclude on these results by analyzing the bubble dynamics.

V.1 Experimental preparation

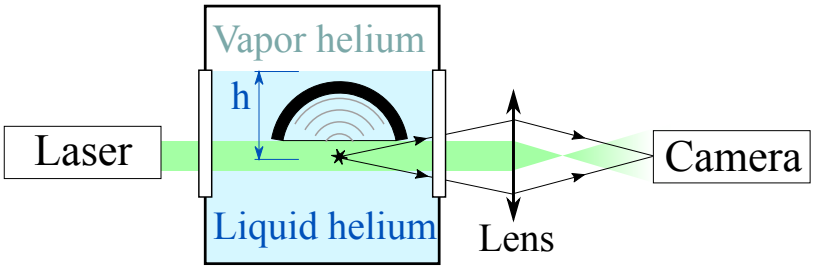

Fig.V.1 – Experimental set-up. PZT is immersed in liquid helium. The height of liquid above the sound focus is marked by h. The CCD camera focuses on the focus plane through a lens.

The detail experimental conditions have already been presented in Sect.II.4.3.2. However, our experimental cell is not originally designed for studying bubble lifetime. We had to make some changes to adapt to the new experimental environment.

V.1.1 Experimental set-up

A scheme of the set-up is shown in Fig.V.1. We still use a Nd:YAG pulsed laser as a light source. A parallel laser beam directly goes into the cell, and is scattered by bubbles created by the PZT. A lens system images the acoustic focus plane onto a CCD camera. The interferometer and phase plates have been removed, as the density measurement is no longer needed in this study.

V.1.2 Modified filling process

The standard filling process was already presented in Chapter.II. But it is not suitable for the measurement of bubble lifetime. As shown in Sect.II.1.1, the experimental cell is connected to the injection capillary. Because the lifetime of bubble is very sensitive to the exterior pressure[1], if the cell is over-filled, a small quantity of helium will stay in this slim capillary, and significantly rise the hydrostatic pressure inside the cell, which makes the pressure inside the cell very difficult to control. So we decided to keep the cell half filled so that the pressure around the bubble is the saturated vapor pressure plus the hydrostatic pressure. In this way, the bubbles will stay longer and are more easily detected.

Our actual PZT support is made for interferometry, and it hangs the transducer on the upper part of the cell. As shown in Sect.II.1.1, the cell window is too small to observe the upper half of the cell. As shown in Fig.V.1 we need to immerse the PZT entirely below the vapor-liquid interface, which is out of vision and difficult to determine. In order to overcome this problem, we chose to modify the filling process. Using the micro fluid flow controller and the Keller pressure transmitter which are outside the cryostat, we can fill the experimental cell at a constant pressure. Because the temperature in the cell is regulated by the thermal controller, all the injected helium vapor will turn to liquid at a constant temperature, so the vapor pressure can be considered as constant too. Therefore the filling process is stationary, and the condensation rate of the injected helium vapor is then constant. It is possible to calculate this rate by measuring vapor-liquid interface when it is in our field of vision.

Fig.V.2 shows two pictures taken during the filling process, the vapor-liquid interface is clearly seen. The structure of the cell is already known[2], if we consider the cell as a hollow cylinder, and neglect the volume of the PZT and its support, then by measuring the liquid height as a function of time, we can calculate at which time the PZT is totally immersed in liquid. In fact, this estimation has an important uncertainty. A typical value is $h = 10 \pm 10$ mm.

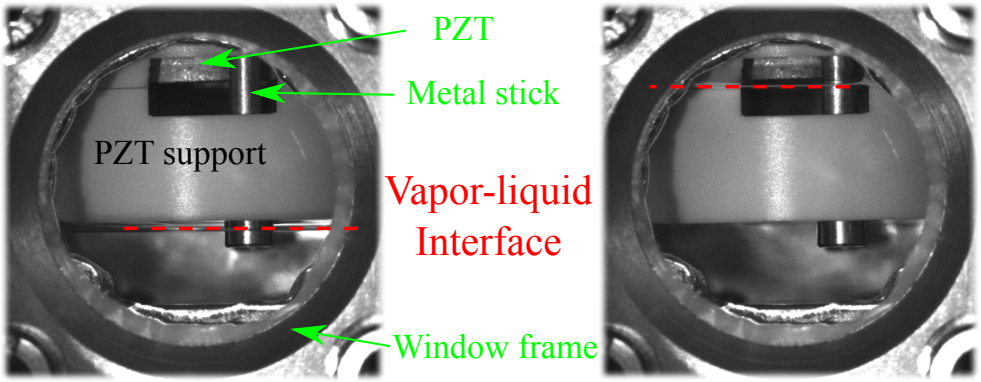

Fig.V.2 – Pictures of the experimental cell being filled with liquid helium. As marked in the left one, the support of the PZT occupies most of the visible zone through the circular window. The ceramic PZT is hung on the upper part of the PZT. Vapor-liquid interface is indicated by the dotted red lines.

V.1.3 The timing problem

In Sect.II.4.4, we presented the experimental protocol including the timing of the optical system. In the following paragraphs, I will use the same notations to denote the time line. Before applying it to the measurement of the bubble lifetime, we have to modify the synchronization process. The problem comes from measuring the time t_d. Eq.(II.11) gives the expression of t_d.

$$t_d = t_{pulse} - \Delta t_{flight} - t_{AFG}$$

It involves three different times: the RF signal burst departure time t_{AFG}, the laser pulse time t_{pulse}, and the time of flight of the sound wave Δt_{flight}. The generator of the RF signal—AFG is triggered by the initial TTL signal, so that t_{AFG} can't be negative. t_{pulse} and Δt_{flight} are two constant values. Eq.(II.11) restricts t_d not to exceed $t_{pulse} - \Delta t_{flight}$:

$$t_d \leq t_{pulse} - \Delta t_{flight}$$

We know that $t_{pulse} = 170$ μs and $\Delta t_{flight} \sim 26$ μs, so $t_d \leq 144$ μs. Therefore, the protocol does not allow to observe any bubble who lasts longer than 144 μs. However the observed bubble lifetime is largely distributed from one to hundreds of milliseconds, which requires that t_d should also be widely tunable. Here is the timing problem.

In order to solve this problem, we decided to make a time shift on the time line. It is considered that the time-resolved measurement has a default repetition

[1]The reason for this will be explained later in Sect.V.4.2.
[2]see Sect.II.1.1

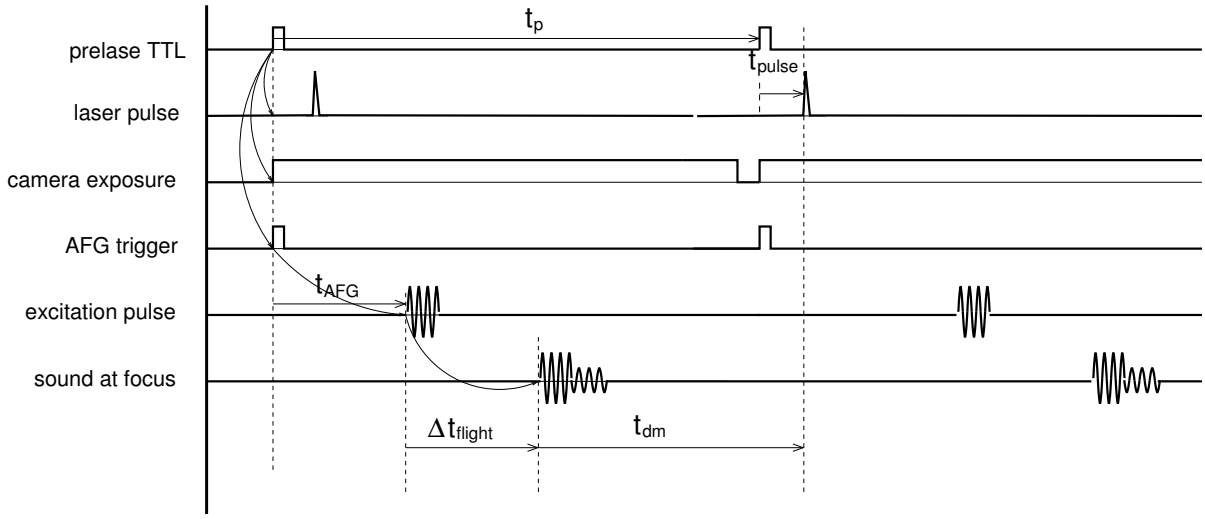

Fig.V.3 – The diagram of the modified time line, which is based on Fig.II.17. We shift all the measurements by the period time T, so as to observe the bubbles who last longer than 170 μs.

rate of 10 Hz. This frequency is adjustable through the AFG. Let the periodic time of the repetition to be t_p. We can shift every observation to the next measurement. Fig.V.3 shows a diagram of this modified time line. We can also express this modification by adding t_p to both sides of Eq.(II.11) and it becomes:

$$t_{dm} = t_{pulse} + t_p - \Delta t_{flight} - t_{AFG}$$

where t_{dm} stands for modified t_d. This new expression requires that $t_{dm} \leq t_{pulse} + t_p$, which depends on the adjustable value of t_p. Because t_{AFG} is widely tunable by the AFG, so is t_{dm}. If we want to observe a bubble which lasts 150 ms, we can simply set $t_p = 200$ ms and $t_{AFG} = 50$ ms[3].

V.2 Behavior of bubbles in superfluid helium

At first glance, the behavior of bubbles is not simple, we observed that the diameter and the lifetime of bubbles are both statistical quantities, as their values are distributed in some interval. In this section, I will respectively present our observations about bubble diameter and its lifetime. Then, we use statistical tool to measure the typical bubble lifetime in superfluid helium.

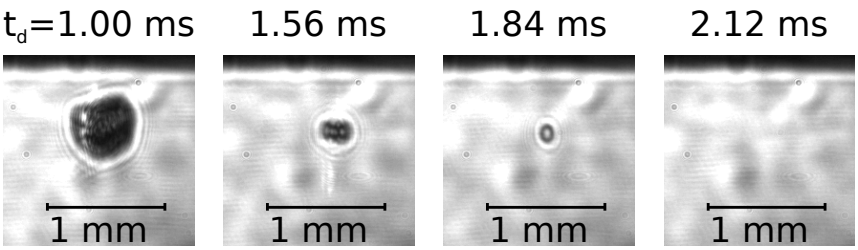

Fig.V.4 – Determining the lifetime of cavitation bubbles: data for $T_0 = 0.87$ K. Images of typical bubbles at different times t_d (see text). The upper black stripe is the shadow of the PZT.

V.2.1 Distribution of bubble's diameter

Fig.V.4 is a typical set of images of collapsing bubbles at $T_0 = 0.87$ K ($< T_\lambda$) recorded at different times t_d. Note that, these 4 images are of 4 different bubbles: the repetition rate of the camera does not allow to record continuously the evolution of a single bubble. In fact, for each setting of t_d we take many images of bubbles so as to do a statistical analysis. The images here are the typical bubbles for each time setting. Here, as mentioned in last section, $t_d = 0$ is the time at which the sound wave arrives at the PZT focus (the duration of the sound burst is one percent of the total bubble lifetime, therefore we consider the arrival of the sound wave as an instantaneous event). We can see that the center of the bubble stays at the same position, whereas its radius is decreasing with time: the bubble is collapsing where it was created. This point is important because it enables us to perform statistics on the lifetime of a bubble. In addition, the motion of bubble is another topic which will be described in the section of buoyancy effect.

Another noteworthy point is that the first left side image in Fig.V.4 is a bubble at its maximum radius. Its is obviously not a perfect sphere. We can attribute its cause to the so-called Rayleigh-Taylor instability [68, 69]. This phenomenon is a fingering instability of an interface between two fluids of different densities, which occurs when the light fluid is pushing the heavy fluid. In a review paper about this instability by D.H. Sharp [70], the author mentioned the complexity of the instability analysis in curved geometries, and it "depends strongly on compressibility and the acceleration history of the interface." Because the expansion of bubble is a fast dynamic process, the irregular spherical form of bubble is probably due to the Rayleigh-Taylor instability. There is a quantitative estimation about the surface acceleration in Sect.V.3.1.

We found that the diameter of bubbles is randomly distributed around a mean value. We supposed it could be caused by the fluctuations of the boundary conditions when the bubbles are created. For example, the fluctuation of the local density in superfluid helium, or the signal fluctuation of the electric devices, such

[3] t_{pulse} is too small compared to 50 ms and is neglected.

as the amplifier and the AFG. Although the exact source of fluctuation is unlikely to be found, those fluctuations obey a Gaussian distribution, which is to say the observables such as bubble diameter have a statistical behavior. To quantify these fluctuations, we measured 200 bubbles in the same conditions, and drew the histograms in Fig.V.5. All the data are taken at the same AFG voltage,

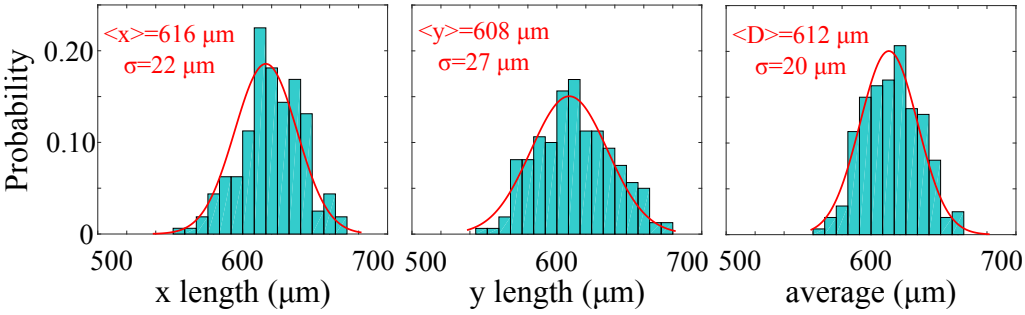

Fig.V.5 – Histograms of 200 bubbles in the same conditions. The three curves are respectively horizontal length, vertical length, and average diameter of bubbles. The mean values and standard deviations written in red are corresponding Gaussian parameters.

static pressure and temperature, and time delay. Because bubbles are irregular spheres, our way of measuring bubbles' diameter is to measure respectively their horizontal and vertical length, then we calculate their mean value.

Fig.V.5 shows that the distribution of bubbles' diameter is roughly Gaussian with a relative standard deviation of about 3%. So it is reasonable to state that the maximum bubble diameter also obeys a Gaussian distribution.

V.2.2 Measuring bubble lifetime

The lifetime τ of a cavitation bubble is expected to depend on several independent parameters. In a simplified model, we only consider the collapsing process of a vacuum bubble, and neglect the liquid-surface tension and viscosity. Then the equation of motion is determined by the time t, the liquid density ρ, the hydrostatic pressure P as Rayleigh shown as early as 1917 [71]. In fact, we can obtain a similar relation from a dimensional analysis. If we only consider the collapsing process, then the corresponding collapsing time $\tau_{collapse}$ depends on three independent parameters: P, ρ, and the initial radius R_0. We can write: $\tau_{collapse} = C\ P^x \rho^y R_0^z$, where x, y, z are three exponents to be determined, C is a constant. By using dimensional homogeneity, we obtain three equations about x, y, z, and have: $\tau_{collapse} = C\ \sqrt{\rho/P}\ R_0$ In the calculation of Rayleigh, he got:

$$\tau_{collapse} = 0.91468 \sqrt{\frac{\rho}{P}}\ R_0 \tag{V.1}$$

In our experiments, the cavitation trigger—the sound burst—only lasts a few microseconds, which is only 1% compared to the observed total bubble lifetime. So the bubble growth can be regarded as a free expansion in liquid, which is the reverse process of the bubble collapse. We can thus write the total lifetime τ as:

$$\tau \approx 2\ \tau_{collapse}$$

Therefore, the bubble lifetime is proportional to the maximum radius R_0 the bubble can reach. As described in the last section, the maximum radius obeys a Gaussian distribution, so $\tau(R_0)$ is also Gaussian distributed. We denote $p(t)$ as the probability of having a bubble at time t, and the probability density of τ is Gaussian distributed, then $p(t)$ should be:

$$p(t) = \frac{1}{2}\Big[1 - \mathrm{erf}(\frac{t - \langle\tau\rangle}{\xi})\Big] \tag{V.2}$$

where erf is the error function, $\langle\tau\rangle$ the mean lifetime of the bubble and ξ its standard deviation.

Experimentally, before determining the bubble lifetime, there are two problems to be solved. The first one is how to count the bubbles. The other is how to determine the threshold driving voltage of the PZT in order to compare the result amongst different temperatures.

V.2.2.1 Counting the bubbles

In order to measure the probability $p(t)$, it is inevitable to count the bubbles amongst thousands of images, which is far beyond my capability. And I decide to count it by computer program. But this is not easy neither. Fig.V.4 has shown a very clear image of small bubble(t_d = 1.84 ms), which is at the end of its collapse. However this image is only an outstanding example. In most cases, we will see a much less clear image like in Fig.V.6. The bubble intensity is almost the same order as the background noise. In fact, the signal-to-noise ratio is terribly low in this image, I have to process the image to accurately count the bubble in such condition. And I learned that the convolution of the image with a proper function will greatly increase the signal-to-noise ratio. In fact, this kind of imaging processing is called spatial filtering. More details can be found in any books of numerical signal treatments. My imaging processing is as follow: I firstly measured the background by taking an image without any bubbles and sound waves. Then, I subtracted the background signal from the bubble image, and got Fig.V.7. Here, the signal-to-noise ratio is roughly 4.

At last, after some trials, I chose a Laplacian of Gaussian as a spatial filter, with a width of 20 pixels. And the result of the convolution is shown in Fig.V.8. After processing, the signal-to-noise ratio is increased to 400, which is two orders of magnitude higher than the original value. By setting a simple

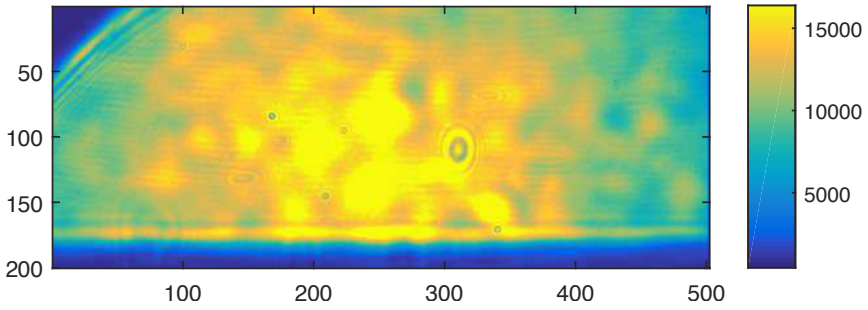

Fig.V.6 – Raw image captured by the CCD camera, the color bar at right side indicates the light intensity. x, y-axis represent the pixel coordinate of the camera. We can roughly find a small bubble around the pixel (300, 100).

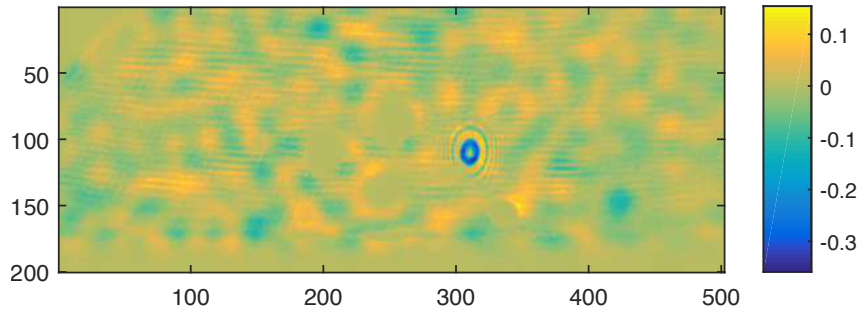

Fig.V.7 – Pretreated image, after subtracting the background noise from the raw image, the bubble signal becomes more evident. The color bar at right side is regularized by taking the maximum intensity of the raw image as unit.

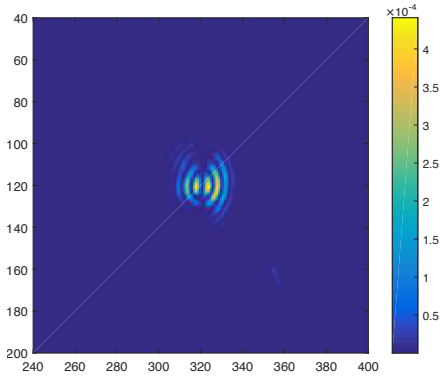

Fig.V.8 – The convolution of the pretreated image and the spatial filter. It shows a significant signal of bubble.

threshold value, and counting the number of pixels above this value, the bubble can be accurately counted. I have checked its accuracy manually—by manually

counting 1000 images—and have confirmed this method to be very efficient. In this way, counting bubbles amongst thousands of images becomes possible.

V.2.2.2 Driving voltage of the PZT

Another problem to be solved is to determine the threshold of the PZT driving voltage. As we already mentioned in the last chapter, the cavitation phenomenon is also distributed around a threshold driving voltage of the PZT. We can't measure the bubble lifetime if there is no bubble. So in the measurement of bubble lifetime, there must be a precondition, which is to measure bubble lifetime at the PZT driving voltage corresponding to the cavitation probability 1. If we denote the driving voltage corresponding to the cavitation probability= 0.5 by $V(Proba = 0.5)$. Then the threshold voltage $V_{threshold}$ should be: $V_{threshold} > V(Proba = 0.5)$. However, $V(Proba = 0.5)$ is a function of temperature. In order to have a consistent precondition of the threshold voltage in different temperatures, we finally chose this threshold to be the minimum driving voltage corresponding to the cavitation probability 1, which is:

$$V_{threshold} = 1.02\ V(Proba = 0.5)$$

This value is given by the "asymmetric S-curve formula"(see Sect.IV.2.2). Because the width of the curve is about 2% of its mid value, the minimum driving voltage is: $V(Proba = 1)_{min} \approx 102\% V(Proba = 0.5)$.

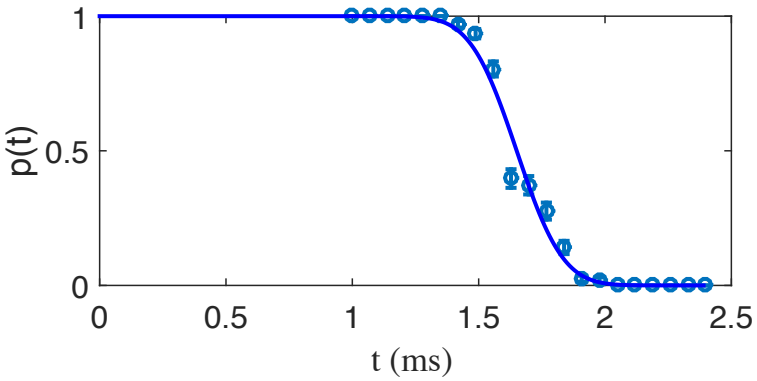

Fig.V.9 – Determining the lifetime of cavitation bubbles: data for $T_0 = 0.87$ K. Probability of existence of a bubble at time t. The solid line is a fit assuming that the lifetime of the bubble is gaussian distributed. The mean value $\langle\tau\rangle = 1.65$ ms, the half height length $\xi = 0.10$ ms.

Figure V.9 is one measured probability curve of $p(t)$. Every data point in the figure is composed of 200 images taken at the same conditions. The blue fit line is given by Eq.(V.2). It shows that such a fit reproduces the data pretty well and enables us to determine the bubble mean lifetime. We obtain, at this

temperature $T_0 = 0.87$ K, $\langle \tau(T_0) \rangle = 1.65$ ms, with a relative standard deviation of 6%. We notice that, this uncertainty is on the same order as the one on R_0, which is 3% and is given in Sect.V.2.1. We could say that the fluctuations have the same influences on both the bubble's diameter and lifetime, which is consistent with the proportional relation between R_0 and τ (see Eq.(V.1)).

Then we have performed these experiments at several temperatures below the λ-point. The results are shown on the left part of Figure V.10. In this temperature range, the lifetime of bubbles is roughly independent of T_0 and its value is 1.5 ± 0.2 ms. This is the statistical uncertainty which comes from the average of all data.

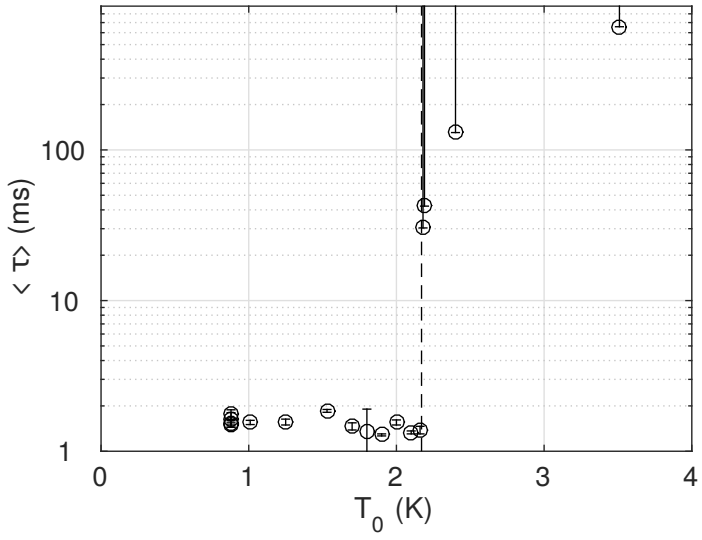

Fig.V.10 – Lifetime of bubbles in liquid helium as a function of temperature. The vertical dashed line marks the superfluid transition temperature ($T_\lambda = 2.17$ K). Above T_λ, we can only estimate the lower bound of the lifetime.

V.3 Behavior of bubbles in normal liquid helium

The bubble lifetime at $T_0 > T_\lambda$ is much longer (up to 600 ms). In this temperature regime, because of the long lifetime of bubbles, which is already on the order of 100 ms, we are obligated to lower the repetition rate of the measurement. If not, some bubbles will survive till the next sound burst arrives and re-expand. At last, bubbles will fill the vision, such as the photo shown in Fig.V.11. This should be avoided.

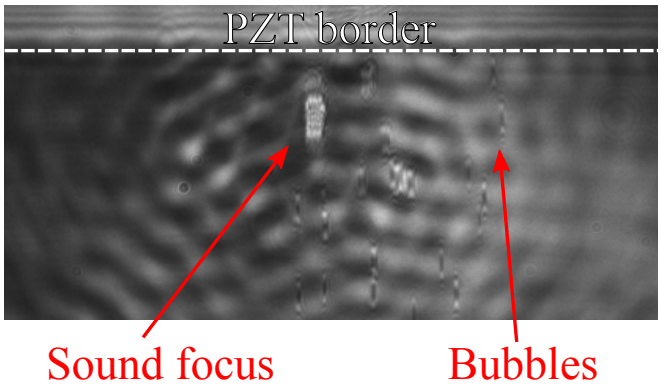

Fig.V.11 – Cavitation bubbles at $T_0 = 2.19$ K. The big bubble is acoustically created at the PZT focus. Other small bubbles are the survivors from previous sound bursts. This photo was taken at a much higher PZT driving voltage. The variation of refractive index is so high that sound wave deflects much light out of sight, and so makes fringes visible.

Fig.V.12 shows images of bubbles taken at different time. Although bubbles are always born at the focus of the acoustic wave, we have seen that, at later times, they become randomly distributed over the field of view. At a given time, there is a chance for a bubble to escape the imaged region and become undetected. Then we can't count the probability $p(t)$ in this regime. The only statement we can make is that the lifetime of bubbles in these experiments is bounded by a lower value corresponding to the highest value of t where $p(t) \neq 0$.

V.3.1 Bubble radius and the surface acceleration

Another observed phenomenon is that during the long lifetime, the radius of the bubble is quite stable. In Sect.V.2.1, I have mentioned the Rayleigh-Taylor instability, because in the superfluid regime, we observed that the bubble's radius changes very fast, and the surface acceleration is not negligible in its expansion, so the instability occurs while the fluid is accelerating. Whereas in the normal fluid, the observed bubble's radius does not change much, which is already shown in the figure above. The acceleration is thus much smaller. Here we can quantitatively estimate this acceleration. We only consider the simplest case, in which we assume the surface expansion is a uniform accelerated process. By using the corresponding equation of motion: $R = at^2/2$, where R, a, t are respectively the bubble radius, estimated acceleration and time. The following table gives a quantitative comparison about this estimated surface acceleration.

	Radius(μm)	Lifetime(ms)	Acceleration($\mathrm{m \cdot s^{-2}}$)
Superfluid	300	1.5	270
Normal	100	40	0.125

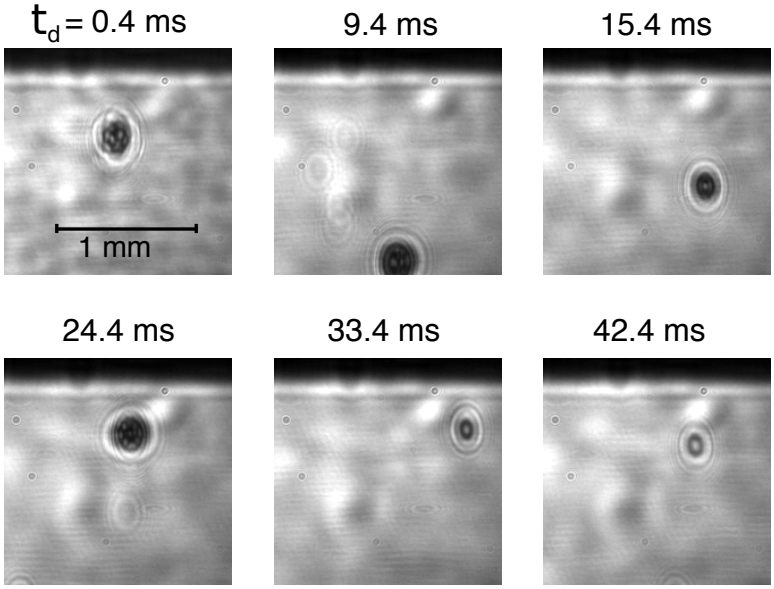

Fig.V.12 – Cavitation bubbles at $T_0 = 2.19$ K. The maximum diameter is about 200 μm. At first five milliseconds, bubbles are at the PZT focus. Later, bubbles become randomly distributed in the vision.

The surface acceleration of the normal liquid helium bubble is three magnitudes lower than the one of the superfuild helium bubble. So the Rayleigh-Taylor instability has much less influence on the surface profile of the normal liquid helium bubble, and they are more spherical.

All these aspects clearly indicate that the cavitation regime in the $T_0 > T_\lambda$ range is strongly different from the one in the superfluid case. This difference is especially remarkable when looking at the bubble lifetime as shown in Fig.V.10.

V.4 Dynamics analysis

In this section, we will try to explain what we have observed about bubble lifetime in two different regimes, and especially to understand the evolution of bubble during its lifetime. First, let us consider the influence introduced by acoustic wave. From our observed result, the lifetime of bubbles is longer than 1 ms. As a comparison, our acoustic burst time is less than 10 μs, which is only less than 1% of total bubble lifetime. So, although acoustic pressure gives birth to bubble, compared to its long time evolution, acoustic wave effect could be neglected in the later evolution of bubble.

Then, after the acoustic wave passed away, bubbles will grow and collapse in a stable environment, where two classical processes become dominating. One is the growth and collapse of bubble in its inertial reference as described by the

so-called Rayleigh-Plesset equation, and another is the motion of bubble in the laboratory reference. We can reasonably suppose the later one is mainly caused by buoyancy.

V.4.1 Buoyancy effect and turbulence effect

Buoyancy is an upward force exerted by a fluid that opposes the weight of an immersed object. In our case, the buoyancy effect is the main cause of bubble motion. Here we try to estimate bubble displacement due to buoyancy during its lifetime. From Archimedes' principle we can write this upward force by:

$$\mathbf{F}_{up} = -\rho_l V \mathbf{g}$$

where ρ_l is the liquid helium density, V is bubble volume, g is gravity acceleration. If we neglect viscosity in helium, as it is quite small in low temperature, bubbles will be accelerated. In fluid mechanics an accelerating body must remove some volume of surrounding fluid as it moves through it. This effect gives an additional inertia to the bubble which is generally called added mass. If we assume bubbles are perfect spheres, this added mass is

$$m_{added} = \frac{2}{3}\pi R^3 \rho_l = \frac{1}{2}\rho_l V$$

where R is bubble radius. So the bubble's equation of motion is:

$$\mathbf{F}_{up} + m_b \mathbf{g} = (m_b + m_{added})\mathbf{a}$$

where m_b is bubble vapor mass. As bubble vapor density in our temperature range is negligible compared to liquid helium density, we obtain $\mathbf{a} = -2\mathbf{g}$. Then, the maximum bubble displacement due to buoyancy is:

$$h = |\mathbf{g}|\tau^2$$

We apply this result to our observed result. In the superfluid case, bubble lifetime is about 1.5 ms. During this time, the maximum displacement of the bubble due to buoyancy is $g\tau^2 = 20$ μm, which is very small compared to the size of visible zone ($\sim$ 1 mm). In fact, this maximum displacement is equivalent to only 2 pixels on our CCD camera whereas the entire vision length is at least 500 pixels. It means the displacement of bubble is quite negligible during this short lifetime. So this is the reason why we observed the bubble is collapsing where it was created.

On the other case, in normal liquid helium, the observed bubble lifetime is at least on order of 20 ms. The vertical displacement due to the buoyancy effect is at least 4 mm. So during bubble lifetime, bubble will probably move outside of vision. But in fact, we can still see the bubble after 20 ms. I think this is

because of the turbulence induced by the displacement of bubbles in the liquid. By simply calculating the Reynolds number in this case, we can have a qualitative comprehension about this phenomenon. The Reynolds number Re is defined as:

$$\mathrm{Re} = \frac{\rho v D}{\mu}$$

where v is the maximum velocity of the bubble, D is the diameter of the bubble, ρ and μ are the density and viscosity of the liquid. Their corresponding values are about $g\tau \approx 0.1$ m/s, $D \approx 0.2$ mm, $\rho = 146$ kg/m^3, and $\mu \approx 10^{-6}$ kg/m/s[4]. And we have the Re for the moving bubble in normal liquid helium:

$$\mathrm{Re} \approx 2900$$

This Re value means the turbulence is inevitable. More precisely, in fluid mechanics, this Re value implies that the bubble will undergo the vortex shedding flow [72]. In this flow, vortices are created at the back[5] of the bubble and detach periodically from either side of the body. The fluid flow past the bubble will create alternating low-pressure vortices on the downstream side of the bubble. Then the bubble will tend to move toward the low-pressure zone. It is to say the rising bubble will be perturbed by the vortices, so as to swing on the horizontal direction. If the bubble touches the PZT wall, it will probably bounce away, and then reappear in the vision. This conclusion is consistent with our observation. Therefore, we can no longer measure the bubble lifetime, since we would never know when the bubble totally disappears.

V.4.2 Rayleigh-Plesset equation

Another process that governs bubble's evolution is the growth and collapse of bubble in its inertial reference. If we assume the bubble is a sphere, then its expansion and collapse are both radial. We can derive the equation of motion of the bubble surface from the Navier-Stokes equation.

In the ideal case, we consider the incompressible Navier-Stokes equations.

$$\rho\Big(\frac{\partial \mathbf{u}}{\partial t} + \mathbf{u}\cdot\nabla\mathbf{u}\Big) = -\nabla P + \mu\nabla^2\mathbf{u} \tag{V.3}$$

where $\mathbf{u}$ is the fluid velocity, ρ the density, P the pressure in liquid, μ the shear viscosity of the liquid. We notice that in the bubble's inertial reference, the fluid velocity is purely radial that $\mathbf{u} = u(r)$, then the velocity can be represented by a potential, with $u = \nabla\phi$. Eq.(V.3) becomes:

$$\rho\Big[\frac{\partial \phi}{\partial t} + \frac{1}{2}\Big(\frac{\partial \phi}{\partial r}\Big)^2\Big] = -P \tag{V.4}$$

[4]The value of the viscosity will increase one magnitude as the temperature goes from 2.17 K to 4 K. This given value is an mean estimation.

[5]Back is the direction opposite from the one bubble is traveling.

where r is the radial distance to the bubble center. Let $U = u(r = R)$ be the thin layer velocity at the bubble surface, where R is the radius of the bubble, it is a function of time. Near the bubble, the incompressible liquid flow obeys the conservation of mass:

$$u(r) = \frac{R^2}{r^2}U = \frac{R^2}{r^2}\frac{\partial R}{\partial t}$$

which leads to:

$$\phi = -\frac{R^2}{r}\frac{\partial R}{\partial t} + C(t) \tag{V.5}$$

where $C(t)$ is a free constant, which is determined by the pressure boundary condition at infinity of Eq.(V.5). Now we consider the pressure term of Eq.(V.4). The contribution of pressure comes from four terms: the liquid pressure outside the bubble P_0, the vapor pressure in the bubble p_v, the pressure due to the shear viscosity and the pressure due to the surface tension:

$$P = p_v - P_0 - \frac{4\mu}{R}\frac{\partial R}{\partial t} - \frac{2\sigma}{R} \tag{V.6}$$

The equation of motion of the bubble surface is given by Eq.(V.4), Eq.(V.5), and Eq.(V.6), where r is replaced by R. And it is noticed that p_v is the saturated vapor pressure, and only depends on the temperature T inside the bubble gas. Then we have:

$$R\frac{\partial^2 R}{\partial t^2} + \frac{3}{2}\Big(\frac{\partial R}{\partial t}\Big)^2 = \frac{1}{\rho}\Big[p_v(T) - P_0 - \frac{2\sigma}{R} - \frac{4\mu}{R}\frac{\partial R}{\partial t}\Big] \tag{V.7}$$

This is the Rayleigh-Plesset equation. It is widely applied in many domains, such as bubble collapse and sonoluminescence [73, 74, 75]. Solving the equation requires knowing P_0 and p_v. The former one could be regarded as the hydrostatic pressure. The later one depends on the heat transfer across the bubble surface [76]. We can consider the following scenarios: while the bubble is expanding, a small quantity of liquid helium near the bubble wall will evaporate. Since the vaporization lowers the liquid temperature, the faster the bubble expansion is, the more heat it consumes. On the contrary, instead of lowering the temperature, the collapse will lead to the condensation of the vapor, which rises the temperature, and the heat has to be dissipated.

V.4.3 Superfluid helium bubble

The bubble lifetime in superfluid helium is quite short, and its motion in the laboratory reference could be neglected. So, the bubble behavior should be mainly described by the Rayleigh-Plesset equation. As mentioned once, to solve this equation is to find P_0 and p_v. In the superfluid state, the thermal conductivity is extremely large. We will show in the following paragraph that the temperature T in the gas is always the static temperature T_0 of the liquid far away from the

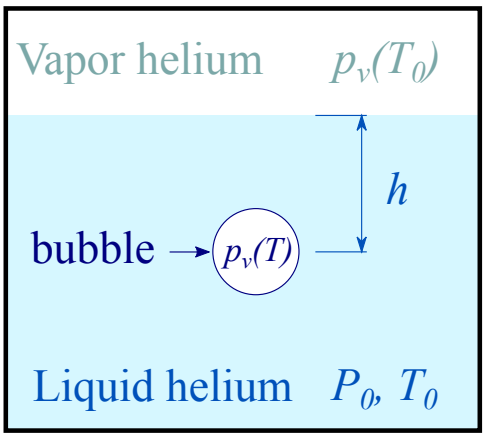

Fig.V.13 – A diagram of the temperatures and pressures in liquid and in bubble.

bubble, and the Rayleigh-Plesset equation becomes a purely mechanical equation.

The scenario is presented in Fig.V.13. Let the spherical bubble be at its maximum radius $R_0 = 300$ μm, and filled with helium vapor at T_0. The number of moles in the bubble n_v is given by the equation of state for ideal gas:

$$n_v = \frac{4\pi R_0^3}{3R_g T}\, p_v(T_0)$$

where $R_g = 8.31$ J/mol/K is the gas constant. The molar latent heat of vaporization of helium is on the order of $L_v(1.9\text{ K}) = 93.2$ J/mol and varies by less than 16% between 0.9 K and 4 K [29]). Therefore, the total heat to be transfered Q_v will be:

$$Q_v = n_v L_v$$

The next step is to estimate the increase of temperature in the surrounding liquid induced by the condensation. In superfluid helium, heat is transfered by second sound [3, 77], whose velocity is about $v_2 \simeq 20$ m/s between 0.9 K to T_λ [29]. We can consider the heat transfer as a radial transport process, with a typical radius $r_{heat} = v_2\tau$, where τ is the bubble lifetime. And the temperature of the liquid within this radius can be regarded as uniform. So the increase of temperature is the total latent heat divided by the heat capacity of the surrounding liquid which equals to the molar number times the volume of the liquid:

$$\Delta T = \frac{Q_v}{n_2\ C(T_0)}, \text{ with } n_2 = \frac{4\pi\ r_{heat}^3}{3M_{\text{He}}}$$

where $C(T_0)$ the molar heat capacity of the liquid at T_0, and M_{He} the molar mass

of helium. n_2 is the number of mole inside the typical radius[6]. By substituting Q_v in the equation above, we get:

$$\Delta T = \frac{M_{\mathrm{He}} R_0^3}{R_g r_{heat}^3} \frac{p_v(T_0) L_v(T_0)}{C(T_0)} \tag{V.8}$$

Because the values of p_v, $L_v(T_0)$, and $C(T_0)$ are already given in [29], we can directly calculate the value of ΔT as a function of T_0. The result is shown in Fig.V.14. We find that for 0.9 K $< T_0 < T_\lambda$, ΔT is about 10 nK. This results

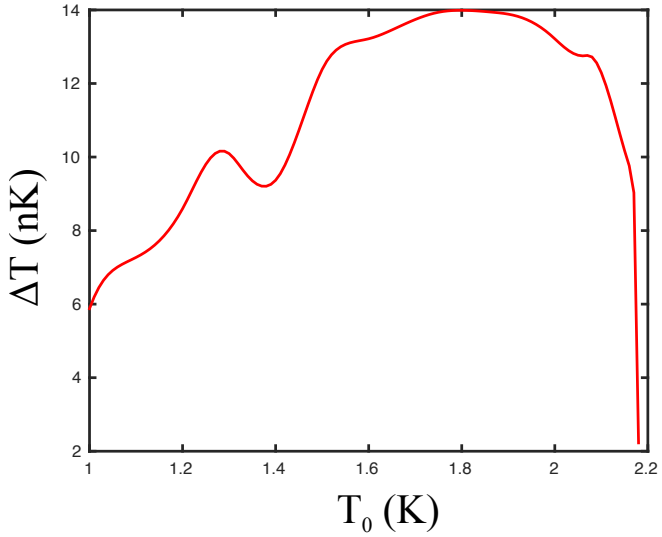

Fig.V.14 – The calculated ΔT as a function of T_0 using Eq.(V.8).

in a rise of the vapor pressure of about 10^{-4} Pa which is certainly negligible compared to $p_v(T_0)$, as the smallest value of p_v in this temperature is about 5.4 Pa. Therefore the condensation heat of the vapor does not influence the temperature in the bubble, and it always remains at the equilibrium temperature T_0.

According to the two-fluid model of superfluid helium, the superfluid fraction will turn to normal fraction if the heat flow is too big. So there remains one question: is the heat flow small enough to be sustained by the superfluid fraction converting to normal fraction at the bubble interface? Shimazaki *et al.* have measured the heat transfer by second second for fluxes as high as 5 W/cm^2 [78]. In our case, this flux is given by:

$$\phi_{heat} = \frac{Q_v}{4\pi R_0^2 \, \tau}$$

The maximum value of ϕ_{heat} is 0.2 W/cm^2, which is much smaller than the result of Shimazaki 5 W/cm^2.

[6]The bubble radius is extremely small compared to this typical radius, so the volume of the bubble is neglected.

Hence, the heat flow is moderate enough for superfluid fraction, and it is also fast enough to transfer the latent heat. As a result, we can safely state that in the superfluid case, the heat transfer is very fast, and the pressure in the bubble is always $p_v(T_0)$.

Another pressure term of the RP equation is the hydrostatic pressure in the liquid P_0. Since we have modified our filling process, the pressure in the experimental cell is always p_v. The expression P_0 is:

$$P_0 = p_v(T_0) + \rho g h$$

where ρ is the liquid density g the gravity acceleration, and h the height of liquid above the bubble (see Fig.V.13). By substituting P_0, Eq.(V.7) simply becomes:

$$R\frac{\partial^2 R}{\partial t^2} + \frac{3}{2}\Big(\frac{\partial R}{\partial t}\Big)^2 = \frac{1}{\rho}\Big(-\rho g h - \frac{2\sigma}{R} - \frac{4\mu}{R}\frac{\partial R}{\partial t}\Big) \tag{V.9}$$

of which the solution is called the Rayleigh solution.

This equation can be solved numerically. In fact, we used the *MATLAB* application to do so. Based on the *Runge-Kutta* method [79, 80], *MATLAB* provides a specific function called "ODE" to solve ordinary differential equations, Since Eq.(V.9) contains the first and second order derivatives of R, the ODE function requires to input a couple of the initial values $(R, \mathrm{d}R/\mathrm{d}t)$, which are the bubble radius and the velocity of bubble surface. However there is not any direct measures of the velocity, but it is clear that the velocity is zero when the bubble is at its maximum radius. So our first attempt of solving Eq.(V.9) was to only compute the collapsing evolution. And by assuming the growth and collapse are symmetric with respect to time, we can rebuild the evolution of R as a function of time. As a result we found that the hydrostatic term $-\rho g h$ on the right side of Eq.(V.9) is dominant in the total collapse time. This is reasonable if we compare the values of the terms on the right side: in the temperature range 0.9 K $< T < T_\lambda$, the hydrostatic pressure is on the order of 20 Pa, and $\sigma \sim 3.0\times10^{-4}$ N/m and $\mu \sim 1.3\times10^{-6}$ [29]. If we assume the maximum velocity of the bubble surface v_{surf} is the sound speed in helium, then the two later terms of Eq.(V.9) only become considerable when $R \sim 10$ μm and $v_{surf} \sim 200$ m/s. At this time, the bubble will close in 50 ns, compared to the total lifetime of 1.5 ms, it is the very end of the collapse.

But one question arises, as mentioned in Sect.V.1, our experimental cell does not allow to precisely measure the value h. Although we performed the modified filling process, the value h can only be estimated with a great uncertainty $h = 15 \pm 10$ mm. So we have to set h as a free parameter in order to fit our measured diameter. As shown in Fig.V.15, we plot the mean radius of the bubble as a function of time, which are determined by the bubble images, and compare it to the Rayleigh solution with the fitted $h = 14mm$. We can find the Rayleigh solution fits quite well with the measured radius, and this results clearly support our assumption which is given at the beginning of this section.

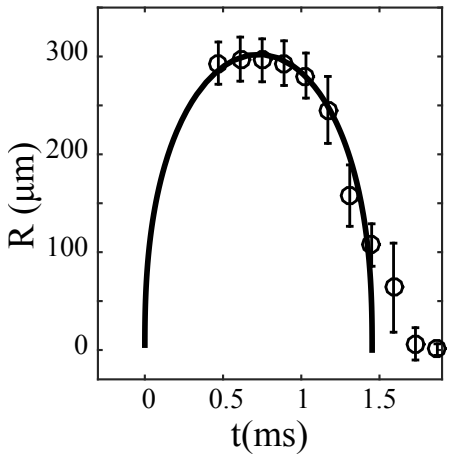

Fig.V.15 – Bubble radius as a function of time at $T_0 \sim 1$ K. Circles are the data obtained from the bubble images (see Sect.V.2.1). The black curve is the solution of Eq.(V.9).

V.4.3.1 The rebound bubble

However, at the end of the bubble lifetime, there are two abnormal data points which could not be fitted by the Rayleigh solution. We attribute them to rebound bubbles. The rebound bubble, as a classical fluid phenomenon, has already been observed many times in the study of the cavitation in different liquids [81, 67, 82, 83]. The collapse of the primary bubble gives birth to the rebound bubble. Our imaging method can't distinguish whether the observed bubble is primary or rebound.

In addition,there is no data for the early growth of the bubble, because those images were initially taken for measuring the bubble probability. At early stage of this study, we did not plan to plot the $R(t)$ curve. In order to increase the efficiency of measuring the probability, we chose to only measure the bubbles at the end of its lifetime, as all the measurements at early time have the same probability of 1. Nevertheless, we have performed another series of measurements to check the rebound bubble issue.

In order to overcome the limit of the camera imaging method, and to follow the full evolution of a single bubble and also to further validate our results, we have performed the same experiment with a fast photodiode, instead of using the camera.

Fig.V.16 is the experimental setup of such a measurement. We put the photodiode at the focus of the lens so as to capture the parallel laser light. Once the bubble is created, the laser beam will be partially scattered, and the recorded intensity is lowered as can be seen on Fig.V.17.

Assuming the scattered light intensity ΔI_{bubble} is proportional to the the

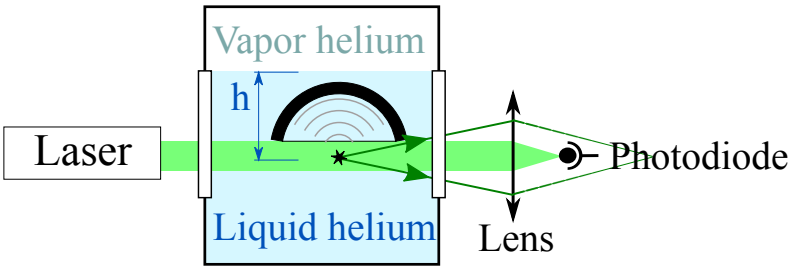

Fig.V.16 – Experimental set-up. The cavitation bubble induced by the focused acoustic wave produced by the piezoelectric transducer (PZT) is imaged by a lens onto a CCD camera.

square of bubble radius:

$$\Delta I_{bubble} \simeq C^{st}\ R(t)^2$$

where C^{st} is a constant to be determined, and by subtracting the signal with a bubble to the signal without a bubble, we can obtain ΔI_{bubble}. Since we have already measured the maximum radius of the bubble by the camera, it is not difficult to find C^{st}. In Fig.V.18, we see a bubble followed by a rebound bubble. This rebound bubble also obeys the Rayleigh-Plesset equation. The figure on the right side is a superposition of 30 measurements without an evident rebound. As expected, those 30 signals start at the same time, but end differently, each of them being well described by the Rayleigh-Plesset equation. This is consistent with the conclusion that the bubble lifetime is randomly distributed. We observed that not every primary bubble is followed by a rebound. The probability of such a rebound is about 70 %. According to the result in sonoluminescence [84], the rebound is inherent to the cavitation phenomenon. Perhaps in our case, some signals of the rebound are too small to be seen in the background noise.

V.4.3.2 Discussion

For now, we have almost explained the dynamics of the bubble in superfluid helium, but there are still two unsolved questions.

The first one is the divergent velocity in the Rayleigh solution. If we consider the velocity of the surface at the start and at the end of the lifetime, the velocity is divergent in both cases. In fact, despite the type of liquid, there is already some study about the divergent velocity during the collapse. Barber *et al.* have studied the ultrasonic collapse of the bubbles in water [84], and they state that because of the ultrasonic collapse, a part of the bubble energy is dissipated due to the shock wave of the collapse. This provides a good interpretation of why the rebound bubble is always smaller than the original one. But we are unaware of the divergent velocity at the start of the bubble lifetime. In the solution of the Rayleigh-Plesset equation for the superfluid bubble, instead of choosing the measured boundary conditions ($R = R_{max}, v_{surf} = 0$), we could manually

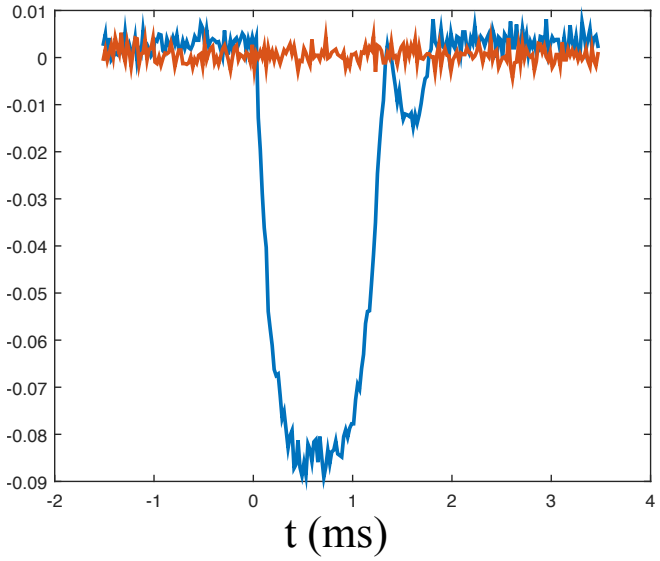

Fig.V.17 – Raw signals of the photodiode. The red line is the signal without a bubble, and the blue one is the signal with a bubble. The bubble scatters light so that it lowers the light intensity received by the photodiode.

find another couple of the boundary conditions, and get the same curve. If we assume the maximum value of v_{surf} is the sound speed at static pressure, then we found the possible initial bubble radius is $R_{init} = 5$ μm. This means after being triggered by the sound waves, the bubble has a initial radius of 5 μm and a initial surface velocity of 230 m/s. We know that the duration of the sound bursts is on the order of 1 μs, and the mean velocity of the surface at the start of the bubble lifetime is about 5 m/s.

Therefore we could consider the following scenario: once the local pressure exceeds the critical value of cavitation, the bubble will grow and the local sound speed. And this speed will tend to zero as the local pressure tends to critical pressure[7]. As the local pressure changes very quickly, the mean velocity of the bubble surface can be regarded as an average of the local sound speed on time. So it seems reasonable to assume that the bubble will grow at the sound speed. In fact, to calculate the very beginning of the bubble behavior is very difficult. Since this problem is highly related to the cavitation process, I tried to look for the answer in the literature of nucleation theory. However, this theory only provides a statistical description of the cavitation process, and we can't find any clue about our dynamics problem.

The second question is related to the bubble size. In our experiments with superfluid helium, we performed thousands of measurements in different conditions, but to our surprise, we have never successfully observed any primary

[7]The sound speed is strictly zero when pressure reaches the spinodal limit.

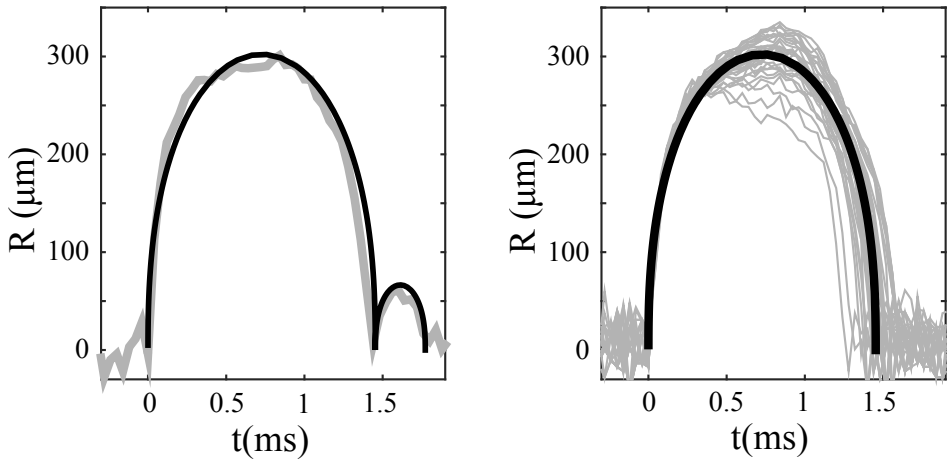

Fig.V.18 – Bubble radius as a function of time at $T_0 \sim 1$ K. On all figures, black solid line is the Rayleigh solution of the Rayleigh-Plesset equation (eq:V.9). Left: Gray curve is one typical photodiode measurement. After the bubble has collapsed, a second bubble is created. Right: Gray curves is the superposition of 100 measurements of the bubble evolution.

bubble which lasts less than 1 ms, which we can call a small bubble. The kinetic energy of bubble E_{bubble} is proportional to its volume [85]. Eq.(V.1) gives $\tau \propto R$ so that:

$$E_{bubble} \propto \tau^3$$

Then its energy spectrum should be continue, so why isn't it. In addition the rebound bubble is actually a small bubble, so why can't we create a small bubble by the cavitation? I still don't know.

At last, our conclusion is that for $T_0 < T_\lambda$, the cavitation dynamics is purely mechanical, a conclusion supported by the fact that the bubble lifetime is independent of temperature. Note that Roche and coworkers have reached a similar conclusion but for liquid helium at much lower temperature (70 mK) [67]. At such a low temperature, the vapor pressure of liquid helium is essentially zero so that bubbles can be considered as empty cavities in which of course no thermal effects can occur.

V.4.4 Normal liquid bubble

For $T_0 > T_\lambda$, the bubble lifetime is higher by at least 1 or 2 orders of magnitude larger than in the superfluid state.

In the normal state, heat is transported by thermal diffusion. A gradient of temperature appears so as to maintain the pressure inside the bubble equal, but for the Laplace term, to the external pressure. This dramatically slows down the collapse of the bubble. This problem has been addressed theoretically by Plesset

and Zwick for boiling water [86]. Using the approach of Plesset, Florschuetz and Chao have addressed the symmetric problem of collapsing vapor bubbles in an undercooled liquid [87]. To our knowledge, this work is the only one looking theoretically at heat transport in a non-acoustically driven collapse of a vapor bubble. Florschuetz and Chao make the assumption of a temperature gradient concentrated at the bubble interface. We solved their equations, slightly adjusted to our case of a depressurized rather than undercooled fluid and found lifetimes as high as 3000 s. In a review on cavitation [73], Plesset and Prosperetti have questioned the validity of the approximation used by Florschuetz and Chao. With the opposite approximation of a gradient extending to infinity, we find more reasonable times of $\sim$ 40s. Whether these calculated lifetimes strictly correspond to reality cannot be checked experimentally because of the buoyancy of the bubbles. Indeed, for such a long lifetime, the inertial velocity of the bubble will reach the stationary regime under the action of the gravity and the viscosity which is approximately:

$$v = \frac{2R_0^2 \rho g}{9\mu}$$

As a result, the expected change in height is given by $H = vt$ which is about 200 m for $t = 40$ s. It is unlikely to measure the bubble's behavior in any existing cryostat. However it is clear that heat transport is the mechanism that governs the dramatic transition in the bubble lifetime at T_λ.

V.5 Conclusion

We have experimentally studied the lifetime of bubbles produced by acoustic cavitation in liquid ^{4}He. We found that this lifetime undergoes a dramatic transition when the liquid crosses the normal to superfluid transition. In the superfluid state, the bubble lifetime is found to be consistent with the Rayleigh model in which heat effects are ignored. On the contrary, in the normal state of the liquid, one has to take into account the diffusion of the latent heat of condensation. The temperature-dependent Rayleigh-Plesset equation is likely to describe much better the real dynamics of the collapsing bubble.

Liquid helium offers a unique opportunity to study the transition from the Rayleigh regime to the Rayleigh-Plesset regime in analyzing and modeling collapsing vapor bubbles. The present experiment is a first step in such a study which is of interest for both the helium and the acoustic cavitation communities. This work was published in [88].

Conclusion and prospects

We have measured the exact appearance time of the instability in the metastable solid ^{4}He using the Schlieren method, and confirmed that it only appears during low pressure swing of the acoustic wave. This instability was never predicted by any theories. According to the dependence of the vacancy activation energy and the molar volume, we probably observed an instability in the low vacancy activation energy regime. This is a potential candidate for supersolidity. In order to further check the properties of this metastable solid helium, we intended to measure its local sound velocity by the stimulated Brillouin scattering (SBS), which is the next step of our long term research project.

In the metastable superfluid ^{4}He, we have investigated its cavitation density using the "time-resolved quantitative multiphase interferometric method", and found that at $T = 0.96\,\mathrm{K}$ $\rho_{cav} = 0.1338 \pm 0.0002\,\mathrm{g/cm^3}$, which is about 8.4% lower than its static density. We converted this result to pressure by the well-established equation of state of helium, and obtained the cavitation pressure P_{cav} to be -5.1 ± 0.1 bar. But this result is not compatible with the one measured by F. Caupin *et al.* [51]. Actually, we could not find a satisfying explanation for this problem. More data are needed, and one of these being the experimental study of the EOS for superfluid helium in the negative pressure domain.

Following the study of cavitation limit in superfluid helium, we further studied the evolution of bubbles in both superfluid and normal liquid helium. By introducing the Rayleigh-Plesset equation and considering the heat transport in two different cases, we successfully explained the dramatic transition of bubble lifetime when helium passes the λ-transition. However, we still found some unsolved questions about the short lifetime bubbles, and we are planning to perform some new measurements to check it.

The future: experimental determination of the EOS

As explained in this thesis, the EOS of metastable liquid/solid helium plays a crucial role in converting the density measurements to pressure values. Therefore, measuring this EOS experimentally is mandatory. Stimulated Brillouin

scattering (SBS) will be used for this purpose.

Here I will give a short introduction of this technique. It involves the interaction of photons and phonons in a medium. We consider a light beam propagating in a medium. At non-zero temperature, the medium contains many thermal phonons. A small part of photons will be reflected by these phonons. The reflected and incident light beams are counter-propagating and will form a stationary light wave inside the medium. Due to electrostriction, the electric field of the stationary light wave will cause a modulation of the medium density and hence of the refractive index. This index modulation acts as a Bragg reflector and increases the intensity of the reflected light. The amplitude of the stationary wave is then increased, and so is the index modulation, thus increasing again the reflected intensity... and so on. Above some threshold, the incident light is totally reflected. This is the so-called stimulated Brillouin scattering. It must be noted that the Bragg reflector created by this process is traveling at the speed of sound and due to the Doppler effect, the frequency of the reflected light will be slightly shifted with respect to the incident light. By measuring this shift, we could extract the local sound velocity. It is known that the sound velocity is an expression of local pressure and density:

$$c = \sqrt{\left(\frac{\partial P}{\partial \rho}\right)_S}$$

where P ρ S are respectively the local pressure density and entropy. As our interferometric method enables to measure the local density of the metastable helium, by combining with the direct measurement of local sound velocity, we can obtain the local pressure of the metastable helium. Then we can further check the equation of state for both solid and superfluid helium.

In order to realise the SBS in the cryostat, we are planning to focus an intense pulsed laser at the acoustic focus. Because the size of this acoustic focus is typically 100 μm, it is very difficult to precisely focalize the laser at the acoustic focus. It is noteworthy that the study of the bubble evolution gives a lot of information about bubble's position, size, and even its surface curvature. If we take the bubble as a reference while adjusting the focalization of laser, these informations will help to ease the adjusting process. This challenging experiment will be performed by the next PhD student of the group and hopefully open a new perspective to the fascinating properties of metastable liquid and solid helium.

Bibliography

[1] F. Souris, J. Grucker, J. Dupont-Roc, and P. Jacquier, "Time-resolved multiphase interferometric of a highly focused ultrasound pulse," EPL **95**, 66001 (2011). (document), I.2, II.4, III, III.3

[2] F. Souris, "L'hélium solide méstastable en sous-pression (french)," Ph.D. thesis, Université Pierre et Marie Curie, Paris, France (2013). (document), I.4, II.1.2, II.2.2, II.2.3, II.3.2, II.3.2, II.4.1, II.4.1, II.4.3.2, III

[3] J. Wilks, *The properties of liquid and solid helium* (Oxford University Press, 1967). I, I.3, V.4.3

[4] M. Chan, R. Hallock, and L. Reatto, "Overview on solid 4he and the issue of supersolidity," Journal of Low Temperature Physics **172**, 317–363 (2013). I.1, I.1.2

[5] J. De Boer, "Quantum theory of condensed permanent gases i the law of corresponding states," Physica **14**, 139–148 (1948). I.1

[6] C. A. Burns and E. D. Isaacs, "Debye-waller factor in solid ^{4} he crystals," Phys. Rev. B **55**, 5767–5771 (1997). I.1

[7] A. F. Andreev and I. M. Lifshitz, "Quantum theory of defects in crystals," Sov. Phys-JETP **29**, 1107–1113 (1969). I.1.1

[8] G. V. Chester, "Speculations on bose-einstein condensation and quantum crystals," Phys. Rev. A **2**, 256–258 (1970). I.1.1

[9] A. Andreev, K. Keshishev, L. Mezhov-Deglin, and A. Shal'Nikov, "Attempts at observing vacancions in he4 crystals," ZhETF Pisma Redaktsiiu **9**, 507 (1969). I.1.2

[10] H. Suzuki, "Plastic flow in solid helium," Journal of the Physical Society of Japan **35**, 1472–1479 (1973). I.1.2

[11] V. Tsymbalenko, "Plastic flow of crystalline he4," ZhETF Pisma Redaktsiiu **23**, 709 (1976). I.1.2

[12] D. Greywall, "Search for superfluidity in solid he 4," Physical Review B **16**, 1291 (1977). I.1.2

[13] D. Bishop, M. Paalanen, and J. Reppy, "Search for superfluidity in hcp he 4," Physical Review B **24**, 2844 (1981). I.1.2

[14] M. W. Meisel, "Supersolid 4 he: An overview of past searches and future possibilities," Physica B: Condensed Matter **178**, 121–128 (1992). I.1.2

[15] E. Kim and M. H. Chan, "Observation of superflow in solid helium," Science **305**, 1941–1944 (2004). I.1.2

[16] E. Kim and M. Chan, "Probable observation of a supersolid helium phase," Nature **427**, 225–227 (2004). I.1.2

[17] S. Balibar and F. Caupin, "Supersolidity and disorder," Journal of Physics: Condensed Matter **20**, 173201 (2008). I.1.2

[18] J. Day and J. Beamish, "Low-temperature shear modulus changes in solid 4he and connection to supersolidity," Nature **450**, 853–856 (2007). I.1.2

[19] O. Syshchenko, J. Day, and J. Beamish, "Frequency dependence and dissipation in the dynamics of solid helium," Physical Review Letters **104**, 195301 (2010). I.1.2

[20] J. Beamish, A. Fefferman, A. Haziot, X. Rojas, and S. Balibar, "Elastic effects in torsional oscillators containing solid helium," Physical Review B **85**, 180501 (2012). I.1.2

[21] H. J. Maris and S. Balibar, "Effect of helium elasticity on torsional oscillator measurements," Journal of Low Temperature Physics **162**, 12–22 (2011). I.1.2

[22] S. Balibar, A. Fefferman, A. Haziot, and X. Rojas, "Disorder, supersolidity, and quantum plasticity in solid helium 4," Journal of Low Temperature Physics **168**, 221–234 (2012). I.1.2

[23] D. Y. Kim and M. H. W. Chan, "Absence of supersolidity in solid helium in porous vycor glass," Phys. Rev. Lett. **109**, 155301 (2012). URL: http://link.aps.org/doi/10.1103/PhysRevLett.109.155301. I.1.2

[24] R. Simmons, "Thermal vacancies in quantum solid heliums," Journal of Physics and Chemistry of Solids **55**, 895–906 (1994). I.2, I.1.3

[25] Q. Mei and K. Lu, "Melting and superheating of crystalline solids: from bulk to nanocrystals," Progress in Materials Science **52**, 1175–1262 (2007). I.2

[26] H. J. Maris, "Properties of metastable solid helium below the normal melting pressure," J. Low Temp. Phys. **155**, 290 (2009). I.2, III

[27] F. London, *Superfluids* (Wiley, 1954). I.5

[28] L. Landau, "Theory of the superfluidity of helium ii," Physical Review **60**, 356 (1941). I.3.1

[29] R. J. Donnelly and C. F. Barenghi, "The observed properties of liquid helium at saturated vapor pressure," Journal of Physical and Chemical Reference Data **27**, 1217 (1998). I.3.1, V.4.3, V.4.3, V.4.3

[30] S. Balibar, "Nucleation in quantum liquids," J. of Low Temp. Phys. **52**, 363–421 (2002). I.4, I.4.1, IV

[31] S. Balibar and F. Caupin, "Nucleation of crystals from their liquid phase," C. R. Physique **7**, 988–999 (2006). I.4

[32] P. G. Debenedetti, "Supercooled and glassy water," Journal of Physics: Condensed Matter **15**, R1669 (2003). I.4.1

[33] L. D. Landau and E. Lifshitz, *Course of Theoretical Physics : Statistical physics, part I* (pergamon, Oxford, 1980). I.4.1

[34] D. W. Oxtoby, "Homogeneous nucleation: theory and experiment," Journal of Physics: Condensed Matter **4**, 7627 (1992). I.4.1

[35] D. Turnbull and J. C. Fisher, "Rate of nucleation in condensed systems," The Journal of chemical physics **17**, 71–73 (1949). I.4.1

[36] D. N. Sinha, J. Semura, and L. Brodie, "Homogeneous nucleation in he 4: A corresponding-states analysis," Physical Review A **26**, 1048 (1982). I.4.2

[37] H. J. Maris and Q. Xiong, "Nucleation of bubbles in liquid helium at negative pressure," Physical review letters **63**, 1078 (1989). I.4.2, IV.1.3

[38] H. J. Maris, "Critical phenomena in he 3 and he 4 at t= 0 k," Physical review letters **66**, 45 (1991). I.4.2, IV.1.3

[39] M. Mélich, "Implantation d'atomes de césium dans un cristal d'hélium," Thèse, Université Pierre et Marie Curie - Paris VI (2008). II.1, II.1.2, II.3.2

[40] E. D. Adams, "High-resolution capacitive pressure gauges," Rev. Sci. Instrum. **64**, 365–367 (1993). II.1.2

[41] J. A. Nissen, E. Bodegom, L. C. Brodie, and J. S. Semura, "Tensile strength of liquid ^4he," Phys. Rev. B **40**, 6617–6624 (1989). II.4, IV.2.2, V

[42] X. Chavanne, S. Balibar, and F. Caupin, "Acoustic crystallization and heterogeneous nucleation," Physical review letters **86**, 5506 (2001). II.4

[43] X. Chavanne, S. Balibar, F. Caupin, C. Appert, and D. d'Humières, "Optical measurement of the non-linear focusing of sound in liquid helium 4," Journal of low temperature physics **126**, 643–648 (2002). II.4, IV.1.4

[44] F. Souris, J. Grucker, J. Dupont-Roc, P. Jacquier, A. Arvengas, and F. Caupin, "Time-resolved multiphase interferometric of a highly focused ultrasound pulse," Applied Optics **49**, 6127 (2010). II.4, IV.2.4

[45] C. V. Raman and N. Nagendra Nath, "The Diffraction of Light by High Frequency Sound Waves: Part I," Proceedings of the Indian Academy of Science, Section A **2**, 406–412 (1935). II.4.3.3

[46] M. G. Moharam and L. Young, "Criterion for bragg and raman-nath diffraction regimes," Appl. Opt. **17**, 1757–1759 (1978). URL: http://ao.osa.org/abstract.cfm?URI=ao-17-11-1757. II.4.3.3

[47] J. Lemaitre and R. Desmorat, *Engineering Damage Mechanics, chapters 4 and 6* (Springer, Berlin Heidelberg New York, 2005). III.3

[48] F. Souris, A. Qu, J. Dupont-Roc, J. Grucker, and P. Jacquier, "On the destabilization of metastable solidˆ 4he," Journal of Low Temperature Physics **179**, 390–395 (2015). III.3

[49] F. Werner, G. Beaume, A. Hobeika, S. Nascimbene, C. Herrmann, F. Caupin, and S. Balibar, "Liquid helium up to 160 bar," Journal of low temperature physics **136**, 93–116 (2004). IV.1.1, IV.1.4

[50] F. Caupin, S. Balibar, and H. J. Maris, "Limits of metastability of liquid helium," Physica B: Condensed Matter **329**, 356–359 (2003). IV.1.1, IV.2.5

[51] F. Caupin and S. Balibar, "Cavitation pressure in liquid helium," Phys. Rev. B **64**, 064507 (2001). URL: http://link.aps.org/doi/10.1103/PhysRevB.64.064507. IV.1.3, IV.2, IV.2.1, IV.2.5, IV.2.6, IV.10, V.5

[52] L. Vranješ, J. Boronat, J. Casulleras, and C. Cazorla, "Quantum monte carlo simulation of overpressurized liquid he 4," Physical review letters **95**, 145302 (2005). IV.1.3

[53] R. Ishiguro, F. Caupin, and S. Balibar, "Homogeneous nucleation of crystals by acoustic waves," EPL (Europhysics Letters) **75**, 91 (2006). URL: http://stacks.iop.org/0295-5075/75/i=1/a=091. IV.1.4

[54] J. Boronat, J. Casulleras, and J. Navarro, "Monte carlo calculations for liquid ^{4}He at negative pressure," Phys. Rev. B **50**, 3427–3430 (1994). URL: http://link.aps.org/doi/10.1103/PhysRevB.50.3427. IV.2, IV.2.5

[55] F. Dalfovo, A. Lastri, L. Pricaupenko, S. Stringari, and J. Treiner, "Structural and dynamical properties of superfluid helium: A density-functional approach," Phys. Rev. B **52**, 1193–1209 (1995). URL: http://link.aps.org/doi/10.1103/PhysRevB.52.1193. IV.2, IV.2.5

[56] G. H. Bauer, D. M. Ceperley, and N. Goldenfeld, "Path-integral monte carlo simulation of helium at negative pressures," Phys. Rev. B **61**, 9055–9060 (2000). URL: http://link.aps.org/doi/10.1103/PhysRevB.61.9055. IV.2, IV.2.5

[57] H. J. Maris and D. O. Edwards, "Thermodynamic properties of superfluid ^{4}he at negative pressure," J. Low Temp. Phys. **129**, 1 (2002). IV.2, IV.2.5

[58] H. Lambaré, P. Roche, S. Balibar, H. Maris, O. Andreeva, C. Guthmann, K. Keshishev, and E. Rolley, "Cavitation in superfluid helium-4 at low temperature," The European Physical Journal B-Condensed Matter and Complex Systems **2**, 381–391 (1998). IV.2.1, IV.2.2, V

[59] S. Balibar, C. Guthmann, H. Lambare, P. Roche, E. Rolley, and H. Maris, "Quantum cavitation in superfluid helium 4 ?" Journal of Low Temperature Physics **101**, 271–277 (1995). URL: http://dx.doi.org/10.1007/BF00754588. IV.2.2

[60] Q. Xiong and H. J. Maris, "Study of cavitation in superfluid helium-4 at low temperatures," J. Low Temp. Phys. **82**, 105 (1991). IV.2.5

[61] H. Maris, "Theory of quantum nucleation of bubbles in liquid helium," Journal of Low Temperature Physics **98**, 403–424 (1995). URL: http://dx.doi.org/10.1007/BF00752276. IV.2.5

[62] D. M. Jezek, M. Guilleumas, M. Pi, M. Barranco, and J. Navarro, "Thermal nucleation and cavitation in ^{3}He and ^{4}He," Phys. Rev. B **48**, 16582–16588 (1993). URL: http://link.aps.org/doi/10.1103/PhysRevB.48.16582. IV.2.5

[63] H. J. Maris, "Nucleation of bubbles on quantized vortices in helium-4," J. Low Temp. Phys. **94**, 125 (1994). IV.2.5

[64] M. S. Pettersen, S. Balibar, and H. J. Maris, "Experimental investigation of cavitation in superfluid ^{4}He," Phys. Rev. B **49**, 12062 (1994). URL: http://link.aps.org/doi/10.1103/PhysRevB.49.12062. IV.2.5

[65] Appert, C., Tenaud, C., Chavanne, X., Balibar, S., Caupin, F., and d'Humières, D., "Nonlinear effects and shock formation in the focusing of a spherical acoustic wave," Eur. Phys. J. B **35**, 531–549 (2003). URL: http://dx.doi.org/10.1140/epjb/e2003-00307-0. IV.2.6

[66] A. Qu, A. Trimeche, J. Dupont-Roc, J. Grucker, and P. Jacquier, "Cavitation density of superfluid helium-4 around 1 k," Physical Review B **91**, 214115 (2015). IV.3

[67] P. Roche, H. Lambaré, E. Rolley, D. Lacoste, S. Balibar, C. Guthmann, and H. Maris, "Growth and collapse of bubbles in superfluid4he," Czechoslovak Journal of Physics **46**, 381–382 (1996). V, V.4.3.1, V.4.3.2

[68] J. W. S. B. Rayleigh, *Scientific papers*, vol. 2 (CUP Archive, 1900). V.2.1

[69] G. Taylor, "The instability of liquid surfaces when accelerated in a direction perpendicular to their planes. i," in "Proceedings of the Royal Society of London A: Mathematical, Physical and Engineering Sciences," , vol. 201,1065 (The Royal Society, 1950), vol. 201,1065, pp. 192–196. V.2.1

[70] D. Sharp, "An overview of rayleigh-taylor instability," Physica D: Nonlinear Phenomena **12**, 3 – 18 (1984). URL: http://www.sciencedirect.com/science/article/pii/0167278984905104. V.2.1

[71] Rayleigh, "On the pressure developped in a liquid during the collapse of a spherical cavity," Phil. Mag. **34**, 94 (1917). V.2.2

[72] T. Von Kármán, *Aerodynamics* (Cornell University press: Mc Graw-Hill company, 1963). V.4.1

[73] M. S. Plesset and A. Prosperetti, "Bubble dynamics and cavitation," Annual review of fluid mechanics **9**, 145–185 (1977). V.4.2, V.4.4

[74] M. P. Brenner, S. Hilgenfeldt, and D. Lohse, "Single-bubble sonoluminescence," Rev. Mod. Phys. **74**, 425–484 (2002). URL: http://link.aps.org/doi/10.1103/RevModPhys.74.425. V.4.2

[75] A. Prosperetti, "In nato advanced studies institute on sonoluminescence and sonochemstry ed," Crum L (Dortrecht: Kluwer) p39 (1998). V.4.2

[76] A. Prosperetti, L. A. Crum, and K. W. Commander, "Nonlinear bubble dynamics," The Journal of the Acoustical Society of America **83**, 502–514 (1988). V.4.2

[77] L. Landau and E. Lifshitz, "Fluid mechanics, vol. 6, 1987," . V.4.3

[78] T. Shimazaki, M. Murakami, and T. Iida, "Second sound wave heat transfer, thermal boundary layer formation and boiling: highly transient heat transport phenomena in he ii," Cryogenics **35**, 645 (1995). V.4.3

[79] W. Kutta, "Beitrag zur naherungsweisen integration totaler differentialgleichungen," Z. Math. Phys. **46**, 435 (1901). V.4.3

[80] J. Butcher, "A history of runge-kutta methods," Applied Numerical Mathematics **20**, 247 (1996). V.4.3

[81] I. Akhatov, O. Lindau, A. Topolnikov, R. Mettin, N. Vakhitova, and W. Lauterborn, "Collapse and rebound of a laser-induced cavitation bubble," Physics of Fluids (1994-present) **13**, 2805–2819 (2001). V.4.3.1

[82] F. Caupin, "Cavitation dans l'hélium 3 : un liquide de Fermi à pression négative," Theses, Université Pierre et Marie Curie - Paris VI (2001). V.4.3.1

[83] M. Tinguely, D. Obreschkow, P. Kobel, N. Dorsaz, A. de Bosset, and M. Farhat, "Energy partition at the collapse of spherical cavitation bubbles," Phys. Rev. E **86**, 046315 (2012). URL: http://link.aps.org/doi/10.1103/PhysRevE.86.046315. V.4.3.1

[84] B. P. Barber and S. J. Putterman, "Light scattering measurements of the repetitive supersonic implosion of a sonoluminescing bubble," Phys. Rev. Lett. **69**, 3839–3842 (1992). URL: http://link.aps.org/doi/10.1103/PhysRevLett.69.3839. V.4.3.1, V.4.3.2

[85] M. Plesset, "The dynamics of cavitation bubbles," Journal of applied mechanics **16**, 277–282 (1949). V.4.3.2

[86] M. S. Plesset and S. A. Zwick, "The growth of vapor bubbles in superheated liquids," Journal of Apllied Physics **25**, 493 (1954). V.4.4

[87] L. W. Florschuetz and B. T. Chao, "On the mechanics of vapor bubble collapse," Journal of Heat Transfer **87**, 209 (1965). V.4.4

[88] A. Qu, A. Trimeche, P. Jacquier, and J. Grucker, "Dramatic effect of superfluidity on the collapse of he 4 vapor bubbles," Physical Review B **93**, 174521 (2016). V.5

An QU **20 janvier 2017**

Sujet : Étude expérimentale de l'hélium-4 solide et superfluide en phase métastable

Résumé : L'hélium solide métastable est un candidat possible pour la supersolidité. Notre équipe a démontré en 2011 que l'on pouvait obtenir de l'hélium solide métastable à des pressions inférieures à la pression de fusion à l'aide d'une onde acoustique focalisée. Cependant, une instabilité inattendue apparaît lorsque la pression locale du crystal atteint ~ 21 bar c'est à dire 4 bar sous la pression de fusion. J'ai donc commencé ma thèse en étudiant le temps d'apparition de l'instabilité, et j'ai confirmé qu'elle apparaît toujours dans des phases de décompression de l'onde sonore, c'est à dire à une pression inférieure à la pression de fusion.

Ensuite, j'ai étudié la limite de cavitation de l'hélium superfluide à pression négative. En utilisant une méthode interférométrique développée par mon prédécesseur Fabien Souris, j'ai mesuré directement la densité de cavitation de l'hélium superfluide métastable. J'ai trouvé que, à 1 K, l'hélium superfluide cavite lorsque sa densité locale a diminué de 8.4%. En utilisant une équation d'état bien établie théoriquement, on peut convertir ce résultat en pression de cavitation pour le comparer avec ceux obtenus par d'autres groupes. À ma grande surprise, mon résultat n'est pas compatible avec ces derniers. Cette incompatibilité soulève des questions intéressantes quant à la possibilité de nucléation de la bulle sur des vortex quantifiés.

Enfin, j'ai étudié la dynamique de la bulle d'hélium déclenchée par la cavitation. En analysant l'équation du mouvement de la bulle et le transfert de chaleur correspondant, j'ai expliqué avec succès pourquoi la durée de vie de la bulle a une transition dramatique quand l'hélium passe de liquide normal à superfluide.

Mots clés : hélium métastable, instabilité, cavitation, durée de vie de bulle

Subject : Experimental study of metastable solid and superfluid helium-4

Abstract: Metastable solid helium is a possible candidate for supersolidity. In 2011, our group has demonstrated that we could obtain the metastable solid helium at pressures below the melting pressure using a focused acoustic wave. However, an unexpected instability occurs when the local pressure of the crystal reaches 21 bar which is $\sim$ 4 bar below the melting pressure. So I started my thesis by studying the appearance time of the instability, and I confirmed that it always appears at the low pressure swing of the acoustic wave.

Then, I studied the cavitation limit of superfluid helium at negative pressure. Using an interferometric method developed by my predecessor Fabien Souris, I directly measured the cavitation density of metastable superfluid helium. I found that at 1 K, superfluid helium cavitates when its local density is lowered by 8.4%. Using a theoretically well-established equation of state, this result can be converted to a cavitation pressure in order to compare our results with those obtained by others groups. To my surprise, my result is not consistent with the others'. This incompatibility raises interesting questions about the possibility of nucleation of the bubble on quantified vortices.

Finally, I studied the dynamics of the helium bubble triggered by cavitation. By analyzing the equation of motion of bubble and the corresponding heat transfer, I have successfully explained why the bubble's lifetime has a dramatic transition as the helium passes from normal liquid to superfluid.

Keywords : metastable helium, instability, cavitation, bubble lifetime